

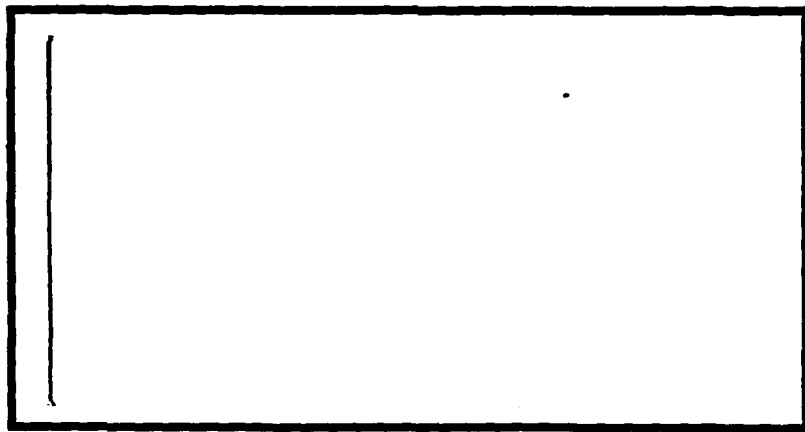
DTIC FILE COPY

①

AD-A203 179



DTIC  
 ELE  
 JAN 17 1989  
 S H D



DEPARTMENT OF THE AIR FORCE  
 AIR UNIVERSITY

**AIR FORCE INSTITUTE OF TECHNOLOGY**

Wright-Patterson Air Force Base, Ohio

**DISTRIBUTION STATEMENT A**  
 Approved for public release:  
 Distribution Unlimited

89 1 17 028

①

AFIT/GAE/AA/88D-18

EFFECTS OF BATTLE DAMAGE REPAIR ON THE  
NATURAL FREQUENCIES AND MODE SHAPES OF  
CURVED RECTANGULAR COMPOSITE PANELS

THESIS

William P. Goodwin  
Major, US Army

AFIT/GAE/AA/88D-18

DTIC  
ELECTE  
S JAN 17 1989 D  
H

Approved for public release; distribution unlimited

AFIT/GAE/AA/88D-18

THESIS

Presented to the Faculty of the School of Engineering  
of the Air Force Institute of Technology

Air University

In Partial Fulfillment of the  
Requirements for the Degree of  
Master of Science in Aeronautical Engineering

William P. Goodwin, B.S.

Major, US Army

December 1988

Approved for public release; distribution unlimited

## Preface

First and foremost, I want to thank my wife, [REDACTED] for her patience, understanding, and support during the past 18 months. Her knack for keeping things in perspective and providing candid criticism was indispensable. A special thanks to my girls, [REDACTED] and [REDACTED] who learned a new vocabulary from Dad while he studied; and whose candid observations about the past year-and-a-half have been priceless.

I owe much to my faculty advisor, Dr. Anthony Palazotto, who had more faith in me than I had in myself. A special thanks to my original thesis advisor, Major Terry Hinnerichs, who pointed me in the right direction; to Major Ron Hinrichsen, whose enthusiasm and insight were invaluable in keeping me on track; and to Captain Howard Gans, who pitched the final two innings as my relief advisor.

I owe a great debt of gratitude to Mr. Gene Maddux of the Flight Dynamics Laboratory (FDL), and to Lieutenant Dave Felker and Mr. Pat Baker of the FDL Composites Shop. Mr. Maddux unselfishly shared his vast knowledge of holography and modal analysis, helping me to avoid the pitfalls that threaten a novice in this area. Lieutenant Felker and Mr. Baker provided invaluable advice and assistance in the design and application of the technique used to repair the test panels. Finally, a special thanks to a classmate, Captain Kurt Lautenbach, for taking me from slide rules to computers.

William P. Goodwin

## Table of Contents

	Page
Preface . . . . .	ii
List of Figures . . . . .	v
List of Tables . . . . .	x
Abstract . . . . .	xi
I. Introduction . . . . .	1.1
Background . . . . .	1.1
Approach . . . . .	1.5
II. Theory . . . . .	2.1
Interferometric Holography . . . . .	2.1
Lamination Theory . . . . .	2.10
Finite Element Theory . . . . .	2.27
III. Composite Panels . . . . .	3.1
Composite Panel Properties . . . . .	3.1
Repairs . . . . .	3.4
IV. Experimental Analysis . . . . .	4.1
Equipment . . . . .	4.1
Holography Procedure . . . . .	4.12
V. Finite Element Analysis . . . . .	5.1
Element Selection . . . . .	5.1
Panel Modeling . . . . .	5.4
VI. Results and Discussion . . . . .	6.1
Unrepaired Panels . . . . .	6.2
Repaired Panels . . . . .	6.31
Repair Effects . . . . .	6.67
NISA Analysis . . . . .	6.72
VII. Conclusions . . . . .	7.1
VIII. Recommendations for Further Study . . . . .	8.1

Table of Contents (Cont'd)

	Page
Bibliography . . . . .	BIBL.1
Appendix A: Holography Test Equipment . . . . .	A.1
Appendix B: Holography Procedure with NRC HC-300 System . . . . .	B.1
Appendix C: Sample NISA Input File . . . . .	C.1
Appendix D: NISA Element Formulation . . . . .	D.1
Appendix E: Preliminary NISA Study . . . . .	E.1
Vita . . . . .	V.1



<b>Accession For</b>	
NTIS GRA&I	<input checked="" type="checkbox"/>
DTIC TAB	<input type="checkbox"/>
Unannounced	<input type="checkbox"/>
Justification	
By _____	
Distribution/	
Availability Codes	
Dist	Avail and/or Special
A-1	

List of Figures

Figure	Page
2.1. Constructive Interference . . . . .	2.4
2.2. Destructive Interference . . . . .	2.4
2.3. Cumulative Effect of Wave Front Interference .	2.5
2.4. Object and Reference Beams . . . . .	2.6
2.5. Construction of the Hologram by Recording the Object Wave Front . . . . .	2.7
2.6. Reconstruction of the Object Wave Front Using the Hologram Made in Figure 2.5 . . . .	2.8
2.7. (a) Real-Time Holography; (b) Time-Average Holography . . . . .	2.10
2.8. Structural (x-y-z) versus Material (1-2-3) Coordinate Systems . . . . .	2.12
2.9. In-Plane Force Resultants . . . . .	2.19
2.10. Shear Resultants . . . . .	2.19
2.11. Moment Resultants . . . . .	2.20
2.12. Geometry of an N-Layered Laminate . . . . .	2.21
2.13. Panel Coordinate System and Displacements .	2.23
3.1. Ratio of Fiber Area to Matrix Area . . . . .	3.2
3.2. Panel Geometry . . . . .	3.3
3.3. Repair Patch Geometry . . . . .	3.10
3.4. Typical Repair Patch (Front) . . . . .	3.11
3.5. Typical Repair Patch (Back) . . . . .	3.11
4.1. Test Fixture Curved Channel (Cap) . . . . .	4.3
4.2. Test Fixture (Front) . . . . .	4.3
4.3. Test Fixture (Back) . . . . .	4.4

List of Figures (Cont'd)

Figure	Page
4.4. Thermoplastic Hologram Process . . . . .	4.7
4.5. Instrumentation Diagram . . . . .	4.8
4.6. Equipment Setup (Schematic) . . . . .	4.9
4.7. Equipment Setup (Front) . . . . .	4.10
4.8. Equipment Setup (Back) . . . . .	4.10
5.1. Parabolic Composite General Shell, Element NKTP 32 . . . . .	5.3
5.2. Nodal Degrees of Freedom, Element NKTP 32 . . . . .	5.3
5.3. Half-Panel Model (NKTP 32, Eight-Noded Element) . . . . .	5.6
6.1. Solid Panel--Mode 1 . . . . .	6.5
6.2. Solid Panel--Mode 2 . . . . .	6.5
6.3. Solid Panel--Mode 3 . . . . .	6.6
6.4. Solid Panel--Mode 4 . . . . .	6.6
6.5. Solid Panel--Mode 5 . . . . .	6.7
6.6. Solid Panel--Mode 1 (NISA) . . . . .	6.7
6.7. Solid Panel--Mode 2 (NISA) . . . . .	6.8
6.8. Solid Panel--Mode 3 (NISA) . . . . .	6.8
6.9. Solid Panel--Mode 4 (NISA) . . . . .	6.9
6.10. 0° Cutout Panel--Mode 1 . . . . .	6.12
6.11. 0° Cutout Panel--Mode 2 . . . . .	6.12
6.12. 0° Cutout Panel--Mode 3 . . . . .	6.13
6.13. 0° Cutout Panel--Mode 4 . . . . .	6.13

List of Figures (Cont'd)

Figure	Page
6.14. 0° Cutout Panel--Mode 5 . . . . .	6.14
6.15. 0° Cutout Panel--Mode 1 (NISA) . . . . .	6.14
6.16. 0° Cutout Panel--Mode 2 (NISA) . . . . .	6.15
6.17. 0° Cutout Panel--Mode 3 (NISA) . . . . .	6.15
6.18. 0° Cutout Panel--Mode 4 (NISA) . . . . .	6.16
6.19. 90° Cutout Panel--Mode 1 . . . . .	6.18
6.20. 90° Cutout Panel--Mode 2 . . . . .	6.19
6.21. 90° Cutout Panel--Mode 3 . . . . .	6.19
6.22. 90° Cutout Panel--Mode 4 . . . . .	6.20
6.23. 90° Cutout Panel--Mode 5 . . . . .	6.20
6.24. 90° Cutout Panel--Mode 1 (NISA) . . . . .	6.21
6.25. 90° Cutout Panel--Mode 2 (NISA) . . . . .	6.21
6.26. 90° Cutout Panel--Mode 3 (NISA) . . . . .	6.22
6.27. 90° Cutout Panel--Mode 4 (NISA) . . . . .	6.22
6.28. +45° Cutout Panel--Mode 1 . . . . .	6.25
6.29. +45° Cutout Panel--Mode 2 . . . . .	6.25
6.30. +45° Cutout Panel--Mode 3 . . . . .	6.26
6.31. +45° Cutout Panel--Mode 4 . . . . .	6.26
6.32. +45° Cutout Panel--Mode 5 . . . . .	6.27
6.33. -45° Cutout Panel--Mode 1 . . . . .	6.29
6.34. -45° Cutout Panel--Mode 2 . . . . .	6.29
6.35. -45° Cutout Panel--Mode 3 . . . . .	6.30
6.36. -45° Cutout Panel--Mode 4 . . . . .	6.30

List of Figures (Cont'd)

Figure	Page
6.37. -45° Cutout Panel--Mode 5 . . . . .	6.31
6.38. Summary of Repair Effect on 0° Cutout Panel .	6.37
6.39. 0° Repaired Panel--Mode 1 . . . . .	6.38
6.40. 0° Repaired Panel--Mode 2 . . . . .	6.38
6.41. 0° Repaired Panel--Mode 3 . . . . .	6.39
6.42. 0° Repaired Panel--Mode 4 . . . . .	6.39
6.43. 0° Repaired Panel--Mode 5 . . . . .	6.40
6.44. 0° Repaired Panel--Mode 1 (NISA) . . . . .	6.40
6.45. 0° Repaired Panel--Mode 2 (NISA) . . . . .	6.41
6.46. 0° Repaired Panel--Mode 3 (NISA) . . . . .	6.41
6.47. 0° Repaired Panel--Mode 4 (NISA) . . . . .	6.42
6.48. Summary of Repair Effect on 90° Cutout Panel .	6.47
6.49. 90° Repaired Panel--Mode 1 . . . . .	6.48
6.50. 90° Repaired Panel--Mode 2 . . . . .	6.48
6.51. 90° Repaired Panel--Mode 3 . . . . .	6.49
6.52. 90° Repaired Panel--Mode 4 . . . . .	6.49
6.53. 90° Repaired Panel--Mode 5 . . . . .	6.50
6.54. 90° Repaired Panel--Mode 1 (NISA) . . . . .	6.50
6.55. 90° Repaired Panel--Mode 2 (NISA) . . . . .	6.51
6.56. 90° Repaired Panel--Mode 3 (NISA) . . . . .	6.51
6.57. 90° Repaired Panel--Mode 4 (NISA) . . . . .	6.52
6.58. Summary of Repair Effects on +45° Cutout Panel . . . . .	6.57
6.59. +45° Repaired Panel--Mode 1 . . . . .	6.58

List of Figures (Cont'd)

Figure	Page
6.60. +45° Repaired Panel--Mode 2 . . . . .	6.58
6.61. +45° Repaired Panel--Mode 3 . . . . .	6.59
6.62. +45° Repaired Panel--Mode 4 . . . . .	6.59
6.63. +45° Repaired Panel--Mode 5 . . . . .	6.60
6.64. Summary of Repair Effect on -45° Cutout Panel . . . . .	6.64
6.65. -45° Repaired Panel--Mode 1 . . . . .	6.65
6.66. -45° Repaired Panel--Mode 2 . . . . .	6.65
6.67. -45° Repaired Panel--Mode 3 . . . . .	6.66
6.68. -45° Repaired Panel--Mode 4 . . . . .	6.66
6.69. -45° Repaired Panel--Mode 5 . . . . .	6.67
D.1. NKTP 32 Element Natural Coordinate System . .	D.2
D.2. Thickness Vector $C_i$ . . . . .	D.4
D.3. Displacement and Rotation Degrees of Freedom .	D.5

List of Tables

Table	Page
3.1. Material Properties of the Panels . . . .	3.2
3.2. Properties of the Patch Materials . . . .	3.5
3.3. Effective Engineering Properties of the Panels . . . . .	3.7
5.1. Convergence Study for Eight-Noded Element . . . . .	5.5
6.1. Solid Panel Results . . . . .	6.4
6.2. 0° Cutout Panel Results . . . . .	6.11
6.3. 90° Cutout Panel Results . . . . .	6.18
6.4. +45° Cutout Panel Results . . . . .	6.24
6.5. -45° Cutout Panel Results . . . . .	6.28
6.6. 0° Repaired Panel Results . . . . .	6.36
6.7. 90° Repaired Panel Results . . . . .	6.46
6.8. +45° Repaired Panel Results . . . . .	6.56
6.9. -45° Repaired Panel Results . . . . .	6.63
6.10. NISA Results Summary . . . . .	6.73
E.1. Monahan's Aluminum Plate . . . . .	E.2
E.2. Yen's Composite Plate . . . . .	E.3
E.3. Soedel's Steel Cylinder . . . . .	E.4

## Abstract

Interferometric holography and a finite element computer code, NISA, were used to experimentally and analytically determine the effects of battle damage repairs on the free vibrational behavior of thin, cylindrical composite panels. The primary objective was to experimentally determine how the mass and stiffness changes introduced by mechanically fastened aluminum patches altered the natural frequencies and mode shapes of the panels. The secondary objective was to investigate the accuracy of the PC version of NISA in predicting the free vibrational behavior of the same panels.

The thin, graphite/epoxy panels had a quasi-isotropic lay-up,  $[0/-45/45/90]_S$ , and a 12-inch height and 12-inch radius of curvature. Each fully-clamped panel had a 2 x 4-inch cutout oriented at either  $0^\circ$ ,  $90^\circ$ ,  $+45^\circ$ , or  $-45^\circ$  with respect to the panel circumference. A thin, 3.5 x 5.5-inch aluminum patch was riveted to each panel to cover the cutout area.

It was found that, in general, the patch increased the natural frequencies of the cutout panels, but did not consistently restore the frequencies of the original solid panel. The mode shapes were restored to those of the original solid panel, although at the higher modes they did not always appear in the original sequence. The influence of

the patch on the mode shapes increased at the higher modes as panel behavior became increasingly localized.

NISA predictions for the natural frequencies were within 10%-20% of the experimental results except for the 90° repaired panel, where they were within 2%-6%. The correct mode shapes were predicted; however, they frequently appeared in a different sequence than observed experimentally.

A parallel investigation showed that both the NISA thin shell and general shell elements gave excellent results for both an isotropic flat plate and cylinder. Accuracy decreased slightly when the composite general shell element was used for a thin composite plate. The least accuracy was observed when the composite general shell element was used for a composite cylindrical panel.

EFFECTS OF BATTLE DAMAGE REPAIR ON THE  
NATURAL FREQUENCIES AND MODE SHAPES OF  
CURVED RECTANGULAR COMPOSITE PANELS

I. Introduction

Background

Historical Perspective. Aircraft Battle Damage Repair (ABDR) is vital to a commander in combat. A successful ABDR program helps to maintain combat power by quickly returning damaged aircraft to battle. In the 1980 "Air Force Concept for Aircraft Battle Damage Repair," USAF Brigadier General Lawrence D. Garrison stated:

The primary purpose of ABDR is to restore sufficient strength and serviceability to permit damaged aircraft to fly additional sorties, of at least partial mission capability, within time to contribute to the outcome of the ongoing battle. The secondary objective is to enable those aircraft damaged beyond unit repair capability to make a one-time flight to its home station, rear area base or major repair facility. ABDR will involve simple repair techniques which eliminate most of the fatigue-conscious methods used in peacetime. Rapid repairs can be performed on most types of damage resulting in significant savings of time without compromising the safety or mission effectiveness of the aircraft [34:1].

Since then, the aerospace industry has expanded its use of composite materials. Their application in high performance combat aircraft has increased because composites

provide superior strength-to-weight and stiffness-to-weight ratios than traditional aerospace metal alloys [14:1]. This trend toward composites, however, brings with it the need for effective repair procedures. Thus far, repair procedures performed at peacetime depots and fixed bases have been developed, documented, and used. Less information is known about abbreviated procedures that could be effectively applied in theaters of operation where materials, equipment, and shelter would be scarce and where airmen making the repairs would be under enormous wartime stress.

Approaches to composite ABDR have mainly been modifications of current ABDR techniques for metal structures or abbreviated versions of composite manufacturing processes. The two types are bolted repairs and bonded repairs. Each has distinct advantages and disadvantages, depending upon the technique itself and upon the environment in which it is applied. The Army has concentrated on bonded repairs [45], while the Navy and Air Force have investigated both types. Within the Air Force, the Flight Dynamics Laboratory and the Materials Laboratory have conducted and sponsored research on this subject. The Flight Dynamics Laboratory sponsored work by McDonnell-Douglas Corporation [12] and by Rockwell Corporation [34] on bolted repair methods, while the Materials Laboratory sponsored Northrop Corporation's work on bonded repairs [20]. In addition, Lockheed-California

developed, fabricated, and tested bolted and bonded field-level repairs for several contract and independent research efforts [37].

Bolted repairs for composites are similar to traditional bolted repairs of metal structures. A metal patch is bolted or riveted to the composite structure to cover the damaged area. Advantages include minimal surface preparation, ease of inspection, resistance to temperature and humidity effects, and use of commonplace tools, materials, and skills. Disadvantages are the weight of the fasteners, the weakening of the structure caused by the fastener holes, the creation of stress concentrations by the fasteners themselves, the uneven load distribution due to nonuniform clearances between hole and fastener, and the possibility of delamination damage from drilling and machining [20:8].

A bonded repair more closely resembles the composite structure's original condition, both visually and structurally. Advantages are lighter weight and better load distribution. Thus, a bonded repair is a more desirable end product. Several factors, however, presently make such repairs impractical in an austere theater of operation. The controlled environment, specialized tools and materials, and advanced skills will not be widely available to the operational line units where damaged aircraft will first arrive for repair. Additional disadvantages include temperature

and humidity effects on the repair, the need for extensive surface preparation, and the difficulty of inspecting the repair [20:8].

Statement and Scope of the Problem. A literature review reveals that most research conducted thus far has been static tests of critical buckling loads and other load-bearing behavior of repaired structures. The emphasis has been on primary load-bearing structures for which static analysis is especially important. Secondary structures, such as fairings and skins, have received less attention. Since they often protect sensitive equipment as an aircraft maneuvers through the environment, they would also have to be repaired when battle damage occurs. Although subjected to minimal static loads, they still experience low amplitude dynamic forces such as the acoustic vibrations that are transmitted through an aircraft in flight. Thus, it is logical to investigate how repairs to secondary structures alter their response to such forces.

A recognized method for investigating such dynamic behavior is modal analysis, which is the identification and evaluation of the natural frequencies and mode shapes of a vibrating structure. These natural, or resonant, frequencies are important because they are the frequencies at which a lightly damped structure will vibrate at a continually increasing amplitude. When the amplitude reaches high

enough levels, vibrations may become violent enough to cause damage or catastrophic failure.

While literature abounds with closed-form solutions to simple problems such as strings, beams, and thin plates, such solutions to more complicated and practical problems like curved composite shells have not proven successful. Fortunately, numerical methods, such as finite elements, provide ways to make relatively accurate predictions of the behavior of such complex structures. Experimental methods, such as interferometric holography, can be used to directly observe, measure, and obtain solutions to these more complex problems.

### Approach

General. Cylindrically curved, graphite/epoxy panels were selected to model a small section of an aircraft structure for this analysis. These thin shell panels are representative of secondary structures on aircraft that are made of composite material. Several previous studies reveal much about both the static and the dynamic behavior of these panels. The addition of a repair patch is an extension of these efforts, the most relevant of which are mentioned below.

Tisler [38] studied the static behavior of these composite panels under buckling loads. Walley [42] and Cyr [7]

investigated dynamic behavior. In 1985, Walley investigated the effect of interior cutout size (2 x 2, 2 x 4, and 4 x 4 inch) on the panels' natural frequencies and mode shapes. In 1986, Cyr followed by investigating the effect of cutout orientation (vertical, horizontal, and 45° angle) on the natural frequencies and mode shapes of similar curved composite panels. Since no closed-form solution exists, Walley and Cyr each used interferometric holography and finite elements to experimentally and numerically perform their modal analyses.

A logical extension to Walley's and Cyr's efforts was an investigation of the effect of Aircraft Battle Damage Repairs on the natural frequencies and mode shapes of these curved composite panels. The dissimilar materials introduced into the structure by a mechanically fastened patch should alter the mass and stiffness of the panel. The effect of these alterations on the dynamic behavior of the panels is of interest to the engineer.

The approach to answering this question mirrored those of Walley and Cyr. First, interferometric holography was used to observe the actual dynamic behavior of the acoustically excited test panels. Second, the Finite Element Method (FEM) was used to analytically predict the same behavior. The results of the two types of analysis were then compared to reveal the effects of Aircraft Battle

Damage Repairs on the free response of these panels and to evaluate the accuracy of the FEM code in making such predictions.

General Outline of the Experimental Investigation.

Interferometric holography was used to observe the natural frequencies and mode shapes of the panels as they were acoustically excited through a continuous frequency range. Cyr's panels were used. First, Cyr's experiments were repeated to establish baseline data on the panels with the interior cutouts. This was necessary since any changes in structural mass or stiffness due to moisture content or hidden internal damage while in storage for two years would alter the dynamic behavior of the panels.

An initial series of tests was run at the Flight Dynamics Laboratory using a video holography system. This series was an initial exposure to holography. It was also an opportunity to locate the natural frequencies, identify asymmetric and symmetric modes, and improve the technique for mounting the panels to the test fixture so that consistent clamping conditions could be obtained. A second series of baseline tests was then run on AFIT's newly acquired thermoplastic holography system. This series was a repeat of the first; however, it served to work out the bugs in the new thermoplastic system and to refine the baseline against which the repaired panels were eventually compared.

General Outline of the Numerical Investigation. The FEM analysis was conducted using the commercially available Numerically Integrated Elements for System Analysis (NISA) program of the Engineering Mechanics Research Corporation (EMRC). The NISA PC version was used for this analysis.

Since there was no prior documentation about its usefulness for the dynamic analysis of the free vibrations of a cylindrically curved, thin, composite shell, a detailed analysis of NISA was conducted. This analysis compared NISA results with well-known theoretical, analytical, and experimental results of isotropic beams and flat plates, composite beams and flat plates, curved isotropic shells, and a cantilevered, curved composite shell. Once the limitations and peculiarities of this PC version of NISA were revealed through the simpler cases, the more complex composite panels with cutouts and patches were analyzed.

The analysis of the test models was conducted in a manner similar to those of Walley and Cyr, who each used STAGSC-1, another FEM code. The interactive pre- and post-processing capabilities of NISA were utilized to develop models and display results. As in the experimental phase, once the baseline for the solid panel was established, the focus turned to analyzing panel behavior before and after they were patched.

Contributions. The primary objective of this work was to experimentally analyze the effect of battle damage repairs on a structure that simulates a composite aerostructure. The secondary objective was to evaluate the accuracy of the PC version of NISA in predicting the experimental results. Contributions to future efforts are the conclusions drawn concerning the effects of unsophisticated repairs on the dynamic behavior of the composite panels, the reliability of the holographic test procedure, and the accuracy of the NISA models. Additional contributions from this work are the establishment of efficient procedures for the use of the new thermoplastic holography system, the development of simple techniques for patching the test panels, and the investigation of a variety of free vibration problems with the PC version of the NISA finite element code.

## II. Theory

This chapter presents the theoretical background for both the experimental and the numerical phases of this thesis. First, the basic theory of interferometric holography is summarized. Second, lamination theory is presented to show how the stiffness, force, and moment relationships for composite materials are developed. Finally, an overview of the NISA finite element program is presented, with emphasis on the formulation and solution of the eigenvalue problem for free vibration analysis.

### Interferometric Holography

This section summarizes the theory of split-beam interferometric holography. Chapter IV provides the details of its application in this thesis.

Split-beam interferometric holography produces three-dimensional images called holograms. Holograms are used in modal analysis because they can portray mode shapes, the geometric behavior of a structure vibrating at its natural frequencies. The mode shapes are composed of fringe patterns resembling contour lines on a topographic map. Each fringe represents a line of uniform displacement of the structure's surface, much as a contour line represents uniform elevation of the land. Hence, the fringe pattern or mode shape for a specific natural frequency visually

portrays the relative displacement of regions on the structure's surface as the structure vibrates at a natural frequency.

Holography is essentially a two-phase process. First, an image of the object is initially constructed by exposing an optical recording medium, such as a photographic plate (the traditional method) or a thermoplastic plate (the method used in this thesis), to light that has been diffused by the object. This phase is similar to taking a common photograph. Second, the image on the plate is reconstructed to make it visible to the naked eye.

Fringes, the essential elements of the hologram, are created by the interference of two or more light waves. The fringes portray minute displacements not otherwise visible to the naked eye [40:379]. An individual fringe line represents a displacement of approximately one-half the wavelength of the light being used to form the hologram. A Helium-Neon (HeNe) laser, for instance, produces light with a wavelength of approximately 24 microinches; thus, each fringe represents approximately a 12-microinch displacement [44:88]. Since interferometric holography creates a visible image of these very small displacements, it is very useful in modal analysis, where surface displacements of a vibrating object are in the microinch range.

The construction and reconstruction of holograms are based on the wave front formed when two other wave fronts with the same optical frequency interfere with one another. If the wave fronts are in phase, their amplitudes will be reinforced, resulting in constructive interference that produces light fringes on the recording plate as shown in Figure 2.1. If they are out of phase, their amplitudes will cancel, resulting in destructive interference that produces dark fringes as shown in Figure 2.2. The degree to which they are in or out of phase determines the size, shape, and intensity of these fringes. Captured on the plate, the fringe pattern is the basis for the three-dimensional hologram of the object [40:319-321]. Figure 2.3 shows the interference of the two wave fronts at the plate where the fringe pattern is created and recorded.

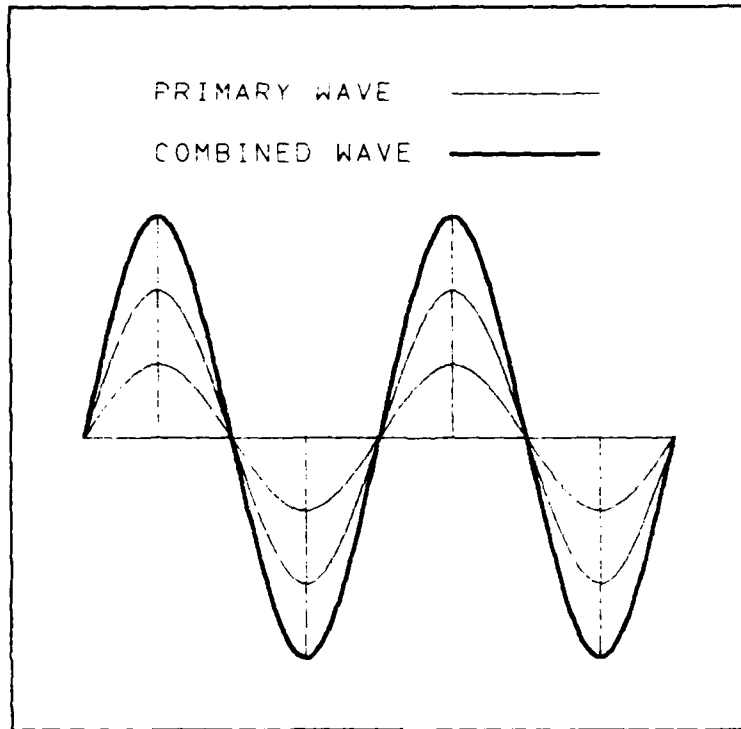


Figure 2.1. Constructive Interference [40:319]

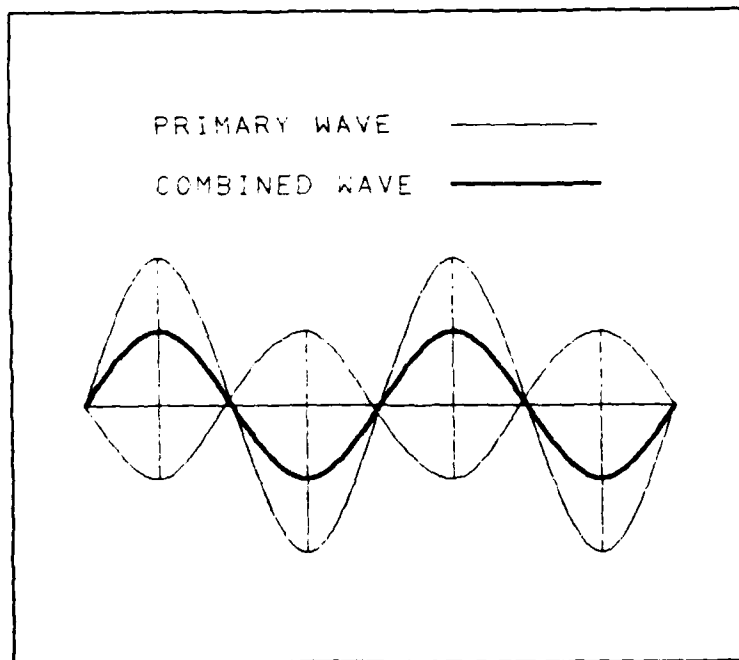


Figure 2.2. Destructive Interference [40:319]

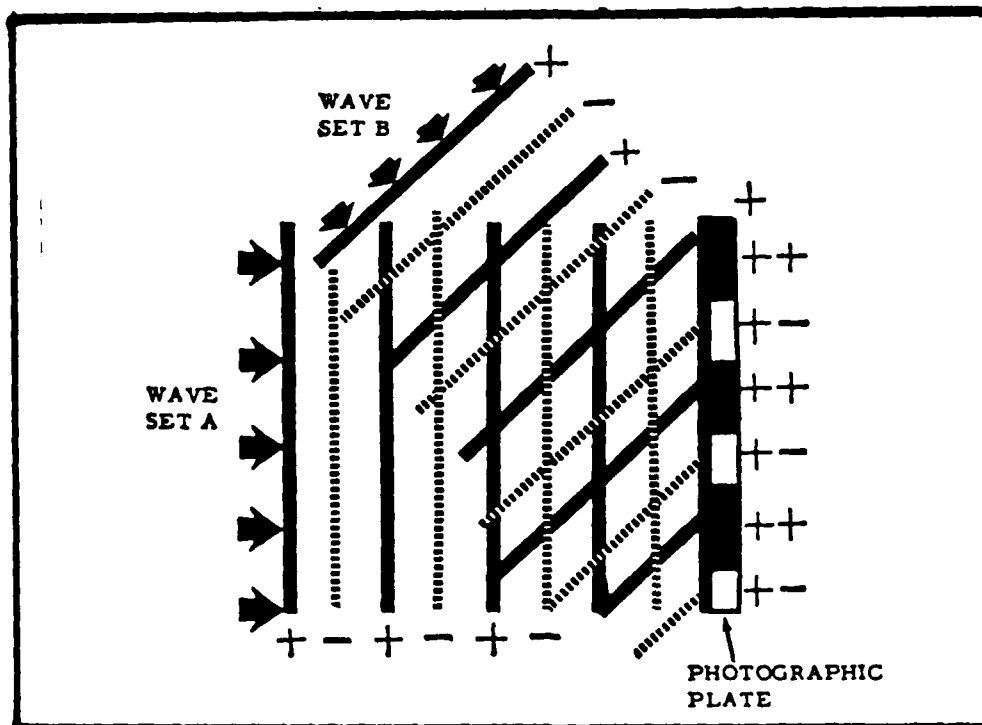


Figure 2.3. Cumulative Effect of Wave Front Interference [18:7]

Split-beam interferometric holography is based on the splitting of a coherent, monochromatic (single frequency) light beam into two separate beams [40:383]. One beam, the object beam, illuminates the object and is reflected from the object onto the plate. The other beam, the reference beam, bypasses the object and ultimately overlaps the object beam at the recording plate.

Light waves used in holography must have certain properties. They must be coherent, which means they must have the same frequency and be vibrating in phase; they must be temporally coherent, meaning they retain their coherence over

time and distance; and they must be spatially coherent, meaning that after being split, the separated waves retain mutual coherence [40:376,388,390].

The HeNe laser emits a single beam of light. This beam travels to a beam splitter that splits it into the reference beam and the object beam. These two beams travel separate paths until they meet at the recording plate as depicted in Figure 2.4. It is essential that their separate paths be nearly equidistant so the two beams are spatially coherent when they interfere at the plate.

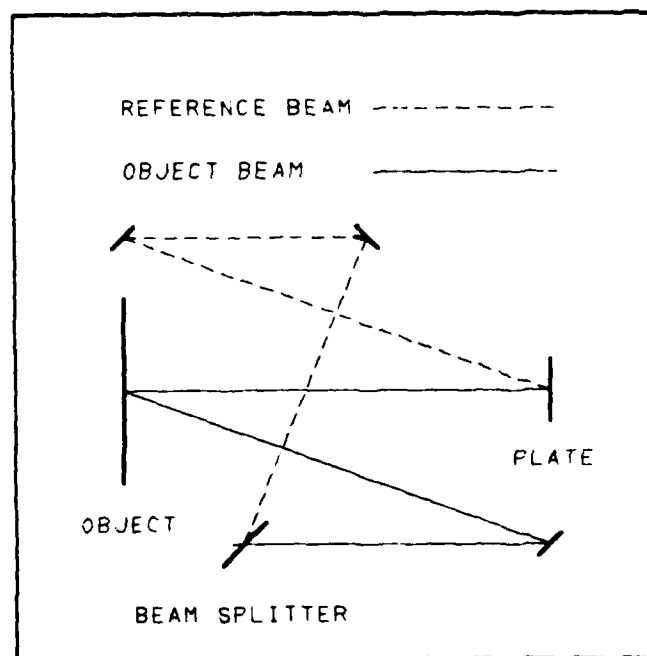


Figure 2.4. Object and Reference Beams

After being split from the original beam, the reference beam is expanded and projected onto the recording plate. Simultaneously, the object beam travels from the beam splitter, is expanded to illuminate the object, and then is reflected from the object to the recording plate as a complex, diffused wave front. Construction of a unique wave front occurs when the two beams interfere at the plate, as seen in Figure 2.5. The exposure of the plate to this wave front results in the recording of a unique image. Viewed alone, this image is unintelligible. It becomes visible again only when the reference beam is superimposed onto it. This reconstruction occurs when the plate and the reference beam are positioned exactly as they were during the initial exposure, as shown in Figure 2.6 [44:6-7].

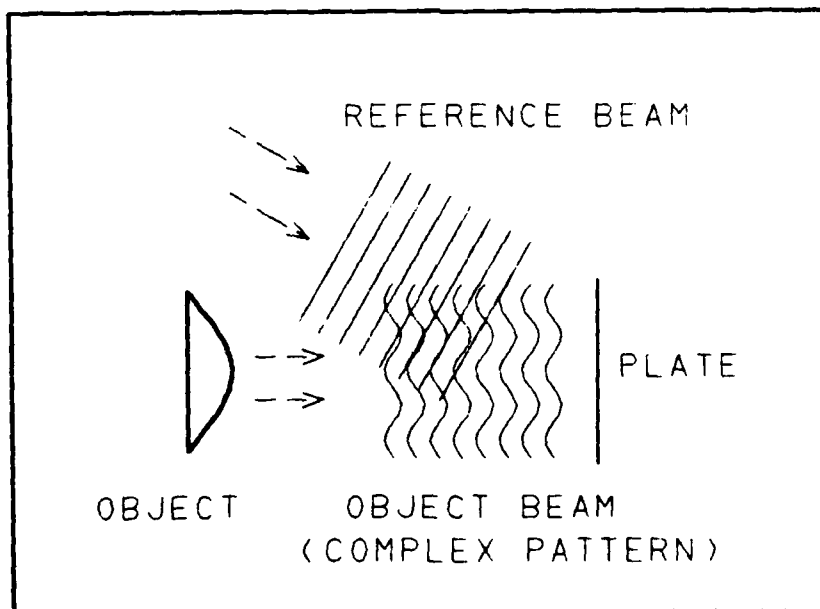


Figure 2.5. Construction of the Hologram by Recording the Object Wave Front [5:8]

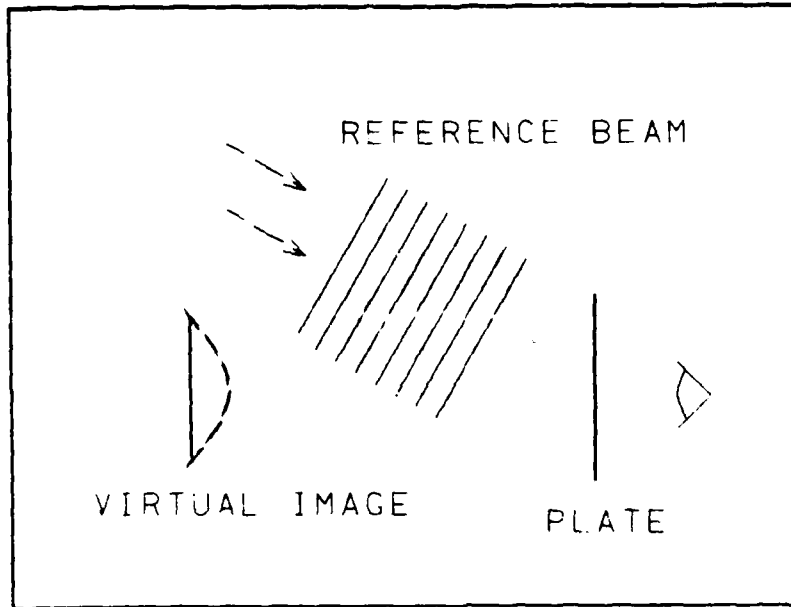


Figure 2.6. Reconstruction of the Object Wave Front Using the Hologram Made in Figure 2.5 [5:8]

A combination of real-time holography and time-average holography is very useful in modal analysis. In real-time holography, an initial hologram is made of the object at rest. Then, using the same optical arrangement and illumination, the virtual image from the static hologram is visually superimposed over the real object as the object vibrates. The reflected wave front continuously changes as the object vibrates. The interference of the reference beam with this changing object wave creates a holographic image of the motion as it occurs, or in "real-time." Real-time holography is useful for observing and identifying the mode

shapes of the object as it vibrates at selected frequencies [44:88,95-96].

Time-average holography allows a particular behavior to be frozen in time and recorded for subsequent study. This is done by recording a hologram of the interference pattern while the object vibrates at one of its natural frequencies. As the object vibrates, it physically spends more time at the two extremes of its displacement cycle, where the direction of motion reverses and the velocity is near zero. The greater relative exposure time creates a hologram dominated by the fringe pattern of the object at its points of extreme displacement [44:88,90]. In real-time holography, the observed displacements are with respect to the object at rest, so that the maximum displacement is as depicted by the distance  $d$  in Figure 2.7a. In contrast, the observed displacements in time-average holography are with respect to the extremes of the displacement cycle, so that maximum displacement is as depicted by the distance  $2d$  in Figure 2.7b. Thus, time-average holograms are generally sharper images. Photographs of time-average holograms provide a useful record of mode shapes.

Combining real-time and time-average holography provides a convenient method for modal analysis. The former process is used to identify natural frequencies and mode shapes by observing the real-time dynamic behavior of the object.

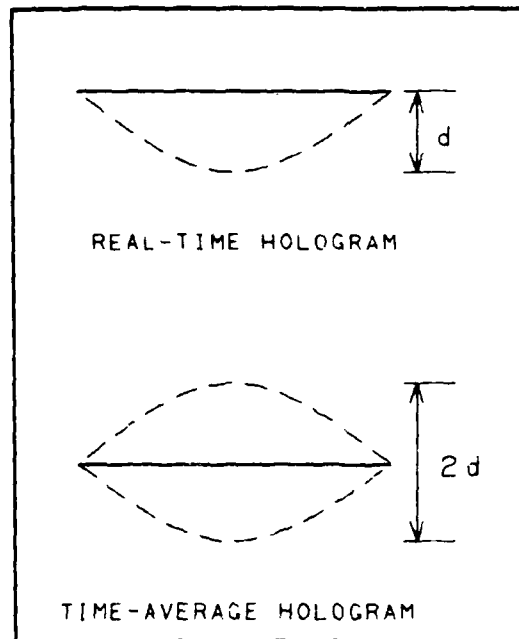


Figure 2.7. (a) Real-time Holography;  
(b) Time-average Holography

When a mode shape is identified, the latter process is used to record the mode shape for subsequent analysis. This combined approach was successfully used to find and record the mode shapes of the composite panels analyzed in this thesis.

#### Lamination Theory

This section describes the macromechanical properties of a composite material. The stiffness matrices and the force, shear, and moment resultants are developed. Stiffness is used when comparing the effects of the repairs made to the panels; stiffness and the resultants are developed in NISA when formulating the finite element problem.

The composite shell element used in NISA includes transverse shear effects and is based on Reissner-Mindlin theory [11:4.48;23;32]. The basic kinematic assumptions for this small-deformation theory are:

(1) The ratio of shell thickness to radius of curvature is small, usually less than or equal to 1:20. The ratio for the composite panels in this thesis is 1:333; therefore the assumption is reasonable [39:198,199].

(2) Deflections are small compared with shell thickness. The deflections observed in this free vibration study are on the order of  $12 \times 10^{-5}$  inches, versus the thickness of the panel which is  $4 \times 10^{-2}$  inches [39:199].

(3) Plane sections normal to the midsurface of the shell before deformation remain straight (no warping) after deformation. These sections do not have to remain normal to the midsurface after deformation, as in the Kirchoff-Love hypothesis. This means that  $\gamma_{xz}$  and  $\gamma_{yz}$ , the shear strains in the normal planes, cannot be neglected. However,  $e_z$ , the normal strain due to transverse loading, is neglected [28:16:304].

(4) Stress normal to the midsurface,  $\sigma_z$ , is neglected as in classical lamination theory [39:199;16:304].

Jones [16] and Calcote [4], among others, present a building-block approach in relating the constitutive, or stress-strain, relationships of individual lamina to the

macromechanical behavior of the total laminate. Lamination theory is based on this assembled behavior of the component laminae. The principal directions, 1, 2, and 3, of an individual lamina are parallel and perpendicular to the direction of its fibers. These directions are related to the principal directions, x, y, and z, of the laminate structure through a coordinate transformation based on the angle  $\theta$  (Figure 2.8).

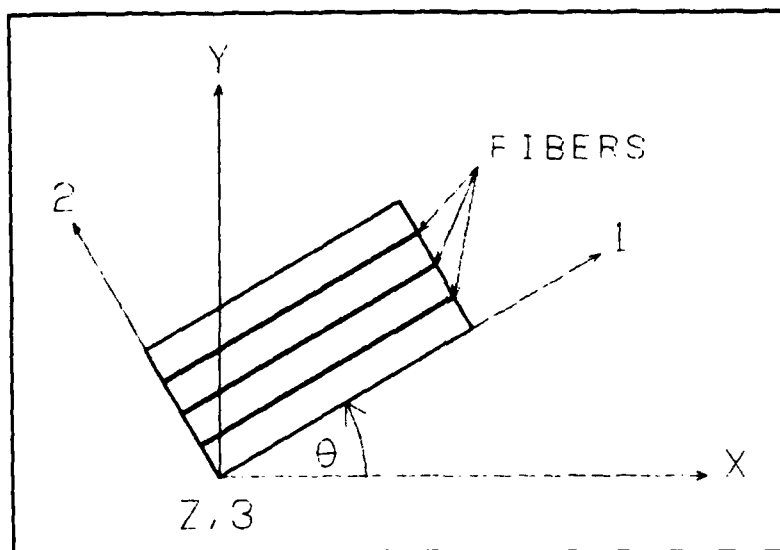


Figure 2.8. Structural (x-y-z) versus Material (1-2-3) Coordinate Systems

The constitutive, or stress-strain, relationships of the individual, orthotropic lamina provide the starting point. These relationships for a single, orthotropic lamina given by

$$\begin{Bmatrix} e_1 \\ e_2 \\ e_3 \\ \gamma_{23} \\ \gamma_{31} \\ \gamma_{12} \end{Bmatrix} = \begin{bmatrix} S_{11} & S_{12} & S_{13} & 0 & 0 & 0 \\ S_{12} & S_{22} & S_{23} & 0 & 0 & 0 \\ S_{13} & S_{23} & S_{33} & 0 & 0 & 0 \\ 0 & 0 & 0 & S_{44} & 0 & 0 \\ 0 & 0 & 0 & 0 & S_{55} & 0 \\ 0 & 0 & 0 & 0 & 0 & S_{66} \end{bmatrix} \begin{Bmatrix} \sigma_1 \\ \sigma_2 \\ \sigma_3 \\ \tau_{23} \\ \tau_{31} \\ \tau_{12} \end{Bmatrix} \quad (2.1)$$

[16:36]

where the elements of the compliance matrix  $[S_{ij}]$  are

$$\begin{aligned}
 S_{11} &= 1/E_1; & S_{12} &= -\nu_{21}/E_2; & S_{13} &= -\nu_{31}/E_3; \\
 S_{22} &= 1/E_2; & S_{23} &= -\nu_{23}/E_2; & S_{33} &= 1/E_3 \\
 S_{44} &= 1/G_{23}; & S_{55} &= 1/G_{31}; & S_{66} &= 1/G_{12}
 \end{aligned} \quad (2.2)$$

[16:38]

and  $E_i$ ,  $\nu_{ij}$ , and  $G_{ij}$  are the Young's Modulus, Poisson's Ratio, and Shear Modulus, respectively, of the orthotropic lamina.

Equation 2.1 can be inverted to give stress  $\{\sigma_{ij}\}$  in terms of strain  $\{e_{ij}\}$  as follows

$$\begin{Bmatrix} \sigma_1 \\ \sigma_2 \\ \sigma_3 \\ \tau_{23} \\ \tau_{31} \\ \tau_{12} \end{Bmatrix} = \begin{bmatrix} Q'_{11} & Q'_{12} & Q'_{13} & 0 & 0 & 0 \\ Q'_{12} & Q'_{22} & Q'_{23} & 0 & 0 & 0 \\ Q'_{13} & Q'_{23} & Q'_{33} & 0 & 0 & 0 \\ 0 & 0 & 0 & Q'_{44} & 0 & 0 \\ 0 & 0 & 0 & 0 & Q'_{55} & 0 \\ 0 & 0 & 0 & 0 & 0 & Q'_{66} \end{bmatrix} \begin{Bmatrix} e_1 \\ e_2 \\ e_3 \\ \gamma_{23} \\ \gamma_{31} \\ \gamma_{12} \end{Bmatrix} \quad (2.3)$$

[28:4]

Having established stress in terms of strain for a single lamina in the material coordinate system (1,2,3), this relationship can be transformed into the laminate coordinate system (x,y,z) by transforming the matrix [Q'] into  $[\bar{Q}']$

$$[\bar{Q}'] = [T]^{-1} [Q'] [T^T]^{-1} \quad (2.4)$$

The transformation matrix [T] is

$$[T] = \begin{bmatrix} m^2 & n^2 & 0 & 0 & 0 & -2mn \\ n^2 & m^2 & 0 & 0 & 0 & 2mn \\ 0 & 0 & 1 & 0 & 0 & 0 \\ 0 & 0 & 0 & m & n & 0 \\ 0 & 0 & 0 & -n & m & 0 \\ mn & -mn & 0 & 0 & 0 & m^2-n^2 \end{bmatrix} \quad (2.5)$$

[28:5]

where  $m = \cos(\theta)$ , and  $n = \sin(\theta)$ , and  $\theta$  is the counterclockwise angle from the structural x-axis to the material 1-axis as depicted in Figure 2.8.

Now, the matrix relating stress to strain becomes  $[\bar{Q}'_{ij}]$  such that

$$\begin{Bmatrix} \sigma_x \\ \sigma_y \\ \sigma_z \\ \tau_{yz} \\ \tau_{xz} \\ \tau_{xy} \end{Bmatrix} = \begin{bmatrix} \bar{Q}'_{11} & \bar{Q}'_{12} & \bar{Q}'_{13} & 0 & 0 & 0 \\ \bar{Q}'_{12} & \bar{Q}'_{22} & \bar{Q}'_{23} & 0 & 0 & 0 \\ \bar{Q}'_{13} & \bar{Q}'_{23} & \bar{Q}'_{33} & 0 & 0 & 0 \\ 0 & 0 & 0 & \bar{Q}'_{44} & 0 & 0 \\ 0 & 0 & 0 & 0 & \bar{Q}'_{55} & 0 \\ 0 & 0 & 0 & 0 & 0 & \bar{Q}'_{66} \end{bmatrix} \begin{Bmatrix} e_x \\ e_y \\ e_z \\ \gamma_{yz} \\ \gamma_{xz} \\ \gamma_{xy} \end{Bmatrix} \quad (2.6)$$

[28:5]

Plane stress applies since each lamina is thin [33:226]. Recalling assumption (4), that stresses normal to the mid-surface are negligible, then the following applies from Equation 2.6

$$\sigma_z = \bar{Q}'_{13}e_x + \bar{Q}'_{23}e_y + \bar{Q}'_{33}e_z + \bar{Q}'_{66}\gamma_{xy} = 0 \quad (2.7)$$

from which

$$e_z = (\bar{Q}'_{13}/\bar{Q}'_{33})e_x + (\bar{Q}'_{23}/\bar{Q}'_{33})e_y + (\bar{Q}'_{66}/\bar{Q}'_{33})\gamma_{xy} \quad (2.8)$$

Now, recalling assumption (3) that  $e_z$ , while not zero, is considered negligible for a thin shell, and substituting back into Equation 2.6, the  $[\bar{Q}']$  matrix degenerates to the following transformed reduced stiffness matrix  $[\bar{Q}]$

$$[\bar{Q}_{ij}] = \begin{bmatrix} \bar{Q}_{11} & \bar{Q}_{12} & 0 & 0 & \bar{Q}_{16} \\ \bar{Q}_{12} & \bar{Q}_{22} & 0 & 0 & \bar{Q}_{26} \\ 0 & 0 & \bar{Q}_{44} & \bar{Q}_{45} & 0 \\ 0 & 0 & \bar{Q}_{45} & \bar{Q}_{55} & 0 \\ \bar{Q}_{16} & \bar{Q}_{26} & 0 & 0 & \bar{Q}_{66} \end{bmatrix} \quad (2.9)$$

[28:6]

where the elements are defined by

$$\begin{aligned} \bar{Q}_{11} &= Q_{11}m^4 + 2(Q_{12} + 2Q_{66})n^2m^2 + Q_{22}n^4 \\ \bar{Q}_{12} &= (Q_{11} + Q_{22} - 4Q_{66})n^2m^2 + Q_{12}(n^4 + m^4) \\ \bar{Q}_{22} &= Q_{11}n^4 + 2(Q_{12} + 2Q_{66})n^2m^2 + Q_{22}m^4 \\ \bar{Q}_{16} &= (Q_{11} - Q_{12} - 2Q_{66})nm^3 + (Q_{12} - Q_{22} + 2Q_{66})n^3m \\ \bar{Q}_{26} &= (Q_{11} - Q_{12} - 2Q_{66})n^3m + (Q_{12} - Q_{22} + 2Q_{66})nm^3 \end{aligned} \quad (2.10)$$

$$\bar{Q}_{44} = Q_{44}m^2 + Q_{55}n^2$$

$$\bar{Q}_{45} = (Q_{44} - Q_{55})mn$$

$$\bar{Q}_{55} = Q_{55}m^2 + Q_{44}n^2$$

$$\bar{Q}_{66} = (Q_{11} + Q_{22} - 2Q_{12} - 2Q_{66})n^2m^2 + Q_{66}(n^4 + m^4)$$

[28:6]

for  $n = \sin(\theta)$  and  $m = \cos(\theta)$ , as previously defined, and the components of the reduced stiffness matrix  $[Q_{ij}]$  are defined as

$$\begin{aligned}
Q_{11} &= E_1/(1-\nu_{12}\nu_{21}) \\
Q_{12} &= \nu_{12}E_2/(1-\nu_{12}\nu_{21}) \\
Q_{22} &= E_2/(1-\nu_{12}\nu_{21}) \\
Q_{44} &= G_{23} \\
Q_{55} &= G_{31} \\
Q_{66} &= G_{12}
\end{aligned}
\tag{2.11}$$

[28:7]

Applying the transformed reduced stiffness matrix  $[\bar{Q}_{ij}]$ , the stress-strain relationships for the laminate become

$$\begin{Bmatrix} \sigma_x \\ \sigma_y \\ \tau_{yz} \\ \tau_{xz} \\ \tau_{xy} \end{Bmatrix} = \begin{bmatrix} \bar{Q}_{11} & \bar{Q}_{12} & 0 & 0 & \bar{Q}_{16} \\ \bar{Q}_{12} & \bar{Q}_{22} & 0 & 0 & \bar{Q}_{26} \\ 0 & 0 & \bar{Q}_{44} & \bar{Q}_{45} & 0 \\ 0 & 0 & \bar{Q}_{45} & \bar{Q}_{55} & 0 \\ \bar{Q}_{16} & \bar{Q}_{26} & 0 & 0 & \bar{Q}_{66} \end{bmatrix} \begin{Bmatrix} e_x \\ e_y \\ \gamma_{yz} \\ \gamma_{xz} \\ \gamma_{xy} \end{Bmatrix}
\tag{2.12}$$

[28:7]

Having established the stress-strain relationships that include transverse shear, the force, shear, and moment resultants can now be obtained by integrating the stresses on each layer through the laminate thickness,  $t$ . The resulting forces, shears, and moments-per-unit length are, respectively,

$$\begin{Bmatrix} N_x \\ N_y \\ N_{xy} \end{Bmatrix} = \int_{-t/2}^{t/2} \begin{Bmatrix} \sigma_x \\ \sigma_x \\ \tau_{xy} \end{Bmatrix} dz = \sum_{k=1}^N \int_{z_{k-1}}^{z_k} \begin{Bmatrix} \sigma_x \\ \sigma_x \\ \tau_{xy} \end{Bmatrix} dz \quad (2.13)$$

$$\begin{Bmatrix} Q_x \\ Q_y \end{Bmatrix} = \int_{-t/2}^{t/2} \begin{Bmatrix} \tau_{xz} \\ \tau_{yz} \end{Bmatrix} dz = \sum_{k=1}^N \int_{z_{k-1}}^{z_k} \begin{Bmatrix} \tau_{xz} \\ \tau_{yz} \end{Bmatrix} dz \quad (2.14)$$

$$\begin{Bmatrix} M_x \\ M_y \\ M_{xy} \end{Bmatrix} = \int_{-t/2}^{t/2} \begin{Bmatrix} \sigma_x \\ \sigma_x \\ \tau_{xy} \end{Bmatrix} z dz = \sum_{k=1}^N \int_{z_{k-1}}^{z_k} \begin{Bmatrix} \sigma_x \\ \sigma_x \\ \tau_{xy} \end{Bmatrix} z dz \quad (2.15)$$

where  $t$  is the total laminate thickness and  $N$  is the total number of layers (or plies) in the laminate (Figure 2.12).

The force, shear, and moment resultants given above are depicted in Figures 2.9 through 2.11.

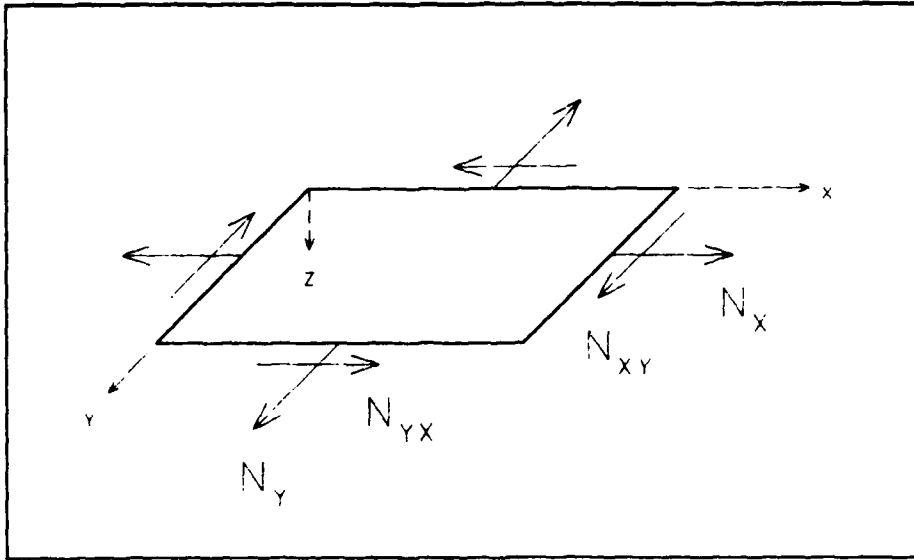


Figure 2.9. In-Plane Force Resultants [39:232]

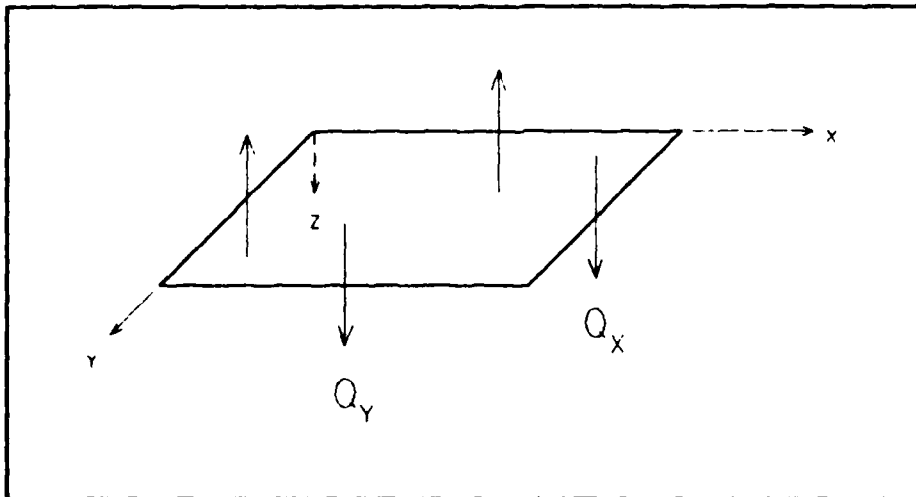


Figure 2.10. Shear Resultants [39:232]

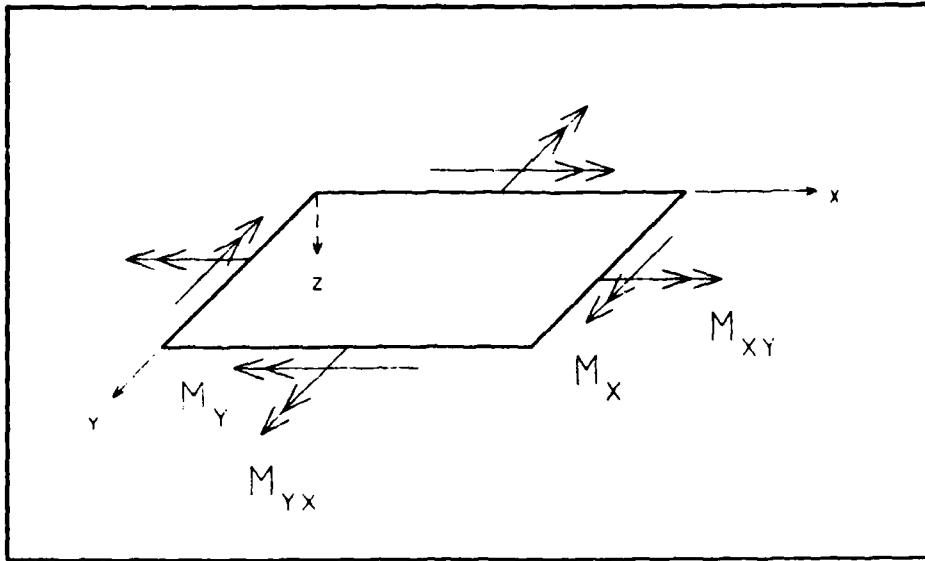


Figure 2.11. Moment Resultants (39:232)

The limits of integration,  $z_{k-1}$  to  $z_k$ , are defined in Figure 2.12, which depicts laminate with  $N$  layers, total thickness  $t$ , and  $z_0 = -t/2$ . Because the stiffness matrix is constant within the lamina, it can be moved outside the integral but within the summation of force, shear, and moment resultants for each layer [16:153]. Substituting Equation 2.12, the resultants can be written as

$$\begin{Bmatrix} N_x \\ N_y \\ N_{xy} \end{Bmatrix} = \sum_{k=1}^N \begin{bmatrix} \bar{Q}_{11} & \bar{Q}_{12} & \bar{Q}_{16} \\ \bar{Q}_{12} & \bar{Q}_{22} & \bar{Q}_{26} \\ \bar{Q}_{16} & \bar{Q}_{26} & \bar{Q}_{66} \end{bmatrix} \int_{z_{k-1}}^{z_k} \begin{Bmatrix} e_x \\ e_y \\ \gamma_{xy} \end{Bmatrix} dz \quad (2.16)$$

$$\begin{Bmatrix} Q_x \\ Q_y \end{Bmatrix} = \sum_{k=1}^N \begin{bmatrix} \bar{Q}_{44} & \bar{Q}_{45} \\ \bar{Q}_{45} & \bar{Q}_{55} \end{bmatrix} \int_{z_{k-1}}^{z_k} \begin{Bmatrix} \gamma_{yz} \\ \gamma_{xz} \end{Bmatrix} dz \quad (2.17)$$

$$\begin{Bmatrix} M_x \\ M_y \\ M_{xy} \end{Bmatrix} = \sum_{k=1}^N \begin{bmatrix} \bar{Q}_{11} & \bar{Q}_{12} & \bar{Q}_{16} \\ \bar{Q}_{12} & \bar{Q}_{22} & \bar{Q}_{26} \\ \bar{Q}_{16} & \bar{Q}_{26} & \bar{Q}_{66} \end{bmatrix} \int_{z_{k-1}}^{z_k} \begin{Bmatrix} e_x \\ e_y \\ \gamma_{xy} \end{Bmatrix} z dz \quad (2.18)$$

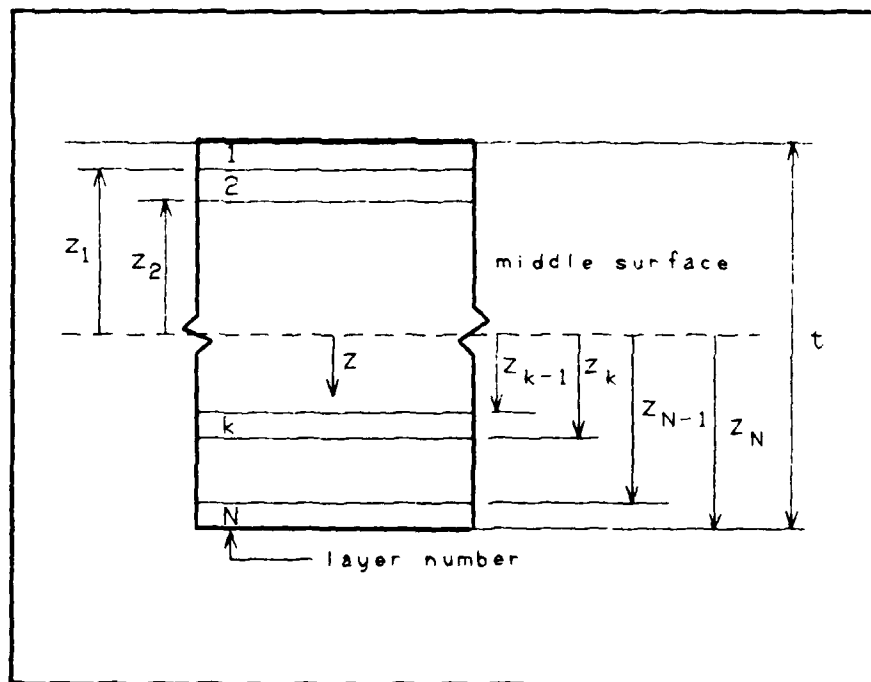


Figure 2.12. Geometry of an N-Layered Laminate [16:154]

Next, the force, shear, and moment resultants are written in terms of displacements by using the strain-displacement relationships. These are significantly more complex for a shell than for a flat plate, although some simplification can be done for the cylindrical panel. Several shell theories that include transverse shear effects have been advanced to describe these strain-displacement relationships, including the higher-order theories presented by Whitney and Sun [47;48]. Sander's equations, Reddy's modification of Sander's theory [30], and Donnell's assumptions for thin shells [28:4] simplify these relationships, yet provide reliable solutions for small deformation problems.

The Donnell assumptions apply to composite shells when the ratio of the thickness to the radius of curvature is less than approximately 1:50 [28:4]. Applying this approach, the behavior of any point in a cylindrical shell can be described by  $u$ ,  $v$ , and  $w$ , the displacements in the  $x$  (meridional),  $y$  (tangential), and  $z$  (radial) directions (Figure 2.13).

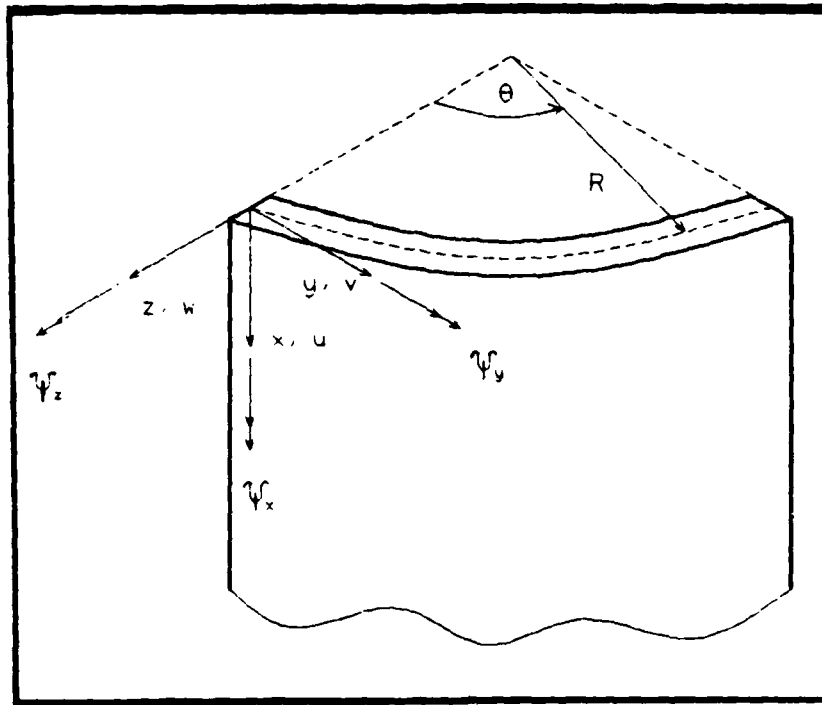


Figure 2.13. Panel Coordinate System and Displacements

Now, the total displacements are defined by

$$\begin{aligned}
 u &= u^0 - z\psi_x \\
 v &= v^0 - z\psi_y \\
 w &= w
 \end{aligned}
 \tag{2.19}$$

where  $u^0$  and  $v^0$  are the displacements in the  $x$ - and  $y$ -directions at the midsurface of the panel ( $z = 0$ ); and  $\psi_x$  and  $\psi_y$  describe the rotations, with respect to the midsurface, of elements in the  $yz$ - and  $xz$ - planes due to bending. Applying the strain-displacement relationships in cylindrical coordinates (neglecting higher-order terms), the strains are defined as partial derivatives of the displacement terms as follows

$$e_x = u_{,x}; \quad e_y = v_{,y} + w/r; \quad e_z = w_{,z}; \quad (2.20)$$

$$\gamma_{xy} = v_{,x} + u_{,y}; \quad \gamma_{xz} = w_{,x} + u_{,z}; \quad \gamma_{yz} = w_{,y} + v_{,z} - v/r$$

[33:138-9]

where the subscript ,i denotes the partial derivative with respect to i. Substituting Equations 2.19 into Equations 2.20 and recalling that the midsurface displacements,  $u_0$  and  $v_0$ , and the rotations,  $\psi_x$  and  $\psi_y$ , are functions of  $x$  and  $y$  only, the strains in terms of midsurface displacements and rotations are

$$e_x = u_0_{,x} - z\psi_{x,x}$$

$$e_y = v_0_{,y} - z\psi_{y,y} + w/r$$

$$e_z = w_{,z} = 0 \text{ (as previously assumed)}$$

$$\gamma_{xy} = u_0_{,y} + v_0_{,x} - z(\psi_{x,y} + \psi_{y,x}) \quad (2.21)$$

$$\gamma_{xz} = w_{,x} - \psi_x$$

$$\gamma_{yz} = w_{,y} - \psi_y - v/r$$

Substituting Equation 2.21 into Equations 2.16 through 2.18, and carrying out the integration, the force, shear, and moment resultants can be expressed as

$$\begin{Bmatrix} N_x \\ N_y \\ Q_x \\ Q_y \\ N_{xy} \\ M_x \\ M_y \\ M_{xy} \end{Bmatrix} = \begin{bmatrix} A_{11} & A_{12} & 0 & 0 & A_{16} & B_{11} & B_{12} & B_{16} \\ A_{12} & A_{22} & 0 & 0 & A_{26} & B_{12} & B_{22} & B_{26} \\ 0 & 0 & A_{44} & A_{45} & 0 & 0 & 0 & 0 \\ 0 & 0 & A_{45} & A_{55} & 0 & 0 & 0 & 0 \\ A_{16} & A_{26} & 0 & 0 & A_{66} & B_{16} & B_{26} & B_{66} \\ B_{11} & B_{12} & 0 & 0 & B_{16} & D_{11} & D_{12} & D_{16} \\ B_{12} & B_{22} & 0 & 0 & B_{26} & D_{12} & D_{22} & D_{26} \\ B_{16} & B_{26} & 0 & 0 & B_{66} & D_{16} & D_{26} & D_{66} \end{bmatrix} \begin{Bmatrix} u^0, x \\ v^0, y + w/r \\ w, x - \psi_x \\ w, y - \psi_y - v/r \\ u^0, y + v^0, x \\ -\psi_{x, x} \\ -\psi_{y, y} \\ -(\psi_{x, y} + \psi_{y, x}) \end{Bmatrix}$$

(2.22)

where  $A_{ij}$  are extensional stiffnesses defined as

$$A_{ij} = \sum_{k=1}^N (\bar{Q}_{ij})_k (z_k - z_{k-1}) \quad (2.23)$$

with the exception that  $A_{44}$ ,  $A_{45}$ , and  $A_{55}$  are defined as

$$A_{ij} = K \int_{-t/2}^{t/2} (\bar{Q}_{ij}) dz \quad (2.24)$$

and  $K = 5/6$  to account for the parabolic distribution of shear through the thickness,  $t$ , of the panel [28:2,8].  $B_{ij}$  are coupled stiffnesses defined as

$$B_{ij} = 1/2 \sum_{k=1}^N (\bar{Q}_{ij})_k (z_k^2 - z_{k-1}^2) \quad (2.25)$$

and  $D_{ij}$  are bending stiffnesses defined as

$$D_{ij} = 1/3 \sum_{k=1}^N (\bar{Q}_{ij})_k (z^3_k - z^3_{k-1}) \quad (2.26)$$

where  $k$  is the lamina number,  $N$  is the total number of laminae in the laminate, and  $z$  is the distance from the laminate midsurface to the  $k^{\text{th}}$  lamina.

It has been shown that transverse shear deformation effects can be incorporated in a relatively simple approach. It should be noted that including shear deformation is a more rigorous approach; however, the effects of shear on a thin shell structure are usually neglected in favor of other acceptable solutions at less computational expense. This is evident by the popularity of the Kirchoff-Love hypothesis, which is the basis of the very accurate STAGSC-1 elements used by Cyr and Walley. Two of the three NISA elements used in this thesis, however, do not use the Kirchoff-Love hypothesis. Instead, they retain transverse shear and account for minimal through-the-thickness effects by using a reduced integration technique to solve for the element stiffness matrices [11:4.37,4.48]. This is discussed more thoroughly in Appendix D.

## Finite Element Theory

This section presents an overview of the finite element theory used by NISA to solve free vibration problems. Specifically, it describes how the eigenvalue problem is developed and solved with finite elements. Appendix D summarizes the formulation of the isoparametric elements that are used by NISA in the development of this problem.

The governing equation for a body in vibration is derived from Newton's Second Law, which can be written

$$M\ddot{x}(t) + C\dot{x}(t) + Kx(t) = F(t) \quad (2.27)$$

where

M = mass of body

C = damping

K = stiffness coefficient

x(t) = displacement

$\dot{x}(t)$  = velocity

$\ddot{x}(t)$  = acceleration

F(t) = external force

The essence of a finite element solution to this problem is to discretize the properties of the continuous body in terms of displacements at individual locations, or nodes, within the body. Thus, Equation 2.27 can be rewritten as

$$[M]\{\ddot{d}\} + [C]\{\dot{d}\} + [K]\{d\} = \{F(t)\} \quad (2.28)$$

where

- [M] = mass matrix
- [C] = damping matrix
- [K] = stiffness matrix
- {d} = displacement vector
- $\dot{\{d\}}$  = velocity vector
- $\ddot{\{d\}}$  = acceleration vector
- {F(t)} = external force vector

The external forces, {F(t)}, acting on a body in free vibration are zero. Damping is also assumed to be negligible. This is because structural damping is based on energy losses due to internal friction, or hysteresis effects, which are proportional to the amplitude of displacement. Since the displacements for the high stiffness, low mass composite panels used in this thesis are infinitesimal, it follows that damping can be neglected [21:72]. Thus, Equation 2.28 becomes

$$[M]\{\ddot{d}\} + [K]\{d\} = 0 \quad (2.29)$$

Assuming the free vibrations are harmonic, the displacements can be written

$$\{d\} = \{d_0\} \sin(\omega t) \quad (2.30)$$

Substituting this into Equation 2.29 yields

$$[K]\{d_0\} - \omega^2[M]\{d_0\} = 0 \quad (2.31)$$

$$\text{or } [[K] - \lambda[M]] d_0 = 0 \quad (2.32)$$

where the  $\lambda$ s are the eigenvalues and the  $\{d_0\}$ s are the eigenvectors or mode shapes. NISA uses a subspace iteration technique to solve Equation 2.32 for the eigenvalues and eigenvectors that define the natural frequencies and mode shapes (11:2.11,2.14,2.15).

### III. Composite Panels

This chapter presents the geometric and material properties of the five graphite/epoxy test panels, and describes the repairs made to these panels. The solid panel provided a baseline against which the effects of the cutouts and the repairs on the other four panels are compared.

#### Composite Panel Properties

The five cylindrically curved, square, composite panels were made of Hercules AS4/3501-6 graphite/epoxy. Cyr used the same panels [7]. They had the same material and geometric properties as Walley's panels in his modal analysis [42] and as Tisler's panels in his buckling analysis [38]. Each panel had a  $[0/-45/45/90]_s$  quasi-isotropic lay-up.

Cyr documented the analysis of the fibers and the resin by Hercules, and the manufacturing process performed by the Flight Dynamics Laboratory's Composites Shop [7]. The material properties were presented in Table 3.1. The two out-of-plane shear moduli,  $G_{23}$  and  $G_{31}$ , were not reported by Cyr, since they were not required in the STAGSC-1 finite element program he used. NISA, however, required these properties.  $G_{31}$  was taken to be equal to  $G_{12}$  by assuming that the ratios of fiber area to matrix area in the lamina principal 2- and 3-directions were equal. This transverse isotropy is depicted in Figure 3.1.

$G_{23}$  was assumed to be 80% of  $G_{12}$ . Since  $G_{23}$  could not be determined directly, the common practice of assuming that it was between 50%-80% of  $G_{12}$  was followed. The analytical results from NISA showed less than 1% difference between using 50% or 80%, so the higher value was used because of its prevalence in the literature.

Table 3.1. Material Properties of the Panels

$E_1$	=	$18.84 \times 10^6$	psi
$E_2$	=	$1.468 \times 10^6$	psi
$G_{12}$	=	$0.9099 \times 10^6$	psi
$G_{23}$	=	$0.9099 \times 10^6$	psi
$G_{31}$	=	$0.7279 \times 10^6$	psi
$\nu_{12}$	=	0.2799	
$\nu_{21}$	=	0.0218	
$\rho$	=	$1.5162 \times 10^{-4}$	lbf-sec <sup>2</sup> /in <sup>4</sup>

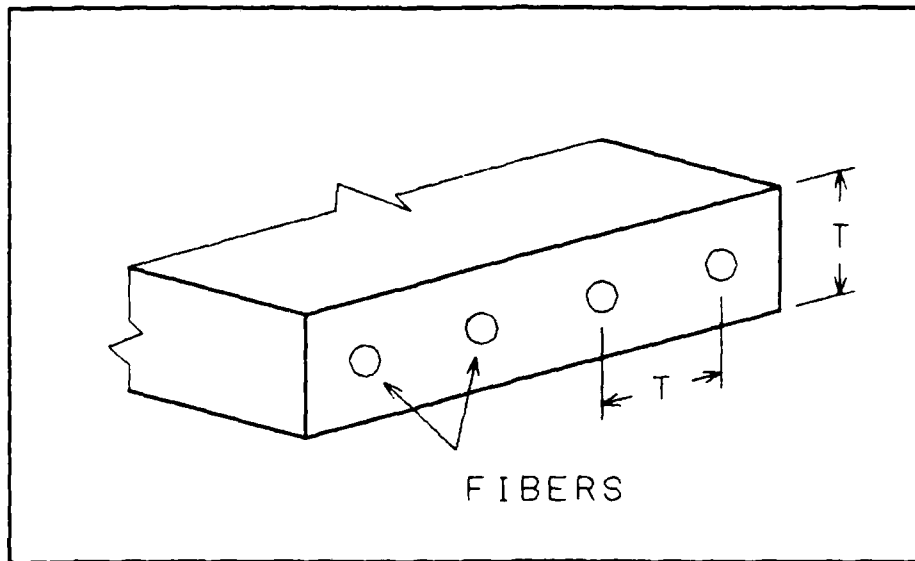


Figure 3.1. Ratio of Fiber Area to Matrix Area

The overall geometry of each panel was the same, except for the interior cutouts. The radius of curvature was 12 inches, the arc length was 15.88 inches, the chord length was 14.75 inches, and the panel height was 16 inches. Average ply thickness was 0.005 inches, for an eight-ply laminate thickness of 0.040 inches. Figure 3.2 depicts the panel geometry.

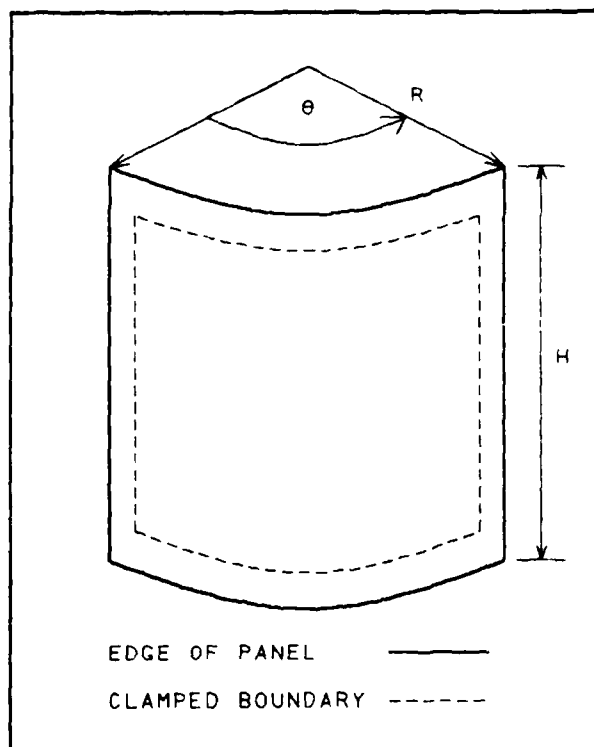


Figure 3.2. Panel Geometry

When mounted in the test fixture, the unclamped or free region of the panel was smaller. The radius of curvature did not change because the fixture was machined to match the 12-inch radius. The arc length of the unclamped region of the panel, however, was 12.19 inches, the chord length was 11.67 inches, and the height was 12.0 inches. These geometric properties were used in designing the finite element model.

### Repairs

A simple repair consisting of an aluminum patch riveted over the cutout area was made to each panel. The design of the patch was based on guidelines recommended by Stone in his work on field-level repairs for Lockheed [37], by Myhre in Northrop's report to the Air Force on composite repairs [25], and in the most recent F-16 Battle Damage Repair Manual [8]. It was representative of an aircraft battle damage repair that could be made with the materials, tools, and skill available at the field level. Its function was to seal the structure and restore stiffness so that the aircraft could continue in battle or be flown to a rear depot for more sophisticated repairs. It was neither a permanent repair nor a repair designed to restore original strength to a primary load-bearing structure.

Patch Material Properties. The patch was formed from type 2024-T3 aluminum sheet, a tough, heat-treatable Al-Cu

alloy [9]. Stone, Myhre, and the Air Force F-16 Battle Damage Repair Manual each cite 2024-T3 as a suitable and commonly available material for field-type repairs to composite structures. The mechanical fasteners were Cherry Aerospace Fasteners made by the Cherry Division of Textron. Specific properties of the repair materials are presented in Table 3.2.

Table 3.2. Properties of the Patch Materials

Aluminum Patch (Al-Cu)

Designation	2024 Aluminum Alloy
Specification	QQ-A-250/4
Temper/Form	T3/Sheet
Young's Modulus, E	$10.5 \times 10^6$ psi
Poisson's Ratio, $\nu$	0.33
Density, $\rho$	0.101 lb/in <sup>3</sup>
Thickness, t	0.032 in

[9]

Fasteners

Designation	Cherry Aerospace Fasteners
MS Number	M7885/2-4-02
Part Number	CR3213-04-02
Nominal Size	0.125 in
Hole Size	0.129-0.132 in
Grip Size	0.063-0.125 in

[Cherry Textron Package]

The patch was designed to cover the cutout area with sufficient overlap for the fastener arrangement described in the next section. The patch thickness was selected to minimize loss of structural stiffness of the panel, a primary consideration in the design of repairs for secondary structures [25]. This selection was based on a comparison of the

stiffness of the isotropic aluminum patch with effective stiffness of the quasi-isotropic composite laminate panel. Young's modulus,  $E$ , for the aluminum was known. An equivalent  $E$  for the composite panel had to be determined. This was done by using the results of the laminated plate theory presented in Chapter II.

For balanced, symmetric laminates such as these panels, the following equations hold

$$E_x = (A_{11}A_{22} - A_{12}^2) / tA_{22} \quad (3.1)$$

$$E_y = (A_{11}A_{22} - A_{12}^2) / tA_{11} \quad (3.2)$$

$$\nu_{xy} = A_{12} / A_{22} \quad (3.3)$$

$$\nu_{yx} = A_{12} / A_{11} \quad (3.4)$$

$$G_{xy} = A_{66} / t \quad (3.5)$$

[28]

The extensional stiffness matrix  $[A_{ij}]$  was defined in Equation 2.23 as a function of the transformed reduced stiffness matrix  $[\bar{Q}_{ij}]$  and the lay-up geometry. Using Equation 2.23, which is repeated here

$$[A_{ij}] = \sum_{k=1}^N [\bar{Q}_{ij}]_k (z_k - z_{k-1}) \quad (2.23)$$

the components of  $[A_{ij}]$  can be calculated and substituted into Equations 3.1 through 3.5 to obtain the effective engineering properties of the composite laminate. In addition, the quasi-isotropic nature of these panels is

confirmed since  $A_{16} = A_{26} = 0$  [28]. The resulting effective laminate engineering properties are given in Table 3.3.

Table 3.3. Effective Engineering Properties of the Panels

$$E_x = 7.515 \times 10^3 \text{ ksi}$$

$$E_y = 7.515 \times 10^3 \text{ ksi}$$

$$\nu_{xy} = 0.293$$

$$\nu_{yx} = 0.293$$

$$G_{xy} = 2.906 \times 10^3 \text{ ksi}$$

The thickness selected for the patch was based on using nominal stock aluminum while retaining, as much as possible, the original mass, stiffness, and flexural rigidity of the panel. The total mass change of the panel due to the repair was calculated as follows:

$$dm_t = m_p - m_c \quad (3.5)$$

where,

$$m_p = \rho_p \times V_p \quad (3.6)$$

and,

$$m_c = \rho_c \times V_c \quad (3.7)$$

and where  $dm_t$  is the total mass change of the panel;  $m_p$ ,  $\rho_p$ , and  $V_p$  are the mass, density, and volume of the patch, respectively; and  $m_c$ ,  $\rho_c$ , and  $V_c$  are similar properties of the composite material removed by the cutout. The calculated mass change,  $dm_t$ , represented a 13% increase before the mass of the rivets was considered. Adding the rivet

mass changed this to an 85% increase in total mass of the panel. This was significant, as the rivets added little to the stiffness of the panel since they were point masses and served only to fasten the aluminum patch to the composite panel. Since the natural frequencies of a structure are proportional to the square root of the stiffness over the mass, the significant mass contribution and negligible stiffness contribution of the rivets should cause a decrease in the panel's natural frequencies.

The change in overall panel stiffness had to be considered. The elastic stiffness due to the repair should differ with location on the panel. In the cutout area, the new elastic stiffness is simply Young's modulus for the aluminum patch, or  $10.5 \times 10^3$  ksi. The equivalent stiffness for the quasi-isotropic composite material was previously calculated to be  $7.5 \times 10^3$  ksi. In the area where the patch overlaps the composite, the effective Young's modulus was calculated with a method similar to the rule of mixtures approach used in determining material properties of a composite lamina based on the properties of its constituent fibers and matrix [16]. This approach calculated the contribution of the stiffness of the aluminum and the stiffness of the composite material in proportion to their respective stiffnesses and areas. The result was an estimated effective stiffness in the overlap area of  $8.8 \times 10^3$  ksi. Thus, the cutout area was

stiffened by 40%, while the overlap area was stiffened by 18%.

Another important property was the flexural rigidity of the panel. This property influenced the behavior of the panel as it vibrated normal to its midsurface. It was determined by the following equation

$$D = Et^3/12(1-\nu^2) \quad (3.8)$$

[39]

Using the material properties of the aluminum and the effective material properties of the patch and the overlap area, the following flexural rigidities were calculated

Composite panel,  $D = 43.84$  in-lb

Aluminum patch,  $D = 32.18$  in-lb

Overlap area,  $D = 304.13$  in-lb

Thus, the area of the cutout replaced with the aluminum had 27% less flexural rigidity. In contrast, the overlap area had a 594% increase in flexural rigidity. This was largely due to the thickness, which was nearly doubled in this area. The cube of the thickness term in the numerator of Equation 3.8 caused this great increase of rigidity in the area around the original cutout.

Patch Geometry. The patch size and rivet pattern were based on accepted practices for mechanically fastened repairs [25;8]. Rivet spacing was four times the rivet

diameter in a single row around the cutout. The rivets were four diameters from the cutout edge and two diameters from the outer edge of the patch. A 3.5-inch by 5.5-inch patch was needed to accommodate this rivet pattern. The patches were pre-rolled to match the curvature of the panel. This reduced the tendency of the patch to straighten the panel or put added stress on the rivets in the direction normal to the patch. Figure 3.3 shows the patch geometry, while Figures 3.4 and 3.5 are examples of the actual patch fastened to the panel. The patches differed only in the direction of curvature, which had to be oriented in the direction of the cutout being repaired.

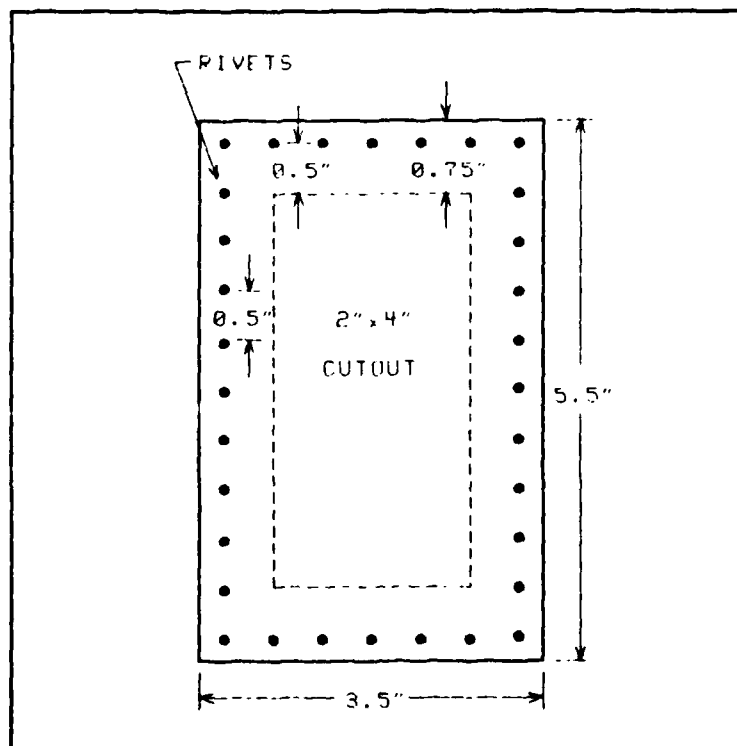


Figure 3.3. Repair Patch Geometry

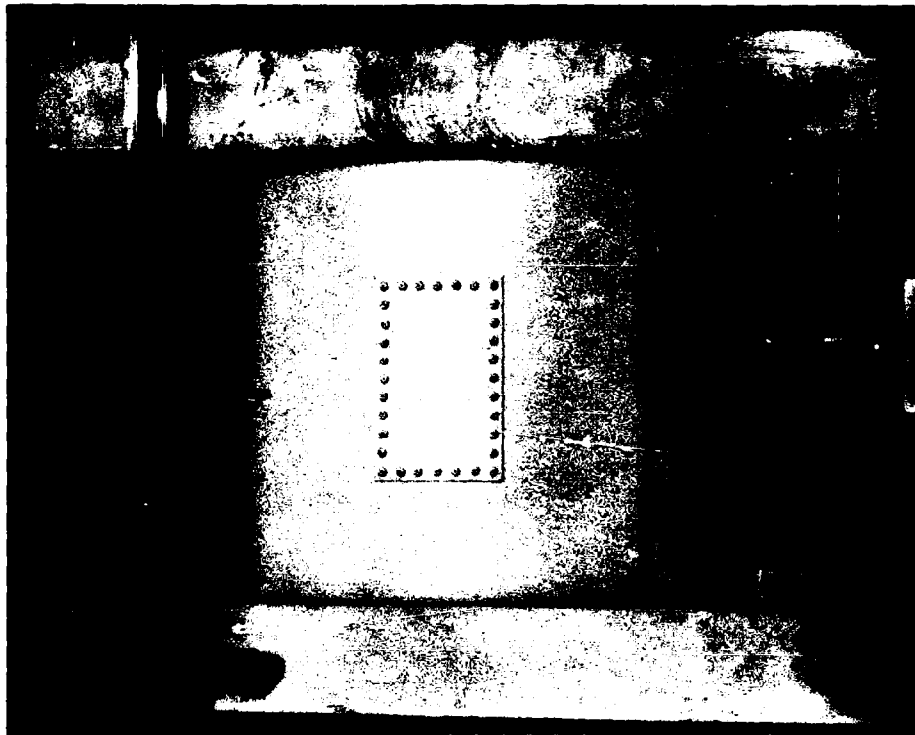


Figure 3.4. Typical Repair Patch (Front)



Figure 3.5. Typical Repair Patch (Back)

Repair Technique. The repairs were done in the Flight Dynamics Laboratory Composite Shop. The technique was developed with the advice of shop personnel. It was based on standards presented in the F-16A ABDR Manual and in Northrop's Advanced Composite Repair Guide [8;25]. Common hand tools were used. One artificiality was the use of a jig for drilling the holes. This jig was the same one used for making the cutouts in Cyr's panels. By using it to support the panel when the holes were drilled, backside breakout was nearly eliminated. In a field environment where a structure is often repaired on the aircraft, similar access to the backside of a damaged area may not be available. McDonnell-Douglas recently reported a technique to minimize breakout damage when the backside is not accessible [12]. This technique, however, was not used. Instead, the jig was used to minimize damage to the thin test panels.

The 3 1/2-inch by 5 1/2-inch patches were cut from 2024-T3 aluminum sheet stock. The rivet pattern was laid out on the patches. A center punch and hammer were used to make pilot holes for drilling. Each patch was then rolled by hand to match the curvature of the panel as closely as possible. A 6 1/2-inch solid aluminum cylinder was used for this. Each patch was manually held onto the cylinder, which was then rolled on a flat table top to force a curve into the patch. When pressure was released from the patch, it

sprung back, but not to its original flat geometry. Several iterations of this process gradually introduced a curve that conformed to that of the panel.

Specifically, the patches for the 0° and 90° cutout panels matched the curvature of the respective panels very accurately. The +45° patch was slightly less accurate, although it had a consistent curvature overall. The -45° patch was not as true at the corners and was the least accurate patch. It did, however, generally conform to the panel.

Once the patch was curved, it was centered over the cut-out area of the panel. A high-speed drill and a 1/8-inch carbide drill bit were used to drill an initial hole simultaneously through the patch and the composite material. The 1/8-inch rivet had a 0.129-0.132-inch tolerance. Thus, the initial 1/8-inch hole was 0.004-0.007 inches too small and the rivet could not be forced through without damaging the hole. A number 28 high-speed drill bit was used to finish the hole to accommodate the rivet. It would have been more efficient to drill the hole to size in one operation. However, a number 28 carbide bit was not available. The tougher carbide bit is essential in drilling composites, which rapidly wear out normal steel bits. Therefore, the next smallest available carbide bit was used to do the bulk

of the drilling and the softer high-speed drill merely reamed out the hole to the proper size.

Once the holes were drilled and cleaned, the patch was fastened to the panel with the Cherry Aerospace Fasteners (rivets). A standard hand-operated rivet gun was used. The panel was then inspected for loose rivets that would have indicated poor installation [12].

In each case, no loose rivets or significant breakout damage was found, indicating that the patch was fastened as well as could be expected with resources similar to those available in an ABDR environment. The main area of concern was the inability to get a good curve fit for the +45° and -45° patches. The corners of these patches were very difficult to roll down and bring in line with the overall panel curvature. Some initial stress at the corners was suspected.

Overall, the repairs were relatively simple to make. With the exception of the jig, they were representative of an unsophisticated field repair, yet provided controlled test specimens upon which reliable modal analyses could be performed.

#### IV. Experimental Analysis

This chapter describes the equipment and the holographic technique used in the experimental phase of this thesis. It also describes how holography is used to determine the natural frequencies and mode shapes of the test panels.

##### Equipment

Test Fixture. As mentioned in Chapter II, interferometric holography is very sensitive to motion, capable of detecting displacements in the microinch range. Therefore, a special fixture was required to isolate the panel from its surroundings without contributing to or interfering with the motion of the panel itself. Any rigid body motion, vibration, or thermal expansion or contraction of the fixture would be superimposed onto the motion of the panel, making it difficult to isolate the true dynamic behavior of the panel itself.

This experiment used the test fixture designed and first used by Walley. Cyr subsequently used this fixture with success. Thus, it provided a proven method of mounting and isolating the test panels for holographic analysis [41;7]. the fixture is made of solid steel and can be securely fastened to the holography table. It is massive and stiff enough to eliminate holographically perceptible rigid body motion, and it has a sufficiently low coefficient of thermal

expansion to remain thermally stable at normal room temperatures. It provides fully clamped boundary conditions on all four edges of the panel. Figures 4.1 through 4.3 show the geometry and the components of the fixture.

The base and cap of the fixture each have a 1 1/4-inch wide by 2 1/8-inch deep curved channel into which the top and bottom edges of the panel are clamped. Channel curvature is very close to that of the panel so that only a slight amount of stress is put on the panel when it is tightened in place. In the bottom channel, a series of recessed allen screws tightens nine steel chucks against a thin aluminum bushing to provide a uniform distribution of clamping pressure across the bottom inner edge of the panel. This securely clamps the front surface of the panel against the front edge of the curved channel. Like the channel, the curvature of the bushing and the chucks is close to that of the panel to provide even clamping. A similar arrangement clamps the top of the panel into the fixture cap.

The 1 1/2-inch wide by 2 1/8-inch vertical channels on each side of the fixture hold the vertical edges of the panel. Each channel has two vertical steel bars, or flats. The outer flat supports the front of the panel and the inner flat distributes the clamping pressure from behind. A series of allen screws tightens the inner vertical flat to create a uniform distribution of clamping pressure.

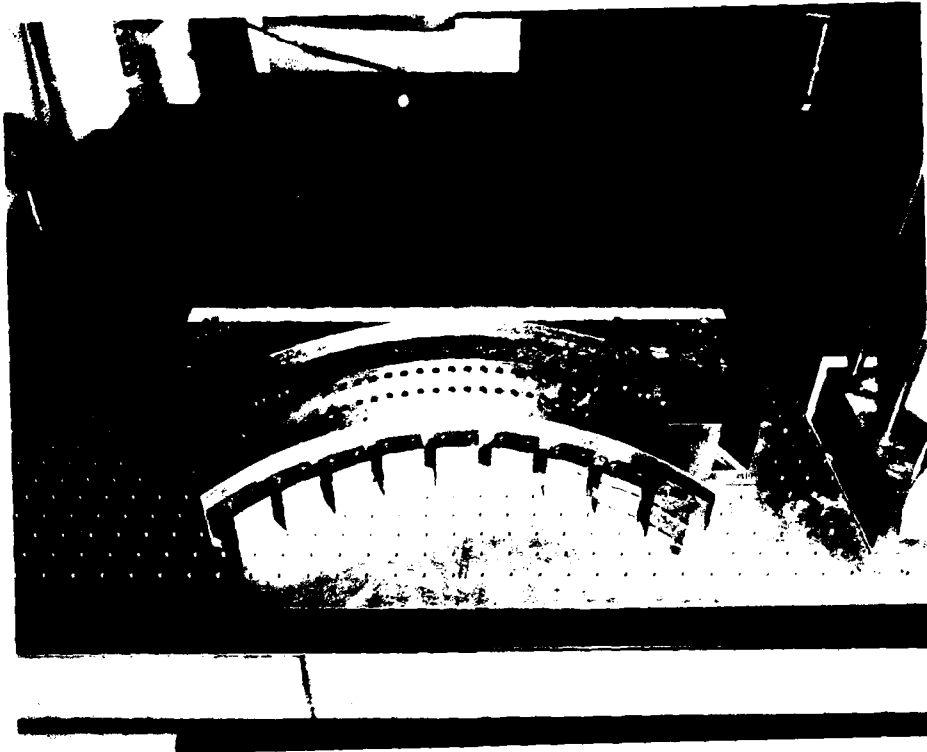


Figure 4.1 Test Fixture Curved Channel (Cap)

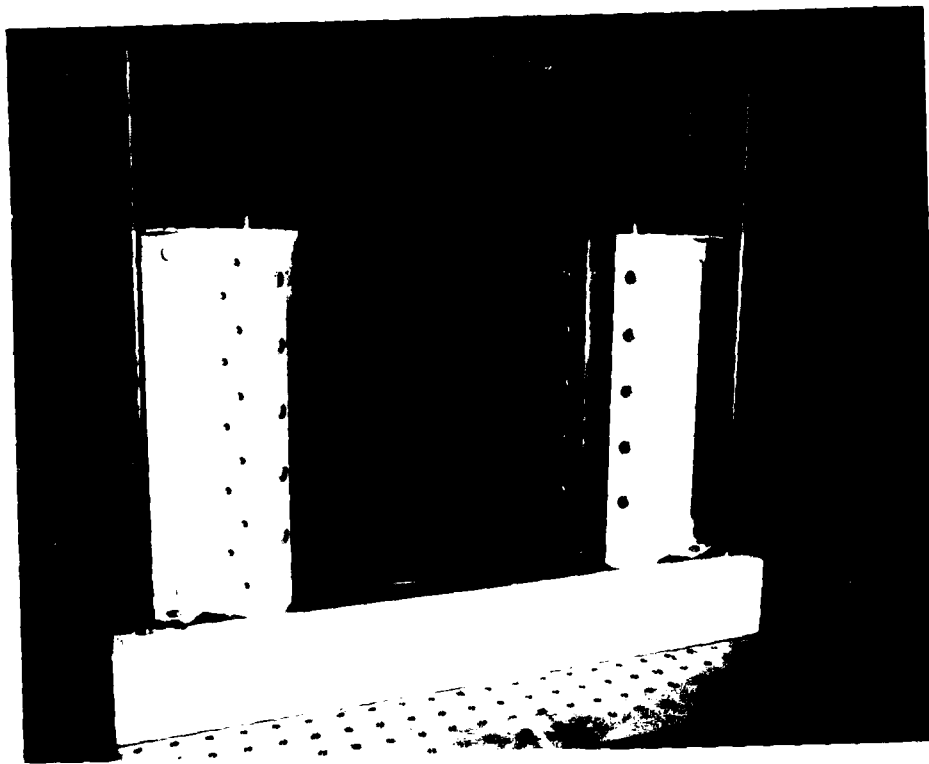


Figure 4.2. Test Fixture (Front)

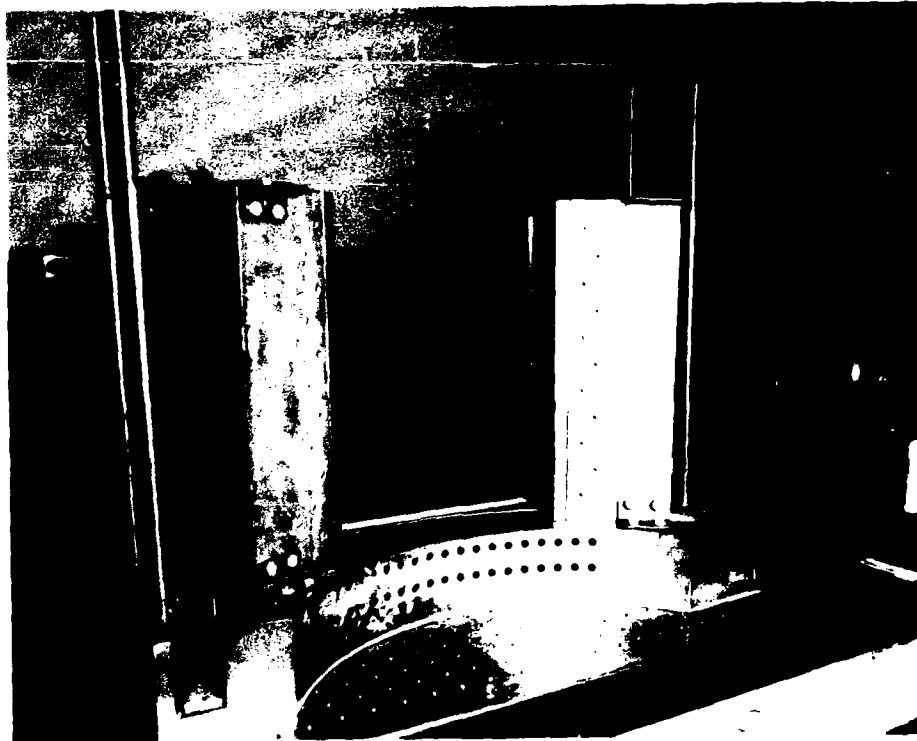


Figure 4.3. Test Fixture (Back)

A specific tightening sequence was developed to provide consistent and smooth clamping of the panel. Three methods were tried, with the first two resulting in fringe patterns that were biased toward one boundary or another, indicating uneven clamping or pre-buckling of the panel. The third and most successful method was to place and tighten the cap onto the fixture columns after placing, but not clamping, the panel into the fixture. This ensured that the weight of the cap was carried by the fixture itself, and not by the panel. Next, the screws along the left column were tightened from bottom to top. This created a firm and straight boundary on

one edge. The top and bottom circumferential rows of screws were then tightened in sequence from left to right around the curve. Alternating from bottom to top, this sequence served to smooth the panel along the curve and eliminate kinks or uneven local radii. Finally, the screws in the right column were tightened from bottom to top to complete the fully clamped boundary condition.

Walley and Cyr emphasized consistently torquing the allen screws to the same value. Walley used 72in-lbs while Cyr used 36in-lbs [42;7]. Since each reported good results, 36in-lbs was used in this thesis. This provided a consistent clamping pressure and reduced the danger of crushing the panel at the edges.

Use of this mounting technique ensured a reasonably consistent boundary condition for each panel. The resulting holograms provide evidence of this by the absence of fringe lines emanating from the edge of the panels, indicating that the panels do not move at the edges.

Holographic Recording Device. Newport Corporation's HC-300 Holographic Recording Device was used to make the holograms. This thermoplastic recording device was cleaner and easier than the traditional wet chemical process. The only drawback was the small size of the recording plates themselves, which made it more difficult to photograph the image.

Recording an image on the thermoplastic plate is a four-step process. The plate has a layer of thermoplastic recording material and a photoconductor. In the first step, a uniform charge is deposited on the plate. A positive charge forms on one side and a negative charge on the other (Figure 4.4a). The plate is then exposed to the complex wave front of the overlapping object and reference beams as described in Chapter II. A negative charge passes through the photoconductor in the light areas but remains on the other side in the dark areas (Figure 4.4b). The plate is charged once again; however, since the exposure has ended, the charge does not move across the photoconductor as in the first step. As a result, a greater charge density resides in the illuminated areas (Figure 4.4c). Finally, the plate is developed by heating the thermoplastic. In the illuminated areas, where the electric field is stronger, electrostatic force squeezes the heat-softened thermoplastic into thinner layers. In the darker areas, the thermoplastic tends to bulge out (Figure 4.4d). The result is a surface-relief hologram that diffracts light like a conventional hologram when it is reconstructed with a reference beam. The hologram can be erased by controlled heating (Figure 4.4e) [26].

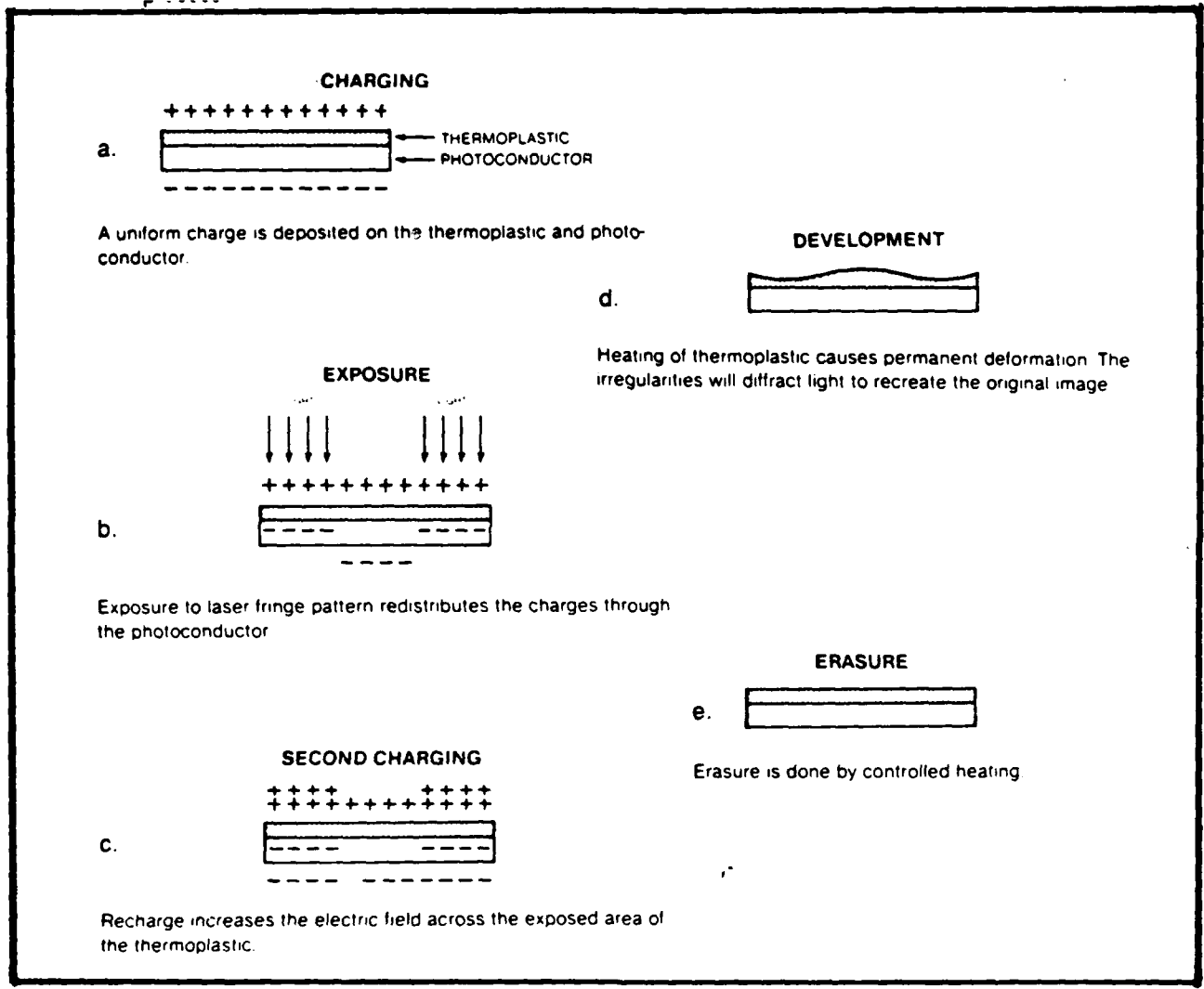


Figure 4.4. Thermoplastic Hologram Process

Equipment. In addition to the test fixture and the HC-300 System, the experiments were performed with a conventional holographic setup using off-the-shelf equipment. Appendix B is a list of the equipment used. Figure 4.5 shows the instrumentation and Figures 4.6 through 4.8 show the equipment setup.

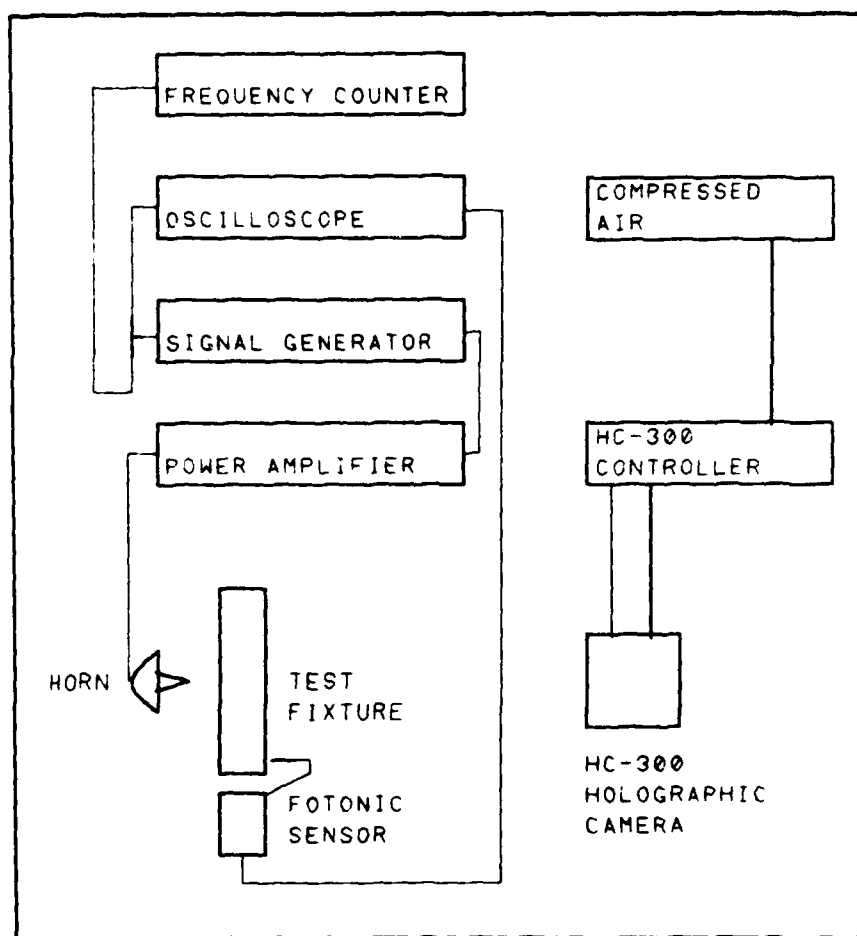


Figure 4.5. Instrumentation Diagram

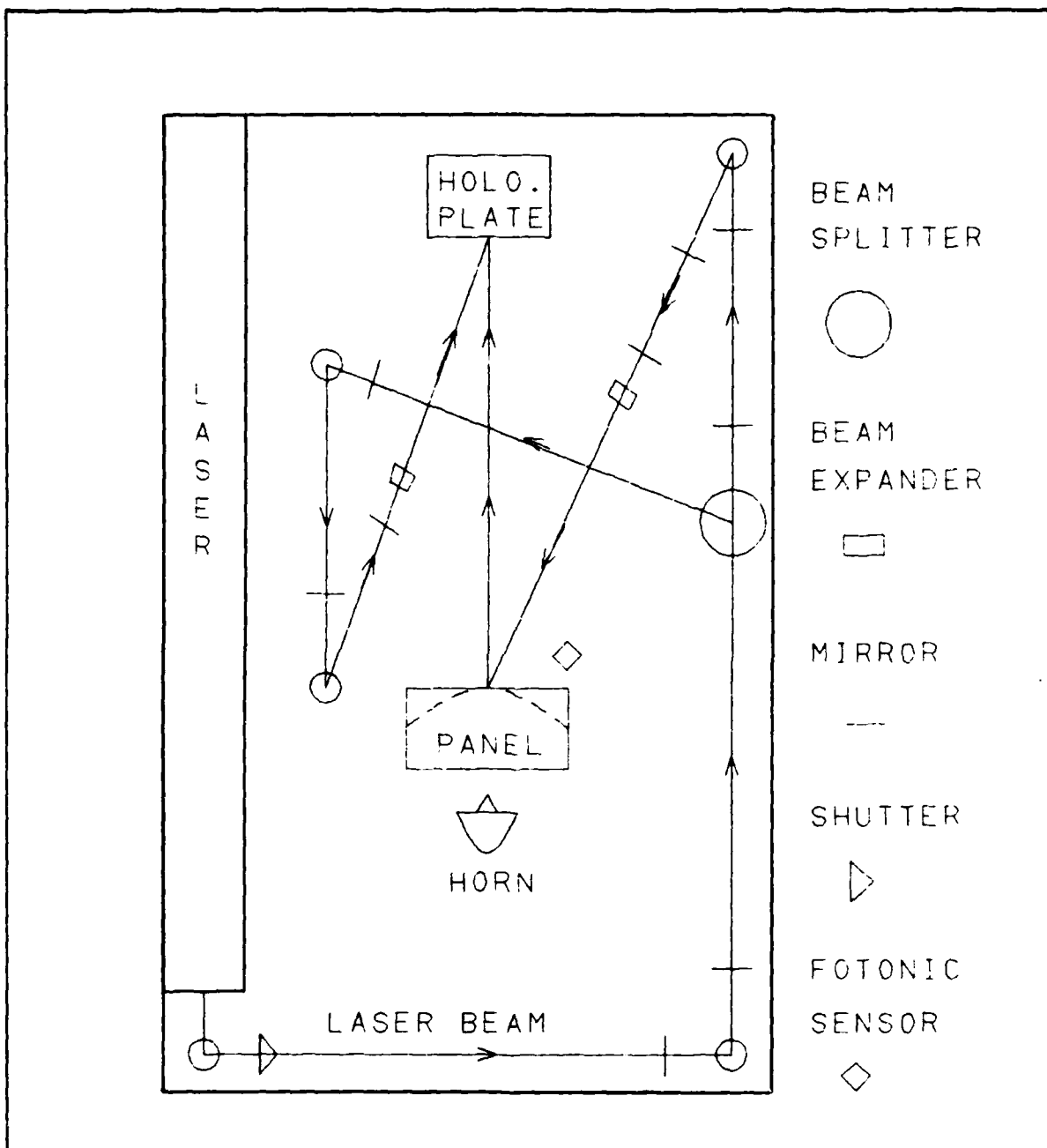


Figure 4.6. Equipment Setup (Schematic)



Figure 4.7. Equipment Setup (Front)

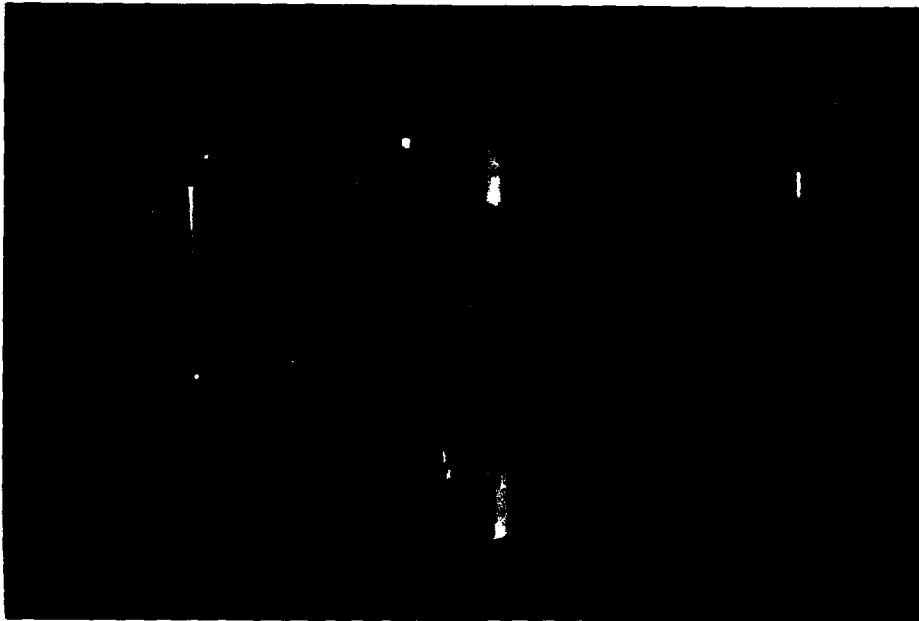


Figure 4.8. Equipment Setup (Back)

The floating table is essential as it provides a level and stable experimental surface that is isolated from external vibrations in the lab. Without the table, random external vibrations would emanate through the fixture and panel, contaminating the results.

The HeNe laser provides the coherent, monochromatic light previously discussed in Chapter II. A variable speed shutter allows specific exposure times to be programmed when shooting the holograms. An array of mirrors directs the light beam both before and after it is split. The variable beam splitter splits the beam into the reference and object beams. It is adjustable to vary the intensity ratio of the two beams to image quality. The combination spatial filter and beam expander clean up the light beams and expand them onto the object and the plate. Adjustable irises are placed along the beam path to reduce backscatter of the light.

A photonic sensor was used to ensure that true natural, or resonant, modes were being identified. The sensor was placed within 1/8-inch of the front side of the panel. A 1/8-inch square piece of aluminum foil was attached to the panel with double-sided tape as a reflecting surface for the light that this instrument uses to sense minute displacements. As the panel vibrates, the photonic sensor transforms the changing light intensity to signals that are input to an oscilloscope as sinusoidal waveforms. A signal

generator and amplifier simultaneously drive a speaker horn with an exponential cone. This horn emits pinpoint noise that excites the panel, causing it to vibrate. The signal driving the horn is also input to the oscilloscope on the other axis, so that perpendicular waveforms are displayed. The Lissajous figures formed by these two waves on the oscilloscope indicate the presence of a true resonant condition, as opposed to a harmonic integral. This will be explained in the following section.

Other equipment included a light meter to monitor the intensity of the reference and object beams at the thermoplastic plate, a light meter to monitor laser output, and miscellaneous tools and equipment for moving and cleaning the fixtures and optical instruments. A video camera and recording system was used to record the experiments and as a convenient way to observe, via the monitor, the images being created on the tiny thermoplastic plate.

#### Holography Procedure

This section describes the procedure for using holography to locate and record natural frequencies and mode shapes. A step-by-step process for making holograms with the HC-300 is included in Appendix B. After the equipment had been set up, the panel mounted, and the light beam intensities checked, a hologram of the panel at rest was

made. Leaving this hologram in the camera mount and the light beams on, a virtual image of the panel could be observed superimposed over the actual object. This static image was the basis for the real-time holograms that were used in the search for the natural frequencies and mode shapes.

With the video camera focused on the image through the plate and the horn mounted behind the panel, a sweep was made by gradually increasing frequency of the excitation noise as the dynamic response of the panel was observed via the video monitor. For this first sweep, the amplitude was constant and relatively weak, so that when resonance was reached, the fringe pattern was not a blur. The frequency range of interest was from 75 Hz (the lowest attainable with the equipment) to 1000 Hz, so that at least the first six modes were observed. This first sweep was to identify approximate resonant frequencies and mode shapes.

If the hologram became distorted with hazy fringe patterns that floated across the image, especially when the panel was at rest, then a new static hologram had to be made. This occurred every five to ten minutes, depending on thermal activity in the lab. These hazy patterns made it difficult to clearly observe and identify true mode shapes.

After the first sweep, a new static hologram was made and the frequency sweep was repeated. This second sweep was

more deliberate and the noise amplitude was increased until more distinctive patterns appeared at resonance. The oscilloscope, as well as the video monitor, was observed this time. When a distinctive fringe pattern began to appear on the monitor, a distinctive Lissajous figure would begin to form on the oscilloscope. An elliptical or circular Lissajous figure indicated that the panel was vibrating at a true natural frequency. Any other shape, such as a "figure eight," indicated that it was vibrating at an integral multiple (harmonic) of a natural frequency [22]. The latter phenomenon was most noticeable below the first, or fundamental, mode. It is discussed in detail in Chapter VI.

Having identified the approximate frequency within 5 Hz for each resonant mode, the next step was to pinpoint the exact natural frequencies and their mode shapes. After another clean hologram was made, another sweep was made; this time concentrating on the approximate frequencies at which resonance occurred.

If a mode was well defined, the frequency was varied above and below the point where the most fringes appeared for a constant amplitude of excitation. If the mode was not contaminated by a neighboring mode (usually symmetric and asymmetric modes were in pairs), the fringe order around the antinodes (points of maximum displacement) appeared to pulsate normal to the panel surface and not "slide" tangent to it.

If the pattern was not distinct, or if some of the nodal lines (lines of zero displacement) disappeared, then modal contamination was probably occurring. For a lightly damped structure like the panel, this would happen when the frequencies of adjacent modes were within one to two percent of one another. This contamination was reduced by strategically locating the horn to take advantage of the characteristics of the adjacent modes. By pinpointing the horn on a strong antinode of the desired mode, or on a nodal line of an unwanted mode, the panel response would favor the desired mode. In general, the natural frequency of a mode would shift toward an adjacent mode when contaminated, so that a contaminated lower mode would actually be too high and a contaminated higher mode would actually be too low [19].

When an uncontaminated resonant mode was isolated, a time average hologram was then made. Each of the first five modes for each panel was located and recorded in this way. Photographs were then taken of each hologram to provide a permanent record for further study.

## V. Finite Element Analysis

This chapter presents the technique used to develop the finite element models. The computational limitations imposed by the PC version of NISA restricted the mesh size and complexity of the models. As a result, the panels with the +45° and -45° cutouts and repairs were not modeled. The other panels, however, provided some useful data regarding the accuracy of this version of NISA in analyzing free vibration problems.

### Element Selection

NISA elements are identified by two variables: the element type (NKTP) and the element order (NORDR). The majority of the elements are isoparametric because identical shape functions are used to interpolate element geometry and element displacement variations [11:4.3]. The elements are quadrilateral or triangular. In addition to the corner nodes, the elements can have one or two nodes on each side. The midside nodes are useful in defining curved shapes, providing transition elements between coarse and fine regions, and increasing the number of degrees of freedom in the model without increasing the number of elements.

The 3D Laminated Composite Shell element, NKTP 32, was used to construct the finite element model of the composite panels. NISA offers two other shell elements: the 3D

General Shell element, NKTP 20, and the 3D Thin Shell element, NKTP 40. These latter two elements can be used for isotropic and orthotropic materials, but are unsuitable for anisotropic laminated composite structures. The 3D Thin Shell element is based on the Kirchoff-Love thin shell hypothesis; therefore, it neglects transverse shear effects. The 3D General Shell, like the 3D Laminated Composite Shell, includes transverse shear effects in its formulation [11:4.48,4.66]. Each element was used in the test cases described in Appendix D to determine the effect that including transverse shear deformation has on the analysis of thin plates and shells with NISA.

The NKTP 32 with one midside node per edge was used to model the composite panels that were experimentally analyzed. The parabolic shape of this eight-noded element provided a better geometric representation of the circumferential curve of the actual panel than could be achieved with faceted flat plate elements (Figure 5.1). Each node can have up to six degrees of freedom. These are the displacements in the x-, y-, and z-directions, defined in NISA as UX, UY, and UZ; and the rotations about the x-, y-, and z-axes, defined in NISA as ROTX, ROTY, and ROTZ. They are defined in the global coordinate system (Figure 5.2). In the local coordinate system, these elements have no stiffness about the normal to the shell surface. NISA overcomes

the potential for ill-conditioning by incorporating a small rotational stiffness at those nodes where the shell curvature is continuous [11:4.47-4.48].

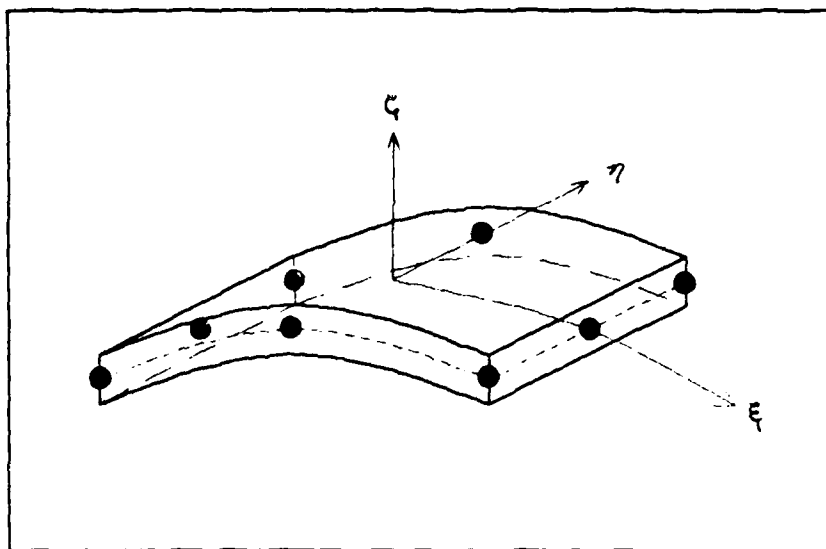


Figure 5.1. Parabolic Composite General Shell, Element NKTP 32

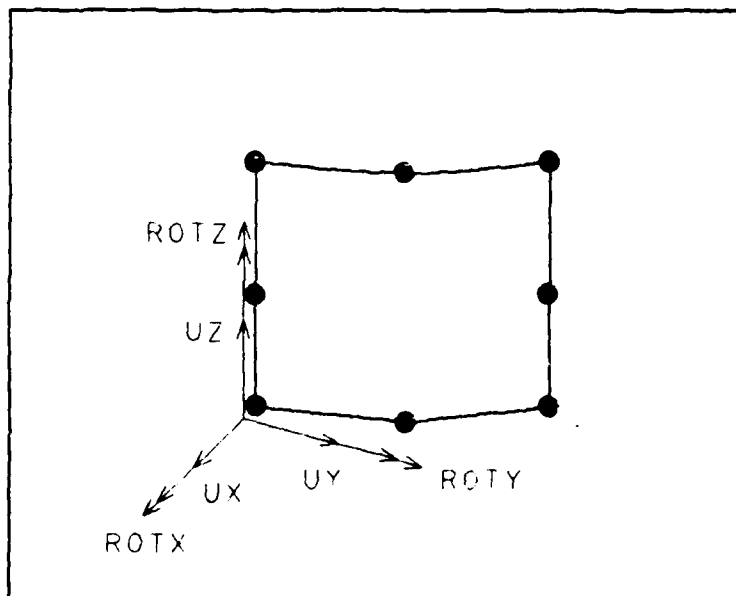


Figure 5.2. Nodal Degrees of Freedom, Element NKTP 32

The NKTP 32 element assumes N layers of perfectly bonded orthotropic materials. Element properties are described at the nodes. These properties include total shell thickness at a node based on individual lamina thicknesses, fiber orientation with respect to a global coordinate system, and the previously mentioned degrees of displacement and rotational freedom. Extensional-bending stiffness coupling, defined in Chapter II, is included, along with transverse shear effects. The quasi-isotropic properties of the balanced, symmetric panels in this study result in the elimination of extensional-bending stiffness coupling ( $B_{ij} = 0$ ) while the small thickness-to-radius-of-curvature ratio should minimize the transverse shear effects [16:160].

#### Panel Modeling

The solid, 0° cutout, 90° cutout, 0° repaired, and 90° repaired panels were modeled with the NKTP 32 elements. The more complex mesh required to model the +45° cutout, -45° cutout, +45° repaired, and -45° repaired panels was not investigated because of the memory limitations imposed by the PC. To overcome these limitations, mesh density was increased without increasing computer memory requirements by modeling only one half of the panel. This approach lost modes that were not symmetric about the horizontal midline at which the panel was cut. But, it increased the accuracy

of predictions for the lowest, most significant modes that were symmetric about the horizontal midline.

Before investigating half-panel models, several full-panel models were analyzed to obtain data on the accuracy of NISA solutions. The solid panel was used for this since it was the simplest to model. The models varied from having 36 eight-noded elements to 256 four-noded elements. The results supported the NISA Manual recommendation that the eight-noded quadrilateral element would be the most efficient element [11:4.48].

A convergence study was also done to determine the optimum mesh size using the NKTP 32 element with eight nodes. The results are presented in Table 5.1. They are inconclusive because the model failed to converge before the 10 x 10, eight-noded element model overran the hard disc memory.

Table 5.1. Convergence Study for Eight-Noded Element

<u>Grid</u>	<u>First Mode (Hz)</u>	<u>CPU Time (Sec)</u>
6 x 6	642	2938
8 x 8	586	4147
9 x 9	573	6345
10 x 10	Overran Hard Disc Memory	

The 9 x 9 mesh for the full panel gave a fundamental frequency that was 12% high. A half-panel was investigated

to determine whether more accurate predictions could be attained within the memory limitations of the PC. The panel was cut at the horizontal midline because the lowest modes were symmetric across this line, or axis of symmetry. Figure 5.3 depicts this model with 72 eight-noded elements, the finest mesh that could be run to completion on the computer.

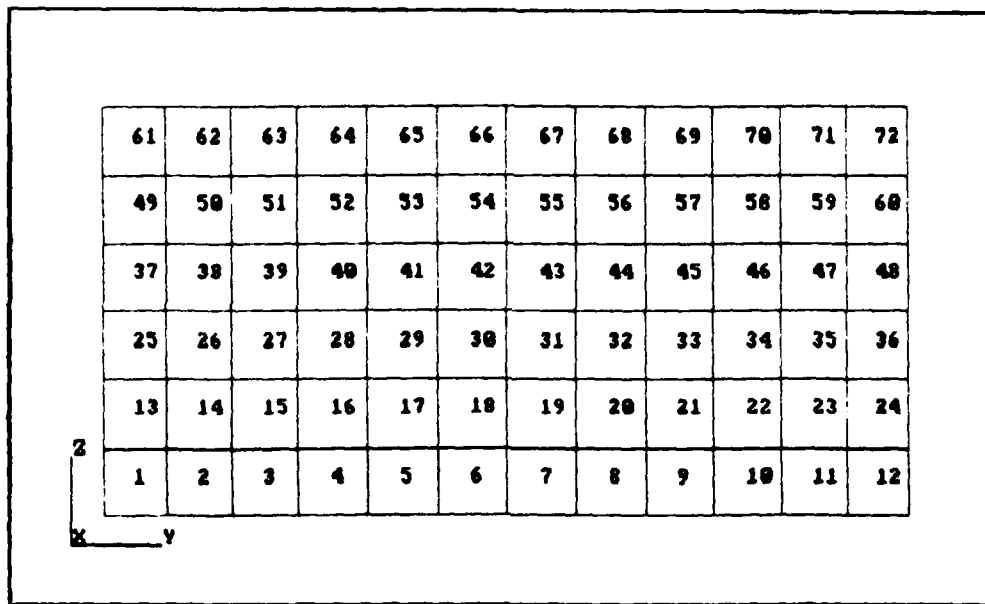


Figure 5.3. Half-Panel Model (NKTP 32, Eight-Noded Element)

The results for relatively coarse 6 x 3 half-panels were compared with the 6 x 6 full-panel results to ensure that the boundary condition at the axis of symmetry was adequately described, and that the half-panel accurately

reflected full-panel behavior for the lowest modes that were symmetric across the horizontal midline. The boundary condition across the horizontal midline restricted displacement in the meridian direction and rotation about the circumferential direction. The results of these two models were exactly the same for the first four modes, indicating that the half-panel model was sufficient to predict the modes of interest.

Having established the accuracy of using a half-panel model to obtain the lower modes, a 12 x 6, eight-noded element mesh was run. The results were 9%-16% high for the first four modes of the solid panel. Since these results were the closest achieved by NISA to the experimental results, this model was used as the basis for modeling both the 0° and 90° cutout panels, and the 0° and 90° repaired panels. A sample NISA input file is presented in Appendix C.

The cutout panels were modeled by simply omitting the elements at the cutout locations. The repairs were modeled by separately modeling the patches and the panels. These separate models were then connected by coupling the displacements at common nodes. A better model would have been obtained if there had been sufficient computer memory to run a finer mesh. A finer mesh would have permitted the modeling of all 32 rivets, and the adding of point masses to

simulate the mass contribution as well as rivet connectivity. The results obtained with each of these half-panel models are presented along with the experimental results in Chapter VI.

## VI. Results and Discussion

This chapter summarizes and discusses the experimental and analytical results. First, the results obtained for the unrepaired panels are compared to Cyr's results to establish a reliable baseline. Next, the results for each repaired panel are compared to the results for both the solid panel and the cutout panel before repair. The overall effect of the patching technique is analyzed, and finally, the accuracy of the NISA program is evaluated.

The results included the natural frequencies and mode shapes of each panel. Since no closed-form solutions exist for this problem, the comparisons are between experimental results and finite element approximations. Cyr's results are included for further comparison, especially since his STAGSC-1 results were very close to the experimental results. Analysis of the results concentrates on the changes in natural frequency and mode shape caused by cutouts and patches. First, the effects of the cutouts are noted to provide continuity with Cyr's work. Then, repair patch effects are discussed with emphasis on how much the repaired panel resembles the original solid panel. Instances where mode shapes change from asymmetric to symmetric are noted. Finally, observations are made about the NISA finite element results.

The test conditions and procedures were standardized from panel to panel, and followed Cyr's methods as closely as possible. The possibility that the panels had a different moisture content or had suffered even the slightest damage since Cyr used them would account for some differences from his experimental results. Another important source of experimental error would be the clamped behavior of the panels. Although a very exact clamping method was developed and used, the fixture provided only an approximation of a truly clamped boundary. The effects of thermal expansion or contraction of the panels was reduced by running a complete test cycle during a single four-hour period and then remounting the panel if the test had to be repeated or extended. The repairs themselves, thoroughly discussed in Chapter III, were another potentially significant source of error. They were very difficult to accurately model within the constraints of the PC version of NISA.

#### Unrepaired Panels

This section presents the results for the unpatched panels. Experimental and NISA results are presented. Results were compared to those of Cyr to establish a reliable baseline for ultimately analyzing the effects of the repairs.

Solid Panel. The natural frequencies for the solid panel are presented in Table 6.1, followed by the mode shapes in Figures 6.1 through 6.9. The experimentally obtained frequencies and mode shapes agreed well with Cyr's experimental results. The differences were attributed to the previously discussed clamping conditions and to possible changes in internal panel conditions while in storage for the past two years.

The first two modes were strong and straight, but the third and fourth modes curved inward toward the top. The panel was removed and remounted, since a poorly clamped boundary condition was immediately suspected. The distortion remained, indicating that the panel had irregularities within some, or all, of its laminae. The frequencies, however, were consistent with Cyr's [7].

The symmetric modes (2, 4, and 5) were strongest when the horn was centered behind the panel, so that it was being excited at its strongest antinode. The two asymmetric modes (1 and 3) were isolated when the horn was two inches to one side of center, so that the panel was excited on one of its two strongest antinodes. These, coincidentally, were located on node lines of the symmetric modes.

The NISA results compared unfavorably with the STAGSC-1 results reported by both Walley and Cyr [42;7]. While the mode shapes of the first four modes were in agreement

(Figures 6.6 through 6.9), the natural frequencies were 9%-16% higher than experimentally observed. Since NISA consistently predicted frequencies that were high for both this and the 0° and 90° cutout panels, possible sources of error are discussed in the final section of this chapter.

Table 6.1. Solid Panel Results  
Natural Frequency (Hz)

Source	Mode Number				
	1	2	3	4	5
Experiment	514	519	716	727	821
NISA	561	588	797	846	n/a
Differ <sup>a</sup> (%)	+9	+13	+11	+16	n/a
Experiment (Cyr)	516	527	716	731	840
Differ <sup>b</sup> (%)	0	-2	0	-1	-2

a -- % difference between experimental and NISA results

b -- % difference between this thesis experimental and Cyr's experimental results

[7]

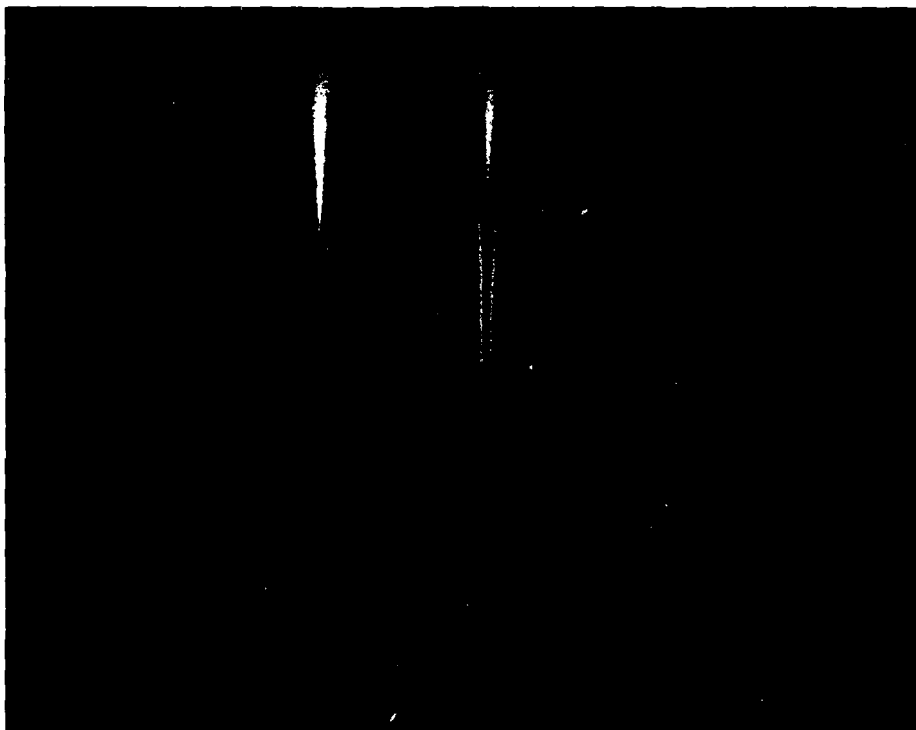


Figure 6.1. Solid Panel--Mode 1

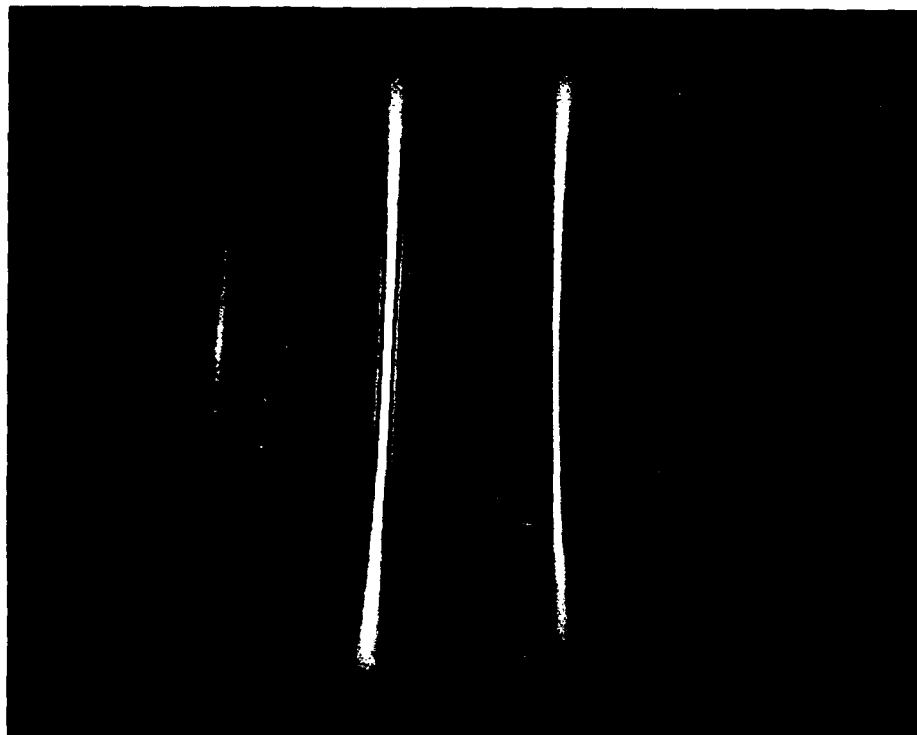


Figure 6.2. Solid Panel--Mode 2



Figure 6.3. Solid Panel--Mode 3

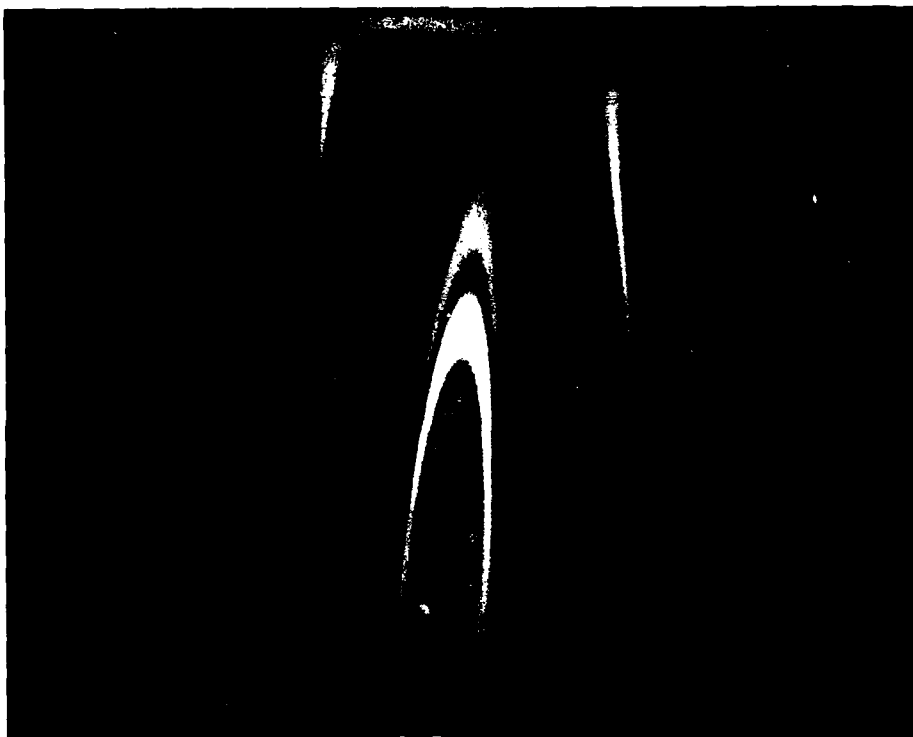


Figure 6.4. Solid Panel--Mode 4

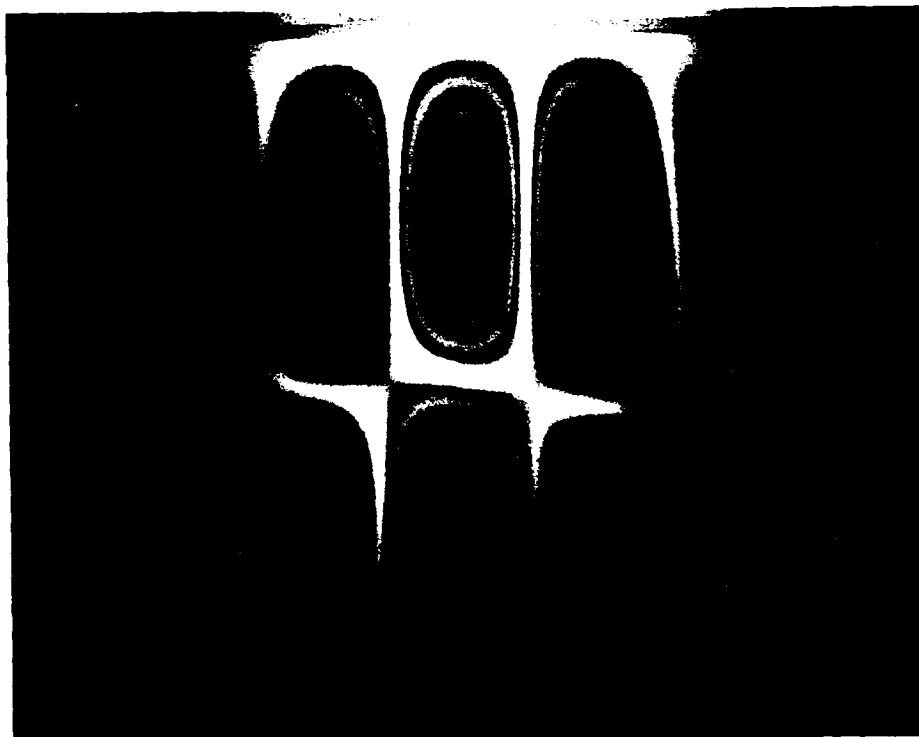


Figure 6.5. Solid Panel--Mode 5

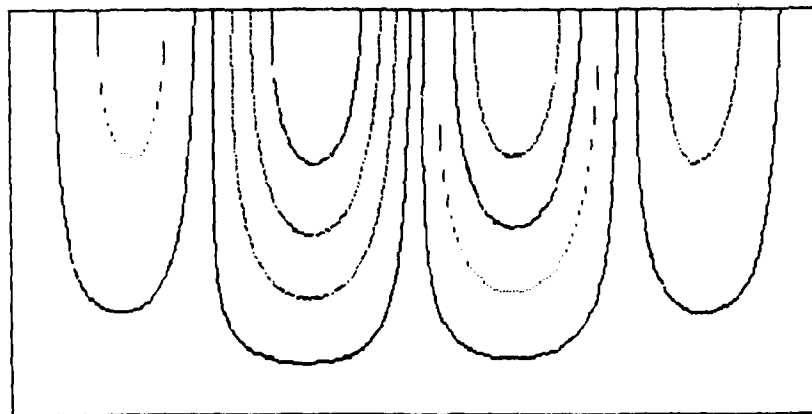


Figure 6.6. Solid Panel--Mode 1 (NISA)

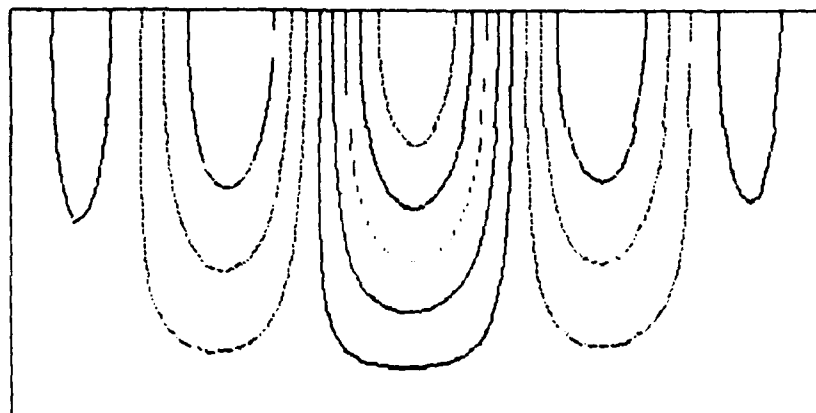


Figure 6.7. Solid Panel--Mode 2 (NISA)

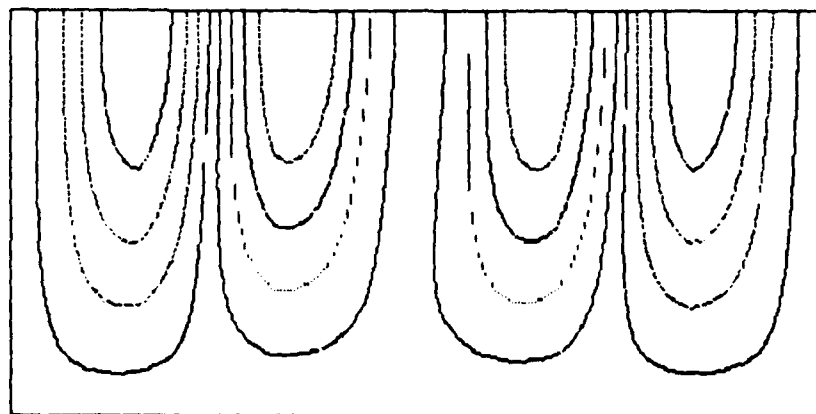


Figure 6.8. Solid Panel--Mode 3 (NISA)

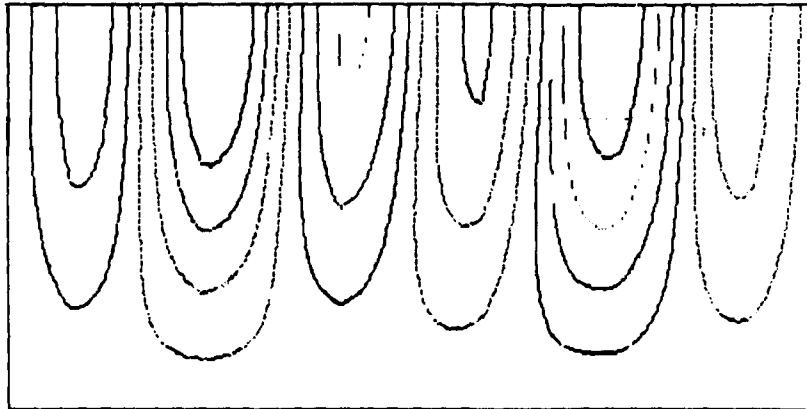


Figure 6.9. Solid Panel--Mode 4 (NISA)

0° Cutout Panel. The natural frequencies for the panel with the 0° cutout are presented in Table 6.2, followed by the mode shapes in Figures 6.10 through 6.18. The correlation with Cyr was good except for the fourth mode, where the natural frequencies differed by 8%. The mode shapes matched very well.

The first, second, third, and fifth modes were excited by one horn placed one inch below and one inch to the right of the cutout (as observed from the rear of the panel). The fourth mode was excited by one horn placed two inches to the right of the cutout.

This panel had the largest decrease in fundamental frequency from that of the solid panel. Recalling that natural frequencies are directly proportional to stiffness and inversely proportional to mass, this indicated that the effect of stiffness lost was greater than the effect of the mass lost. Each panel lost approximately the same amount of mass, since the cutouts were all two inches by four inches. The orientation of the cutout in this panel, however, resulted in the greatest number of circumferential fibers being severed. Since the dynamic behavior of the lower modes was more pronounced in the circumferential direction, it made sense that the loss of stiffness in this direction would have the greatest effect on overall panel behavior.

Second mode, a symmetric mode, had a relatively small frequency decrease. Fourth mode also had a small frequency drop, while third mode and fifth mode, like first mode, had large frequency drops. Again, the natural frequency trends and the mode shapes correlated very well with Cyr's results.

The phenomenon of mode switching, where a pair of symmetric and asymmetric modes interchange their frequency sequence, first appeared in the third and fourth modes. In the solid panel, third and fourth modes were asymmetric and symmetric, respectively. In this panel they switched, so that third mode was symmetric and fourth mode was asymmetric. This behavior was observed by Cyr and by Rajamani

and Prabhakaran [7;29]. It was observed in some higher-order modes of the other panels, and it occurred with the first and second modes of the 90° cutout panel. No predictable physical phenomenon was found that would account for this behavior, although it could be a function of inconsistent material properties or inadequate boundary conditions.

Table 6.2. 0° Cutout Panel Results  
Natural Frequency (Hz)

Source	Mode Number				
	1	2	3	4	5
Experiment	445	507	606	708	749
NISA	499	581	681	784	n/a
Differ <sup>a</sup> (%)	+12	+15	+12	+11	n/a
Experiment (Cyr)	440	485	577	655	766
Differ <sup>b</sup> (%)	+1	+5	+5	+8	-2

a -- % difference between experimental and NISA results

b -- % difference between this thesis experimental and Cyr's experimental results

[7]

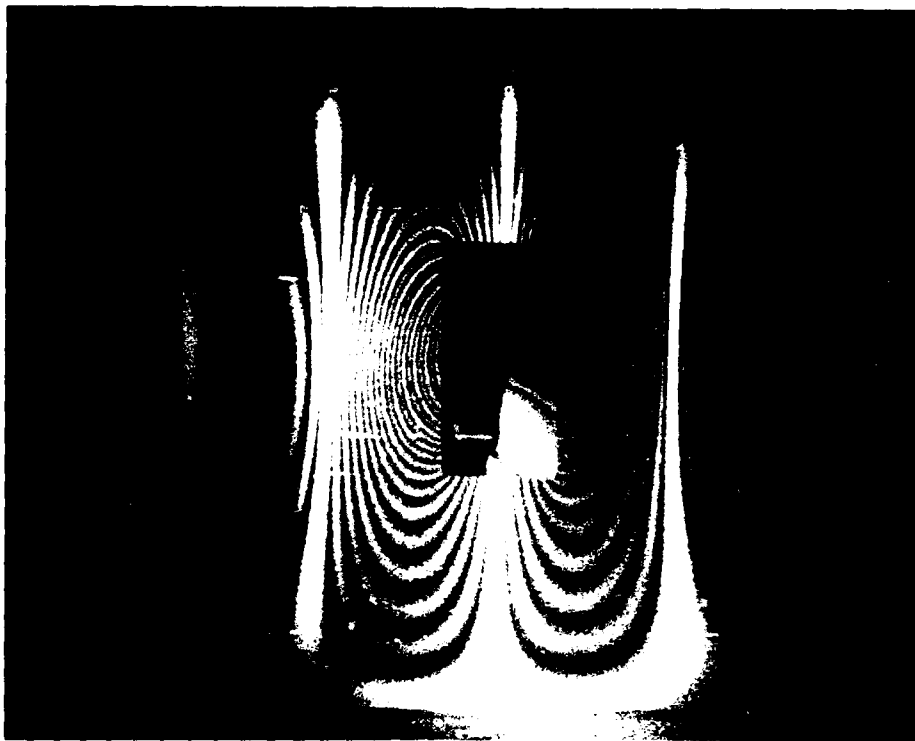


Figure 6.10. 0° Cutout Panel--Mode 1

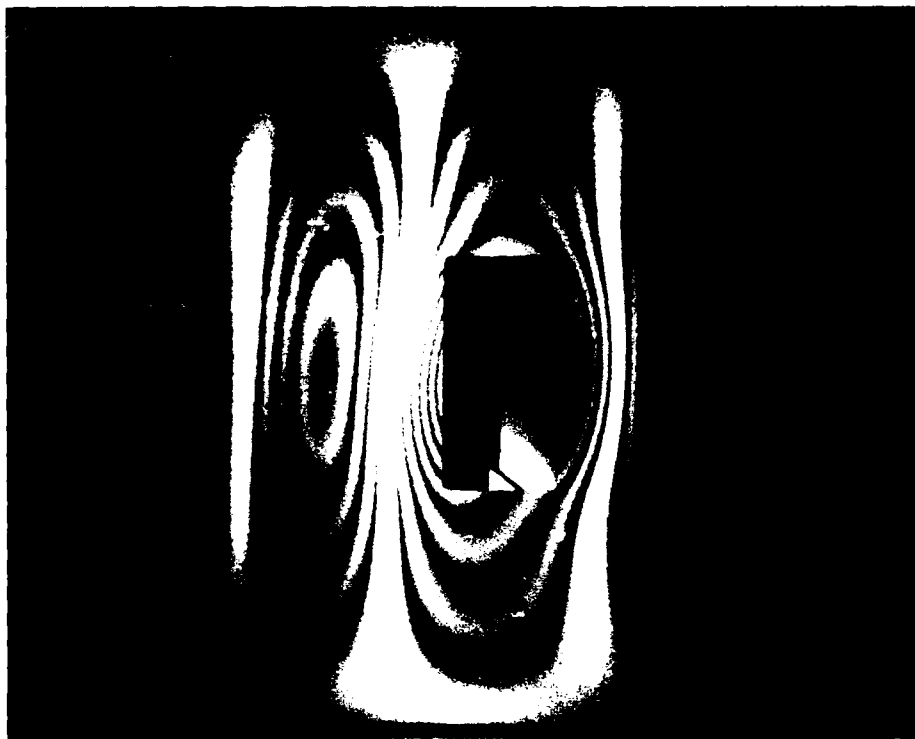


Figure 6.11. 0° Cutout Panel--Mode 2



Figure 6.12. 0° Cutout Panel--Mode 3

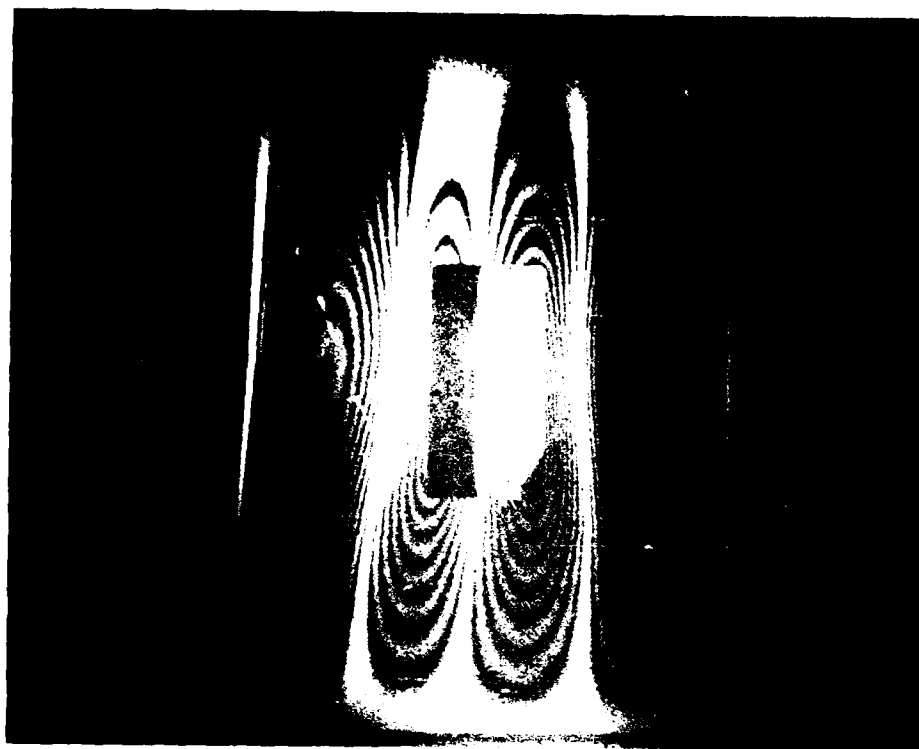


Figure 6.13. 0° Cutout Panel--Mode 4

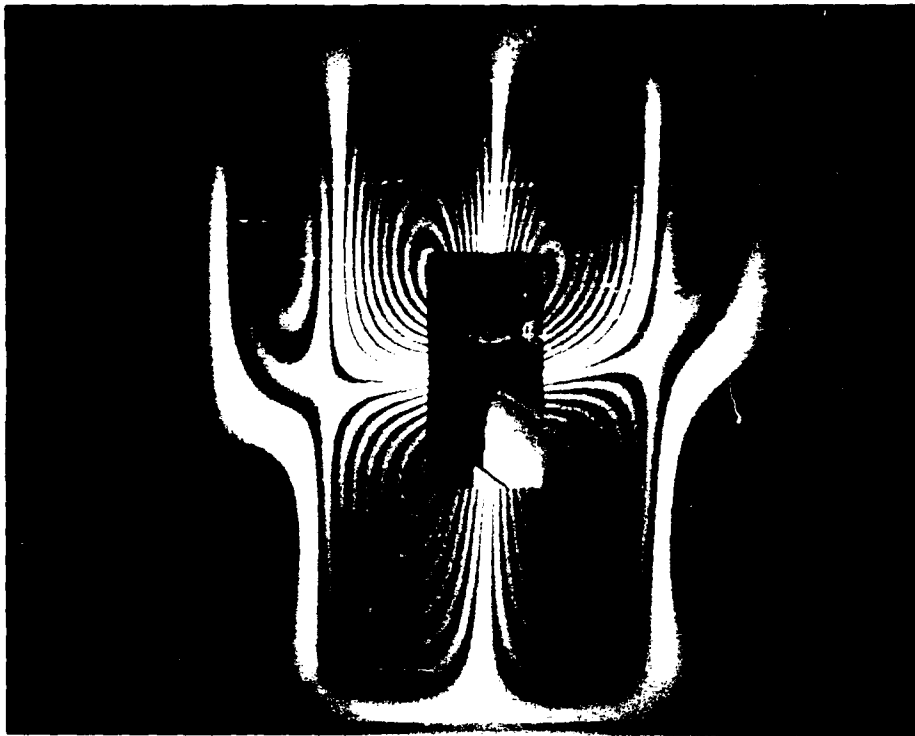


Figure 6.14. 0° Cutout Panel--Mode 5

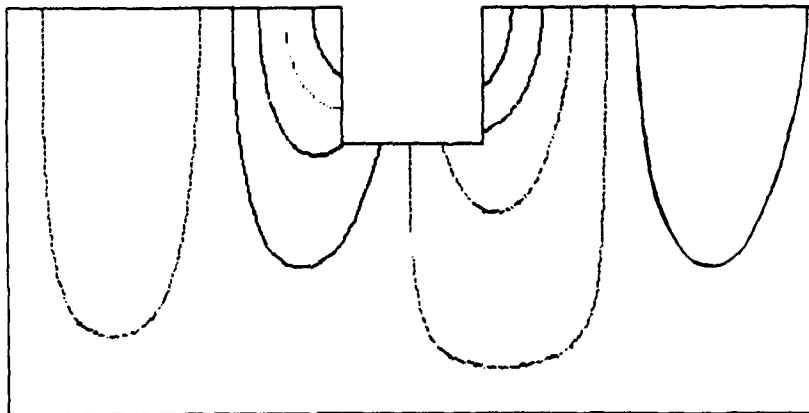


Figure 6.15. 0° Cut Panel--Mode 1 (NISA)

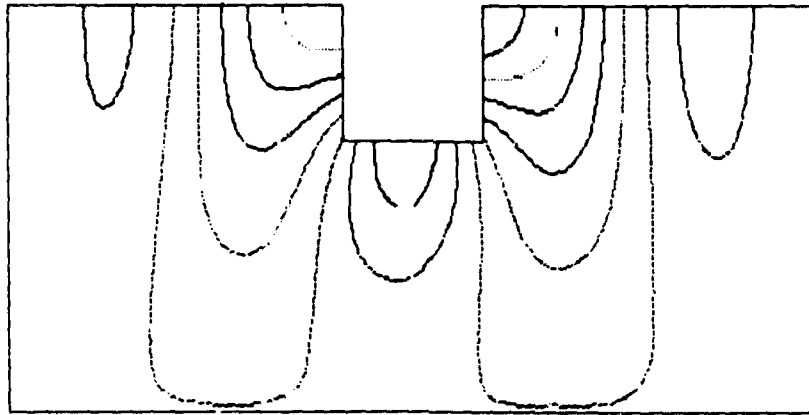


Figure 6.16. 0° Cutout Panel--Mode 2 (NISA)

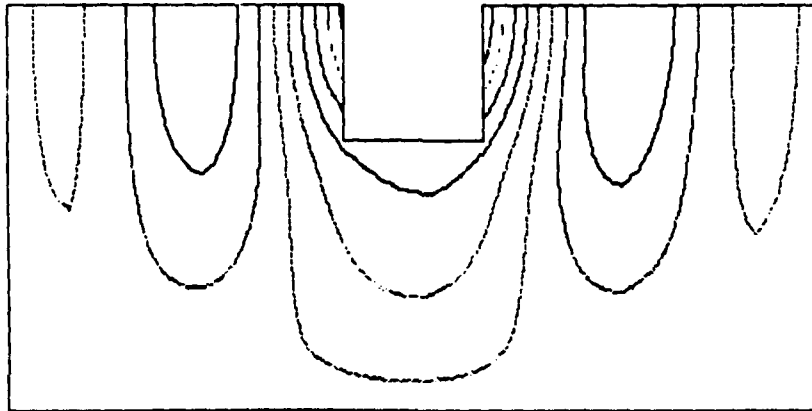


Figure 6.17. 0° Cutout Panel--Mode 3 (NISA)

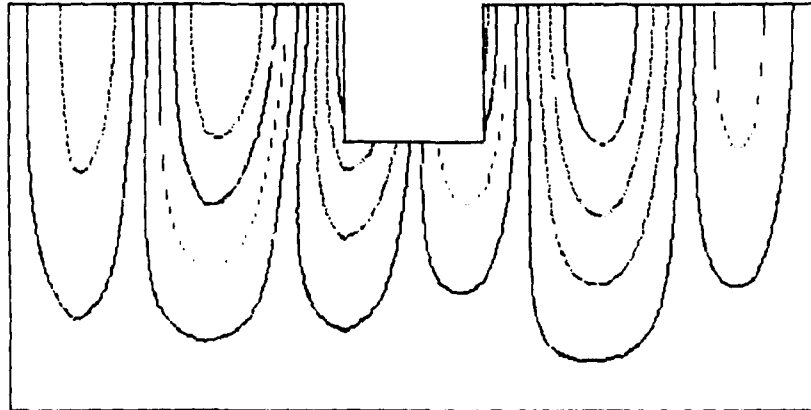


Figure 6.18. 0° Cutout Panel--Mode 4 (NISA)

90° Cutout Panel. The natural frequencies for the panel with the 90° cutout are presented in Table 6.3, followed by the mode shapes in Figures 6.19 through 6.27. The frequency correlation with Cyr was not very good, except for the fourth and fifth modes. Again, though, the mode shapes matched very well.

The symmetric first and third modes were excited by one horn placed two inches below the center of the cutout to take advantage of symmetry. Second mode was excited with one horn placed in the upper left corner of the panel where one of the stronger antinodes was located. Fourth mode was

excited by one horn in the lower right corner, and fifth mode was excited by one horn two inches above the right edge of the cutout.

This panel had a small increase in fundamental frequency from that of the solid panel. One factor leading to this result would be that the mass loss due to the cutout had a slightly greater effect on increasing the frequency than the stiffness had on decreasing it. Since the orientation of this cutout resulted in the fewest number of fibers being severed, this would make sense, just as it made sense for the 0° cutout to soften the overall panel.

As Cyr discovered, mode switching in the first pair of modes occurred in this panel. First mode in the solid panel was an asymmetric mode, whereas in this panel, first mode was symmetric. The second mode in this panel had switched to an asymmetric mode. The sequence in which symmetric and asymmetric modes appeared in the higher modes also changed as compared to the solid panel.

Table 6.3. 90° Cutout Panel Results  
Natural Frequency (Hz)

Source	Mode Number				
	1	2	3	4	5
Experiment	519	546	656	712	733
NISA	584	585	795	810	n/a
Differ <sup>a</sup> (%)	+13	+7	+12	+14	n/a
Experiment (Cyr)	496	527	608	705	731
Differ <sup>b</sup> (%)	+5	+4	+8	+1	0

a -- % difference between experimental and NISA results

b -- % difference between this thesis experimental and Cyr's experimental results

[7]

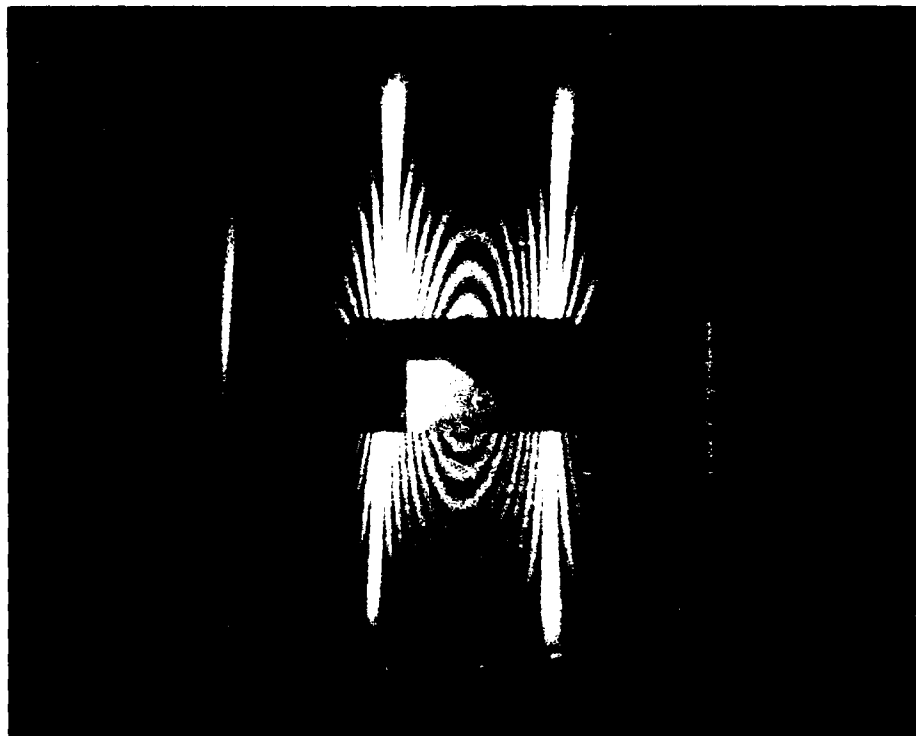


Figure 6.19. 90° Cutout Panel--Mode 1

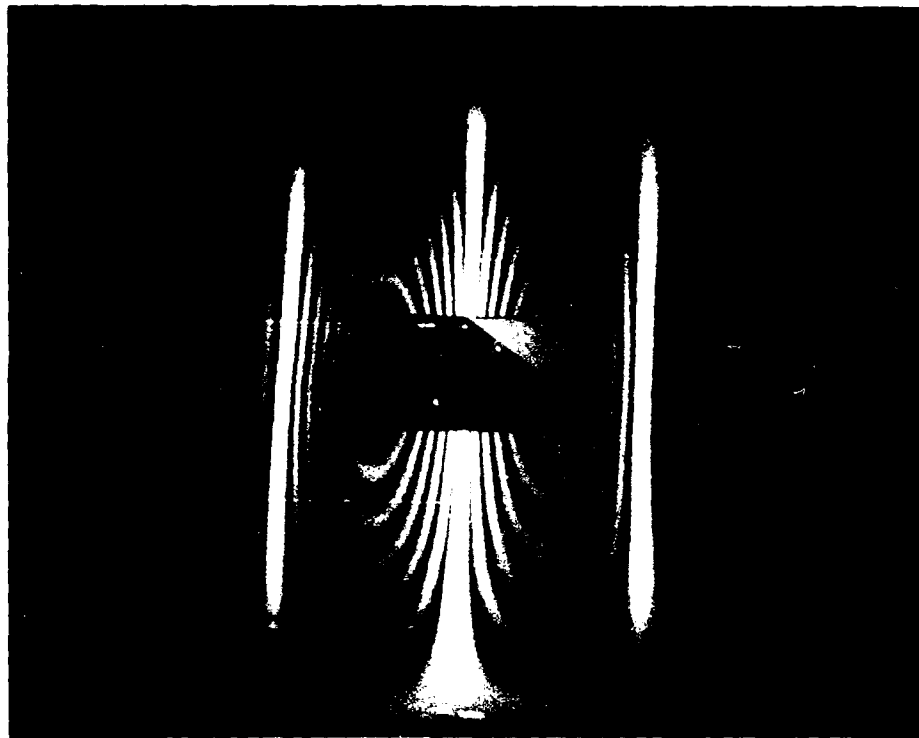


Figure 6.20. 90° Cutout Panel--Mode 2

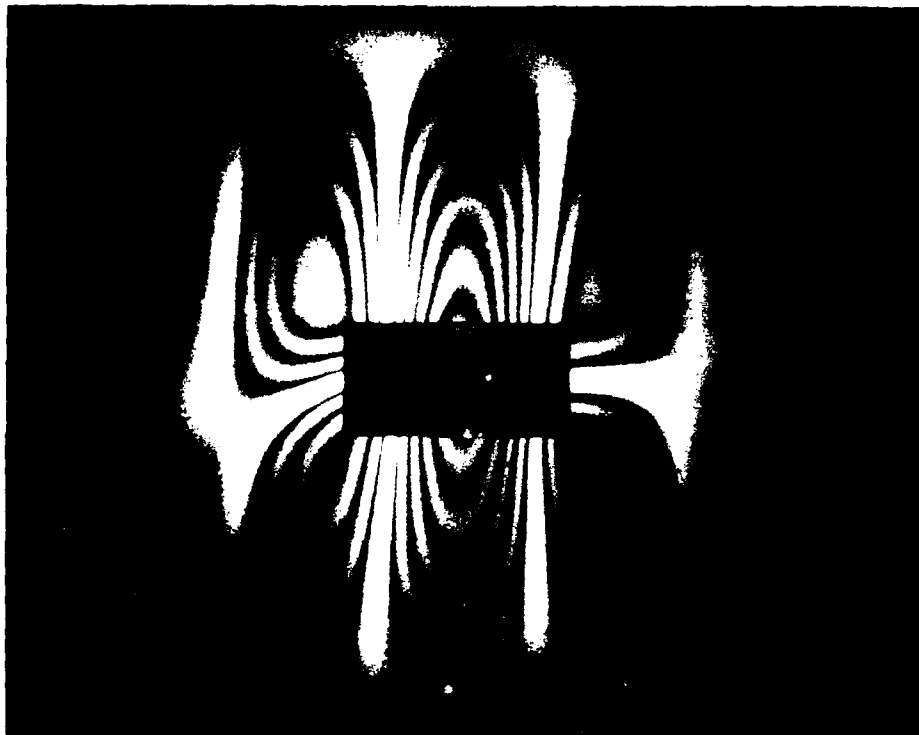


Figure 6.21. 90° Cutout Panel--Mode 3

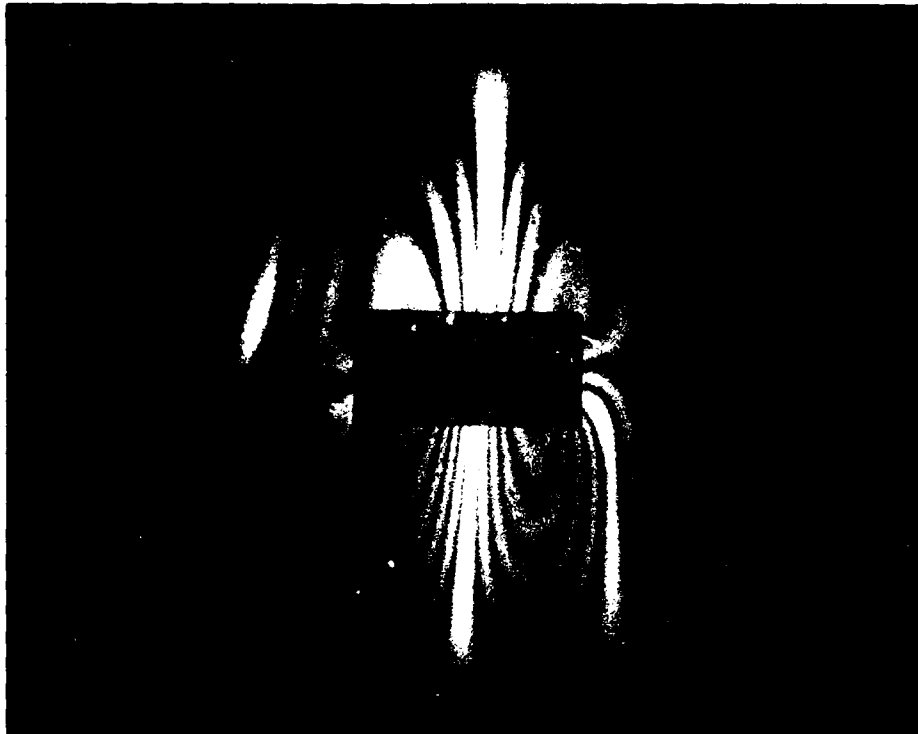


Figure 6.22. 90° Cutout Panel--Mode 4

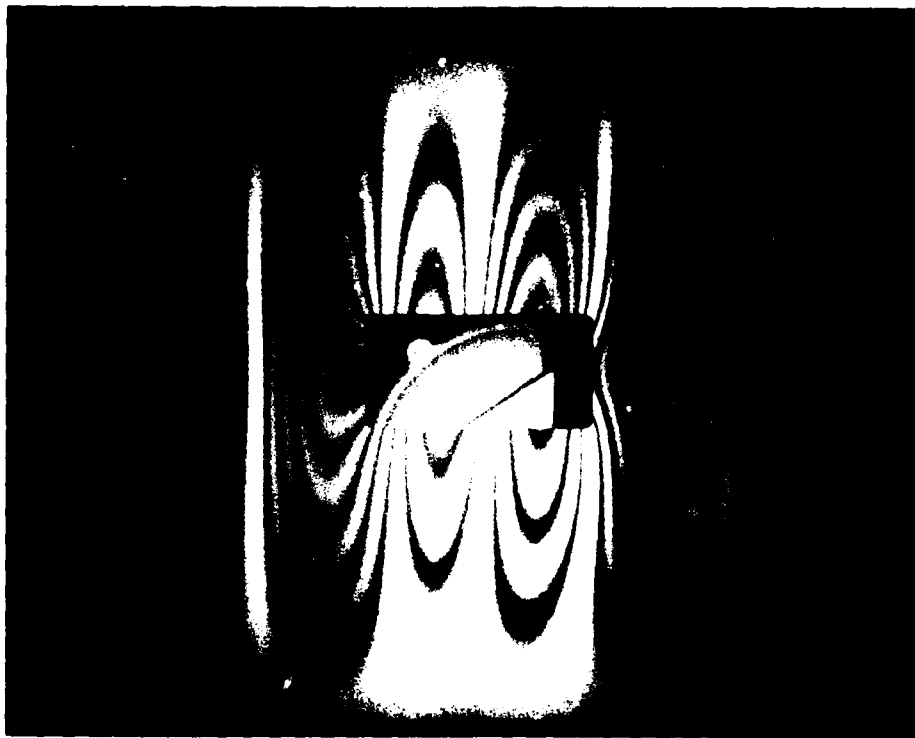


Figure 6.23. 90° Cutout Panel--Mode 5

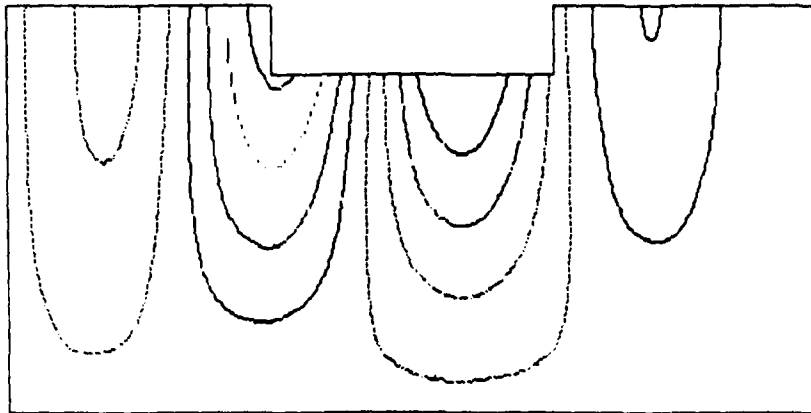


Figure 6.24. 90° Cutout Panel--Mode 1 (NISA)

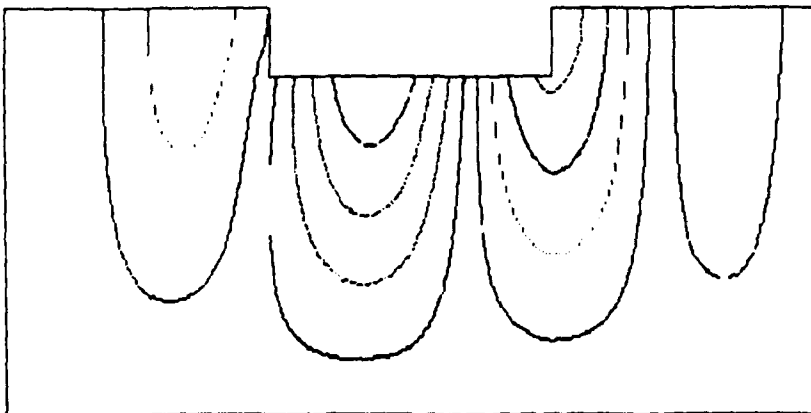


Figure 6.25. 90° Cutout Panel--Mode 2 (NISA)

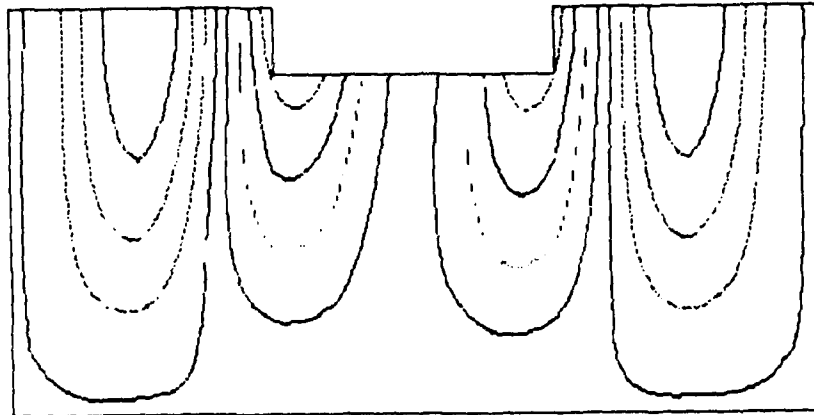


Figure 6.26. 90° Cutout Panel--Mode 3 (NISA)

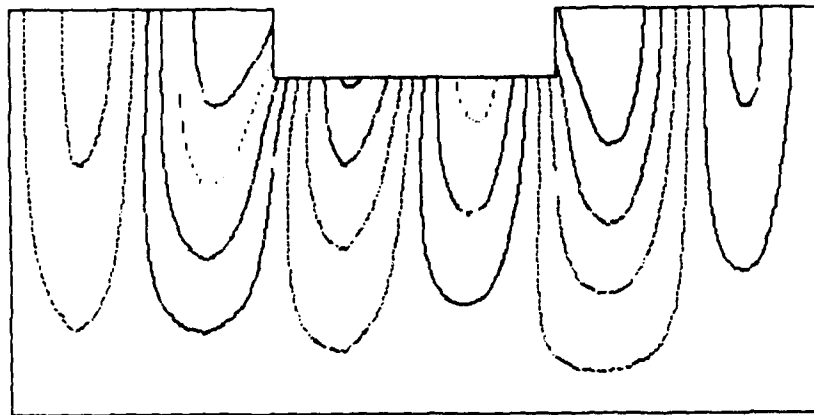


Figure 6.27. 90° Cutout Panel--Mode 4 (NISA)

+45° Cutout Panel. The natural frequencies for the panel with +45° cutouts are presented in Table 6.4, followed by the mode shapes in Figures 6.28 through 6.32. NISA predictions were not made for the +45° or the -45° cutout panels because of the limitations of the PC version. The experimental results were consistent with Cyr's results, the largest difference being at mode three, where this test produced a 5% lower frequency than Cyr's. The mode shapes correlated very well for the first two modes; at the next three modes the more complex shapes did not correlate as well. At these higher modes, the panel was more prone to contamination between adjacent modes. There was more sensitivity to the position of the horn, a behavior that Cyr observed also.

First and fourth modes were excited with the horn one inch below the extreme right corner of the cutout as viewed from the rear. The second mode was isolated with the horn centered two inches above the cutout. The third and fifth modes were most clearly defined when the single horn was placed one inch above the top right corner and one inch below the bottom left corner of the cutout, respectively.

Except for the second mode, the natural frequencies decreased, indicating an overall softening of the panel from the combined effects of mass and stiffness loss. Cyr observed the same trend, with second mode showing a

frequency increase. Finally, in both this panel and the panel with the  $-45^\circ$  cutout, it should be noted that the difficulty in isolating the individual modes led to an increased margin of experimental error. When the modes were not well defined, a judgment was made on exactly where the panel is resonating. Previously insignificant differences in boundary conditions or panel properties could have a significant effect when trying to identify individual modes that were not very strong or well defined.

Table 6.4.  $+45^\circ$  Cutout Panel Results  
Natural Frequency (Hz)

Source	Mode Number				
	1	2	3	4	5
Experiment	500	538	631	685	775
Experiment (Cyr)	513	533	663	700	764
Differ <sup>a</sup> (%)	-3	+1	-5	-2	+1

a -- % difference between this thesis experimental and Cyr's experimental results

[7]

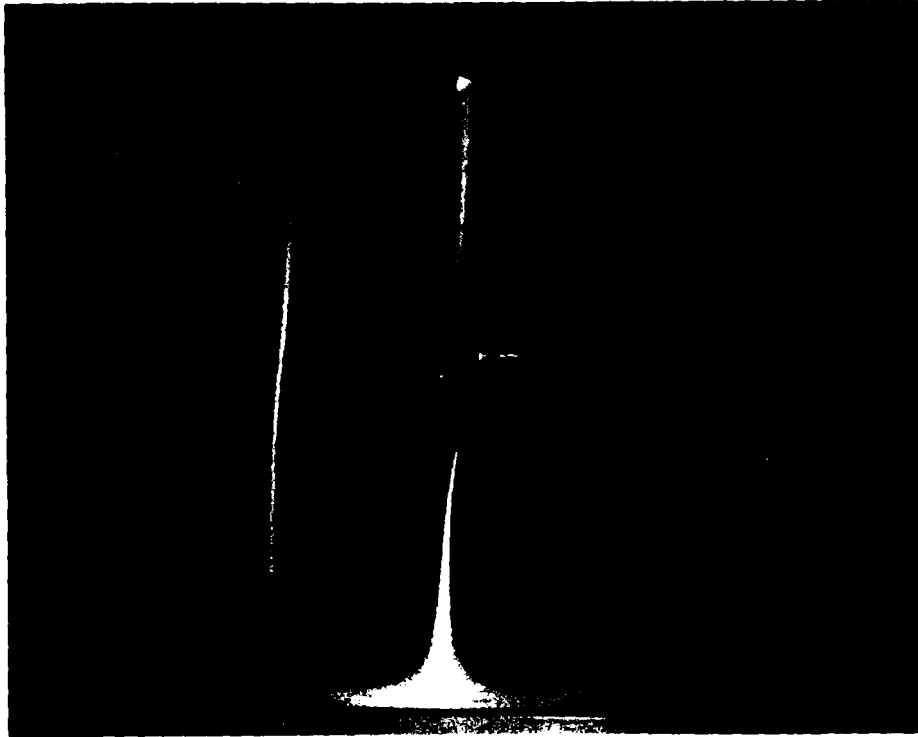


Figure 6.28. +45° Cutout Panel--Mode 1

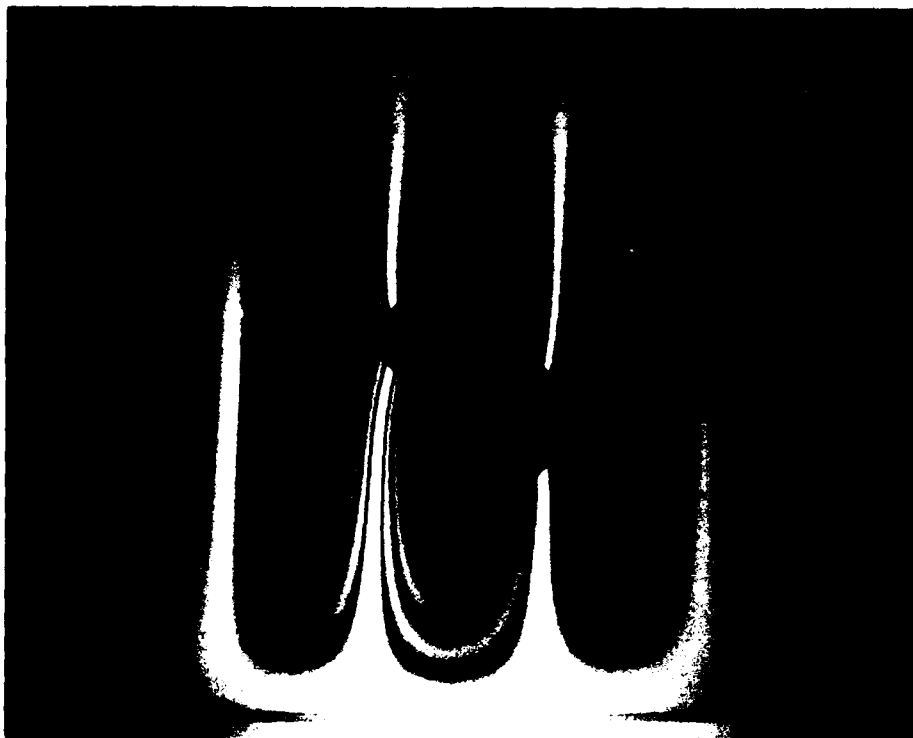


Figure 6.29. +45° Cutout Panel--Mode 2

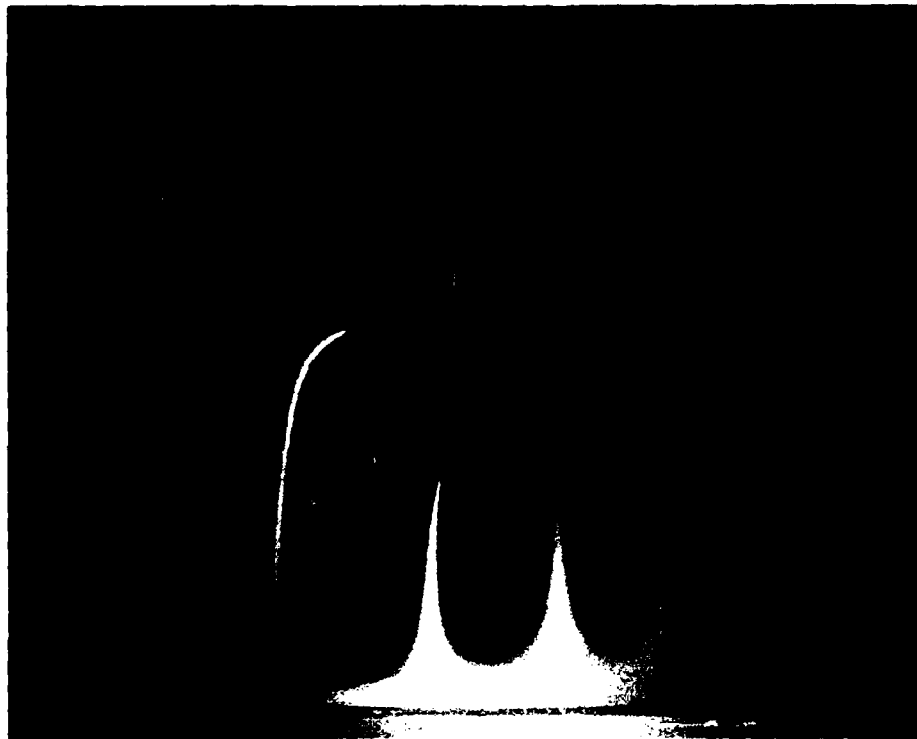


Figure 6.30. +45° Cutout Panel--Mode 3

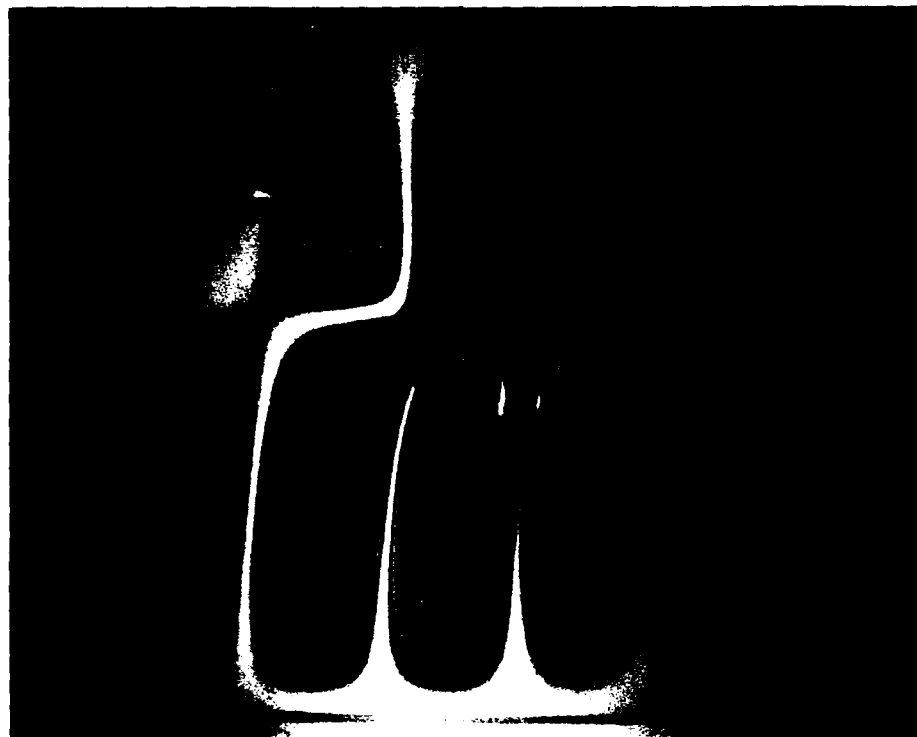


Figure 6.31. +45° Cutout Panel--Mode 4

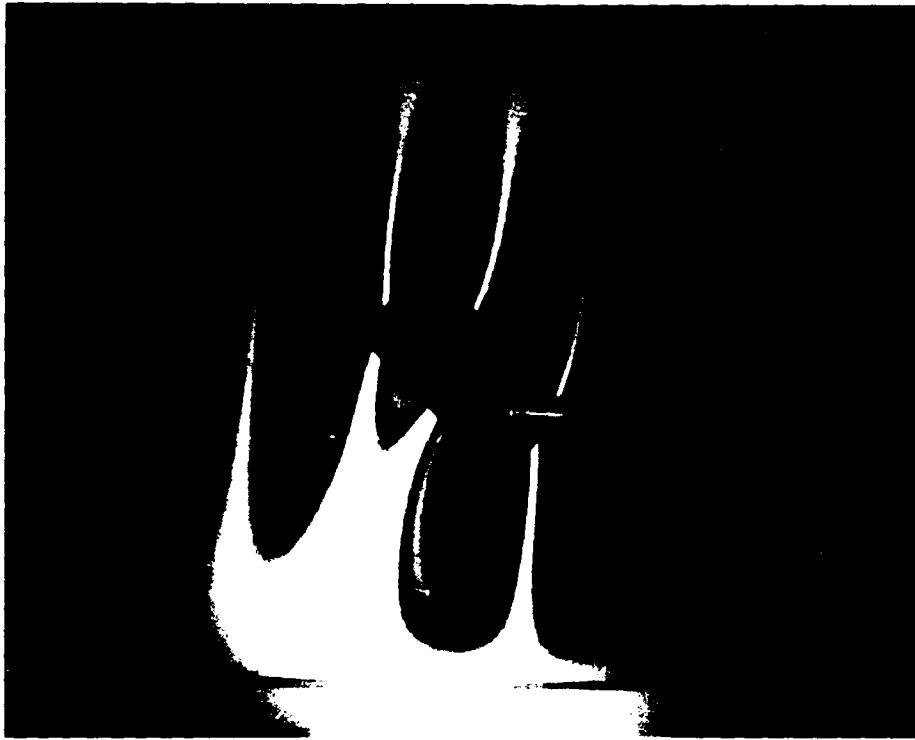


Figure 6.32. +45° Cutout Panel--Mode 5

-45° Cutout Panel. The natural frequencies for the panel with -45° cutouts are presented in Table 6.5, followed by the mode shapes in Figures 6.33 through 6.39. The experimental results do not correlate well with Cyr's results. Mode three was 15% lower than that observed by Cyr, while the other four modes were 4%-7% higher. Again, the mode shapes correlate very well for the first two modes; at the next three modes the more complex shapes do not correlate as well. As in the +45° cutout panel, these higher modes were more prone to contamination between adjacent modes.

The first, second, and fourth modes were obtained with one horn placed one inch below the extreme left corner of

the cutout, as viewed from the rear. Third mode was strongest with the horn centered two inches above the cutout; fifth mode was strongest when the horn was diagonally one inch from the top end of the cutout. This panel was the most difficult to obtain reliable mode shapes. The first two modes were strong, but the higher modes showed inconsistent localized behavior that continuously contaminated adjacent modes.

Unlike the +45° cutout, the first two natural frequencies in this panel increased, whereas Cyr reported a decrease in experimental frequencies and an increase in the STAGSC-1 prediction. He attributed this to either an error in the STAGSC-1 input or a poorly clamped test panel. The agreement between the trend predicted by STAGSC-1 and the trend observed in this experiment would favor Cyr's latter assessment.

Table 6.5. -45° Cutout Panel Results  
Natural Frequency (Hz)

Source	Mode Number				
	1	2	3	4	5
Experiment	528	538	648	666	823
Experiment (Cyr)	494	519	608	782	794
Differ <sup>a</sup> (%)	+7	+4	+7	-15	+4

a -- % difference between this thesis experimental and Cyr's experimental results

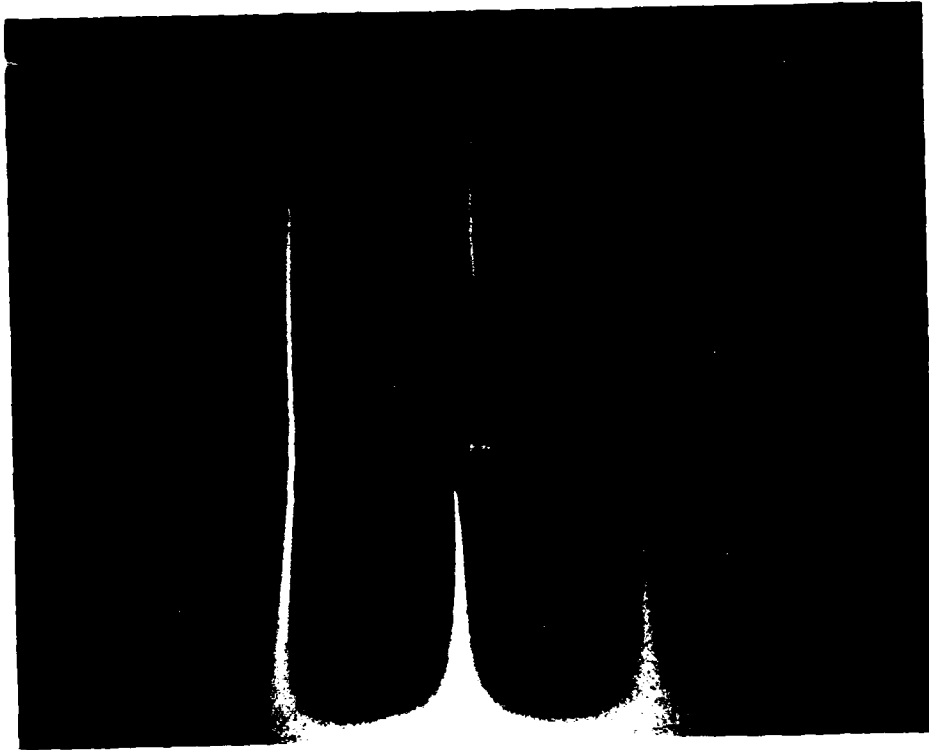


Figure 6.33. -45° Cutout Panel--Mode 1

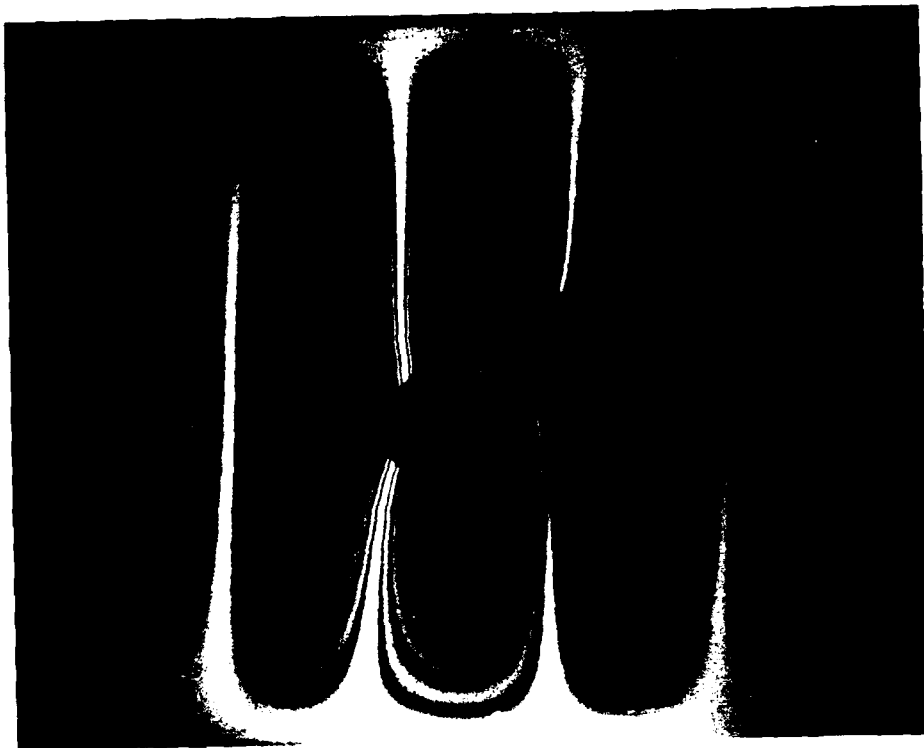


Figure 6.34. -45° Cutout Panel--Mode 2



Figure 6.35. -45° Cutout Panel--Mode 3



Figure 6.36. -45° Cutout Panel--Mode 4

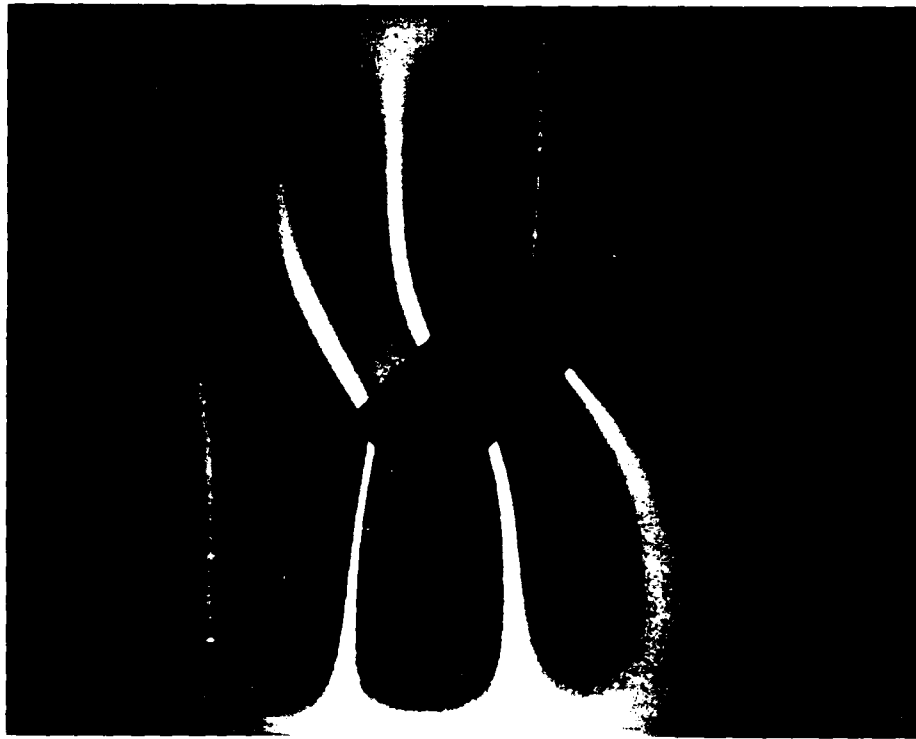


Figure 6.37. -45° Cutout Panel--Mode 5

### Repaired Panels

This section presents the experimental and finite element results for the repaired panels. Frequencies and mode shapes are compared with those of both the solid panel and the corresponding unrepaired panel.

Repaired 0° Cutout Panel. The experimentally determined natural frequencies for the repaired 0° panel are presented in Table 6.6. A graphical summary of the repair effects on natural frequencies is provided in Figure 6.38, followed by the mode shapes in Figures 6.39 through 6.47. The NISA predictions are also included in Table 6.6 and in the accompanying mode shapes.

The real-time holograms displayed the difference in the thermal conductivity of the aluminum patch and the composite panel. Immediately after the hologram was made, both materials began to heat up under the laser light. The aluminum patch, however, showed a greater number of darker and more uniform fringes than the surrounding graphite/epoxy. The rivets could also be seen as rows of dots along the perimeter of the patch. This indicated the greater thermal conductivity of the aluminum as it heated up faster than the composite.

The panel was then acoustically vibrated. The single horn was positioned to excite the panel on the composite part rather than on the aluminum patch to avoid biasing the localized response of the patch. The asymmetric first mode was isolated by putting the horn two inches to the right of the patch. The symmetric second and third modes were excited by centering the horn one inch below the patch. Finally, the horn was placed one inch to the right of the patch to drive the asymmetric fourth and fifth modes.

As the frequency was increased from 75 Hz, faint modal patterns appeared at various frequencies. The first faint pattern had three antinodes and occurred at 185 Hz. The flat, three-lobed Lissajous figure on the oscilloscope confirmed that this was not a natural frequency. As the frequency increased, a four-lobed Lissajous figure appeared at

218 Hz accompanied by a complex, higher-order mode shape. At 266 Hz faint, single antinodes were present on each side of, and above and below, the patch. A clearly recognizable, symmetric mode shape appeared at 277 Hz, followed by a mode shape with two rows of horizontally symmetric antinodes at 289 Hz. The mode shape at 277 Hz resembled the shape of the second natural frequency, which occurred at 334 Hz. The Lissajous figure was a figure eight, which indicated that the panel was vibrating at twice the frequency with which it was being acoustically excited. This phenomenon was observed at a variety of frequencies below the fundamental frequency in every panel. It was clearest when the panel was vibrating 2, 3, or 4 times as fast as it was being excited. The photonic sensor was essential in determining that these mode shapes did not represent the true natural frequencies.

The natural frequency of the asymmetric first mode was only 1% lower than that of the unpatched panel, but 15% lower than that of the solid panel. The mode shape was exactly like the first mode of the solid panel, showing no evidence of the cutout, the dissimilar patch, or the boundary between patch and panel.

The natural frequency of the symmetric second mode was 10% higher than for the cutout panel and 7% higher than for the solid panel. Despite the fact that it behaved as a

stiffer panel as opposed to behaving as a softer panel at the first mode, the mode shape resembled the second mode of the solid panel. Like the first mode, the dynamic behavior of this mode seemed to be dominated by the composite material, while displaying minimal effects of the dissimilar patch material and its boundary with the graphite/epoxy.

Patch effects became increasingly noticeable at the higher modes as localized dynamic behavior increased. The symmetric third mode exhibited some effects of the aluminum patch and rivets. The center antinode was actually one antinode within the patch and two smaller antinodes emanating out of the top and bottom of the patch into the composite material. Thus, there was some localized stiffening occurring at the rivet line. The frequency was 9% higher than that of the unpatched panel and 8% lower than that of the solid panel. Its mode shape more closely resembled that of the fourth mode of the solid panel. This tendency for the third through fifth (the sixth mode also behaved this way) modes to resemble, yet not be in the same frequency sequence, as modes in the original solid panel was observed in each panel. The first two modes, which were the strongest, were the only ones that were consistently restored to both their original mode shape and frequency sequence when the patch was applied. This seemed to indicate the dominance of the total panel, which behaved as a homogeneous

structure rather than under the influence of localized differences in mass and stiffness at the lower modes [19].

With respect to the fourth and fifth modes, the patch had more of an effect on stiffening the panel than it did on adding mass, since the frequencies increased about 6% from the cutout panel. The overall properties of the solid panel were nearly restored, as the frequency differences were within 3% of the solid panel. Again, the mode shapes were out of sequence.

The NISA results were consistently high, yet accurately predicted the trend. The mode shapes revealed no patch effects, indicating that the repair was modeled as a perfect repair. This was reasonable, especially given the constraints of this program. In fact, a finite element program would make a perfect model unless the individual characteristics of each rivet were put into the model.

Table 6.6. 0° Repaired Panel Results  
Natural Frequency (Hz)

Source	Mode Number				
	1	2	3	4	5
Repair (Experiment)	439	555	663	745	795
Repair (NISA)	490	548	730	884	n/a
Differ <sup>a</sup> (%)	+12	-1	+10	+19	n/a
Cutout (Experiment)	445	507	606	708	749
Differ <sup>b</sup> (%)	-1	+9	+9	+5	+6
Solid (Experiment)	514	519	716	727	821
Differ <sup>c</sup> (%)	-15	+7	-7	+2	-3

a -- % difference between experimental and NISA results

b -- % difference between repaired panel and unrepaired panel (experimental)

c -- % difference between repaired panel and solid panel (experimental)

# REPAIRED "O" CUTOUT

SOLID vs CUTOUT vs REPAIR

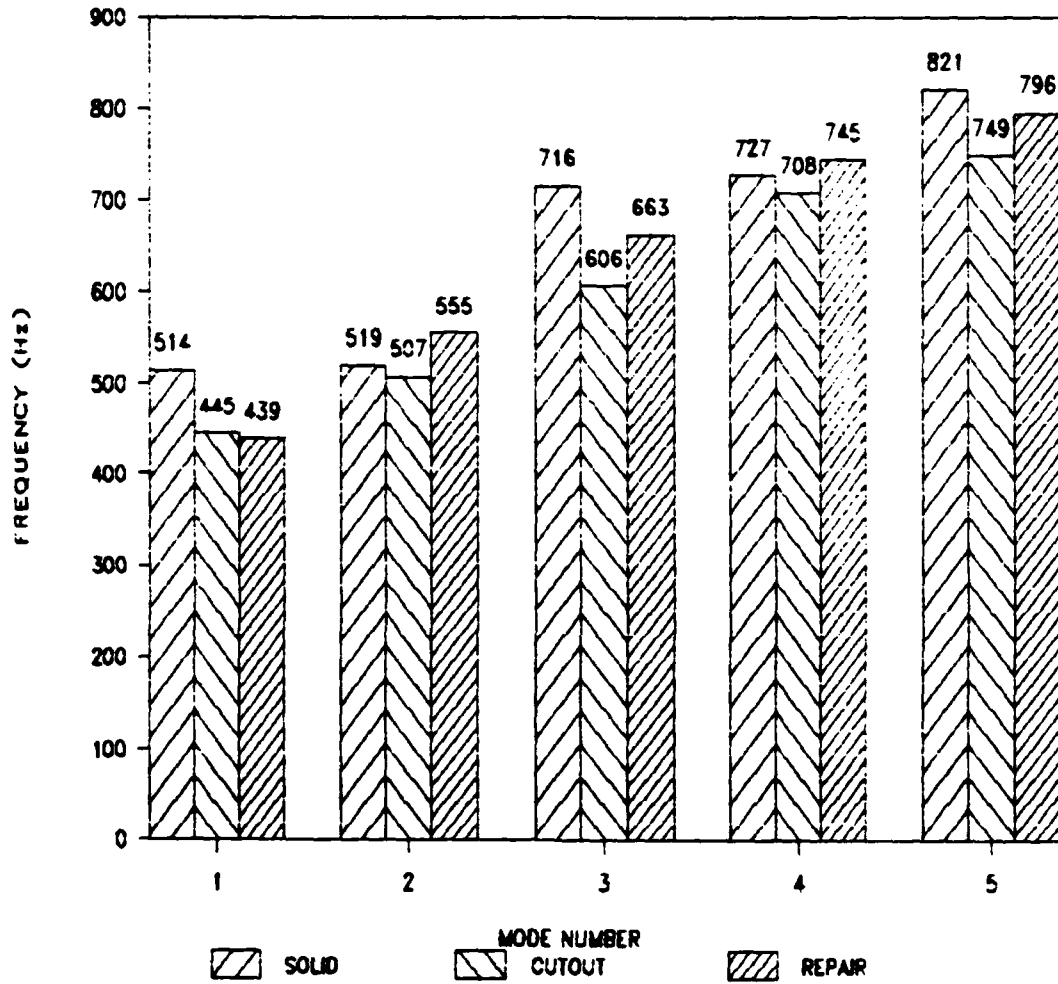
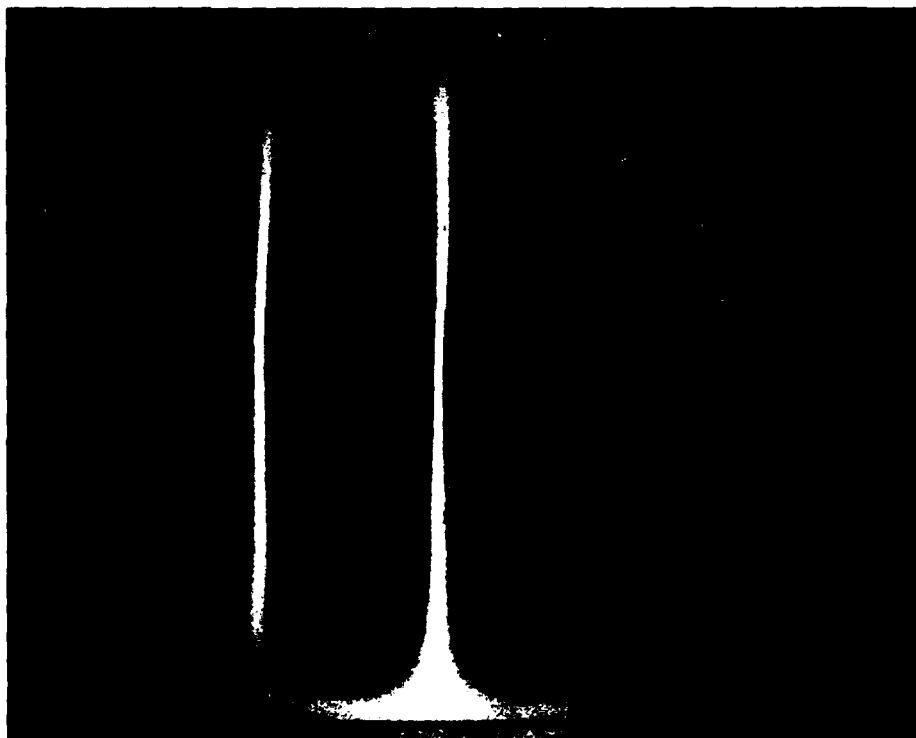


Figure 6.38. Summary of Repair Effect on 0° Cutout Panel



Figures 6.39. 0° Repaired Panel--Mode 1

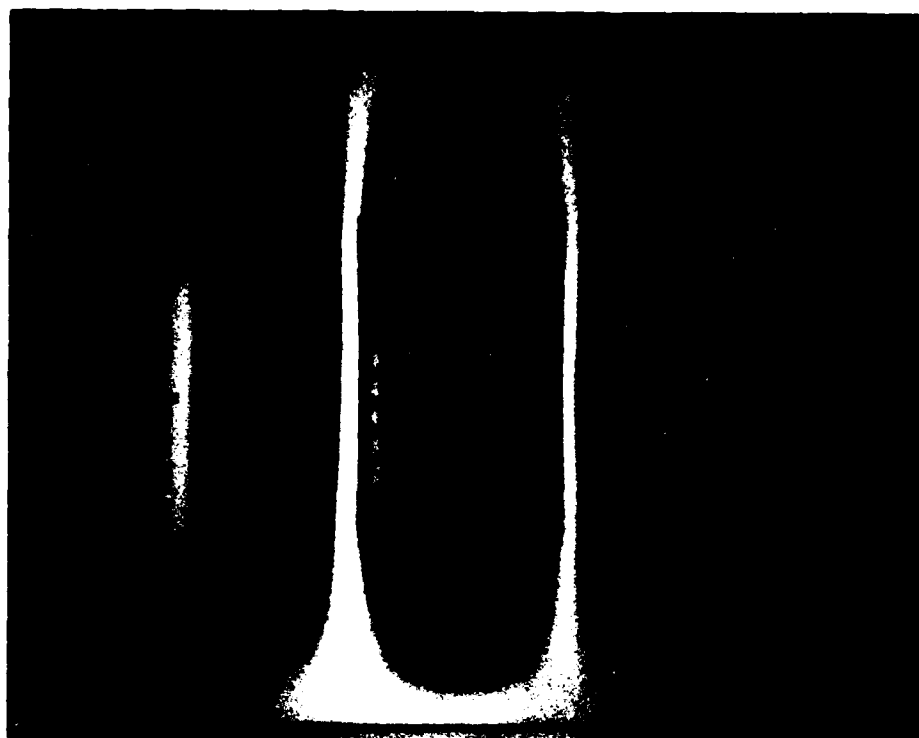


Figure 6.40. 0° Repaired Panel--Mode 2



Figure 6.41. 0° Repaired Panel--Mode 3

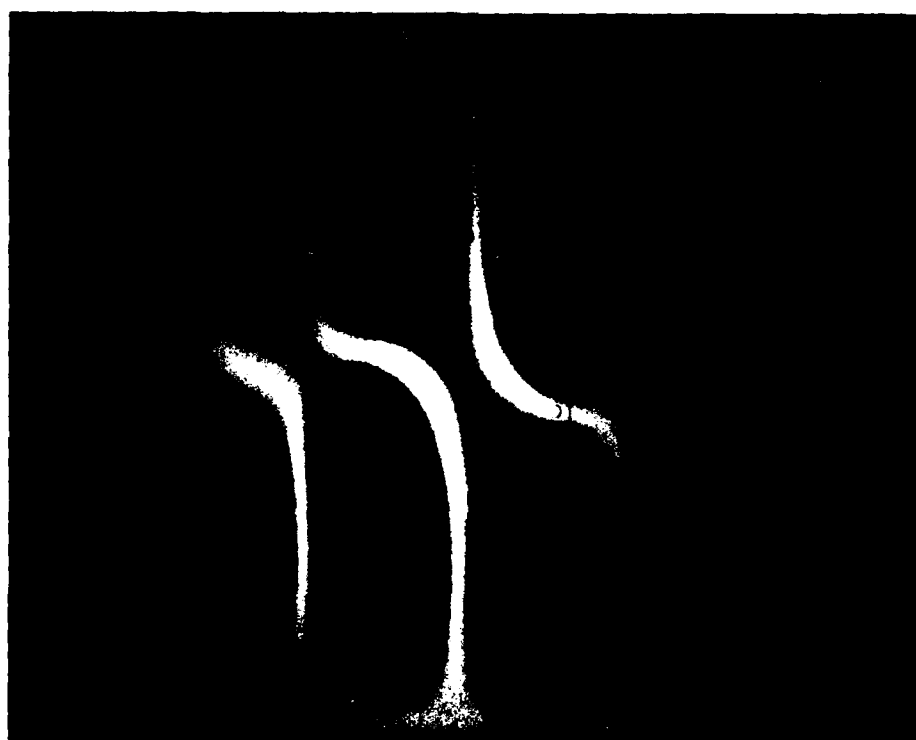


Figure 6.42. 0° Repaired Panel--Mode 4



Figure 6.43. 0° Repaired Panel--Mode 5

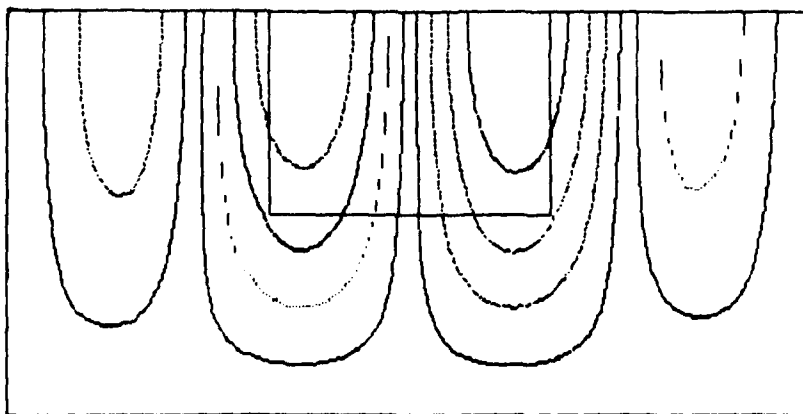


Figure 6.44. 0° Repaired Panel--Mode 1 (NISA)

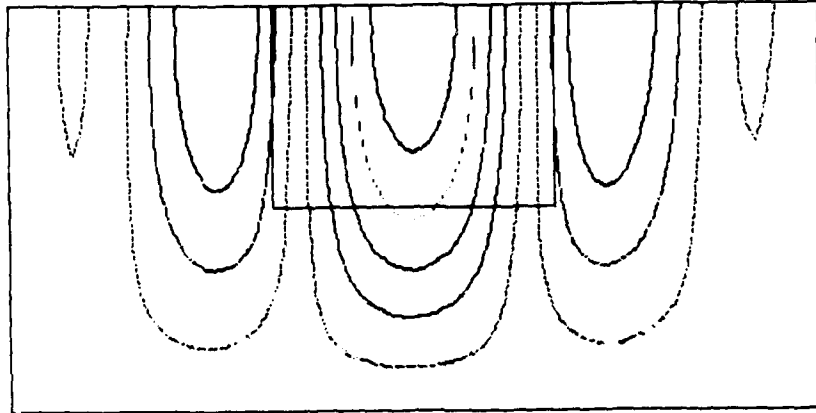


Figure 6.45. 0° Repaired Panel--Mode 2 (NISA)

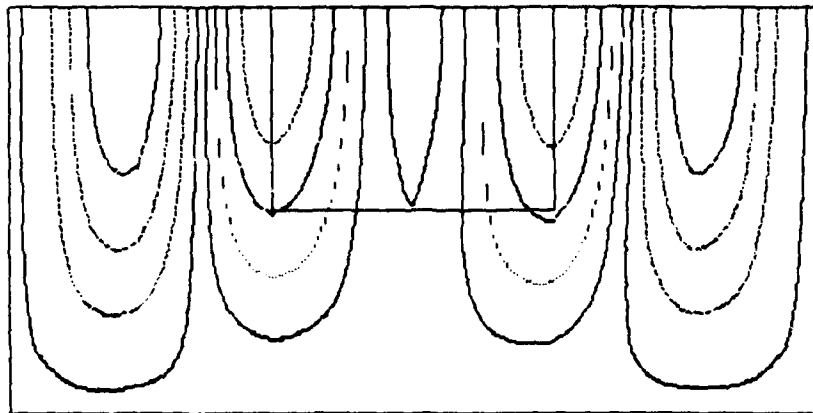


Figure 6.46. 0° Repaired Panel--Mode 3 (NISA)

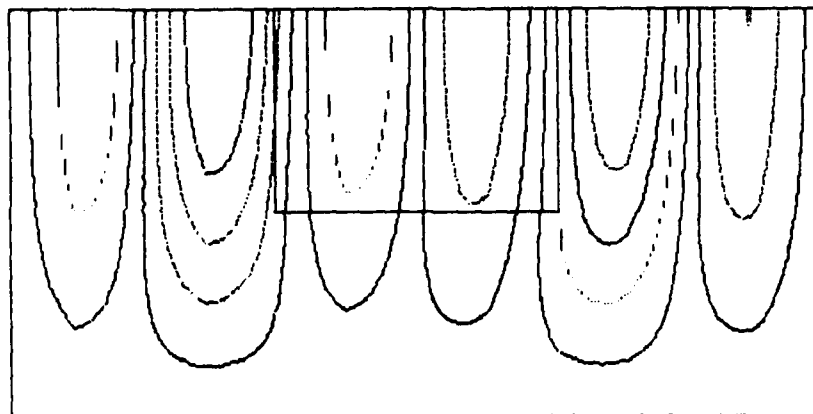


Figure 6.47. 0° Repaired Panel--Mode 4 (NISA)

Repaired 90° Cutout Panel. The experimentally determined natural frequencies for the repaired 90° panel are presented in Table 6.7. A graphical summary is provided in Figure 6.48, followed by the mode shapes in Figures 6.49 through 6.57. The NISA predictions are included in Table 6.7 and in the accompanying mode shape plots. Again, restoration of the solid panel mode shapes and recovery of some stiffness, although at the expense of additional mass, were observed.

As in the 0° panel, the real-time holograms displayed the difference in thermal conductivity between the aluminum

patch and the composite panel. Immediately after the real-time hologram was made, the aluminum patch showed a greater number of darker and more uniform fringes than the surrounding graphite/epoxy. The rivets were visible again. This thermal behavior was consistent with that observed in the 0° patch and was also observed in the +45° and -45° patches.

The panel was acoustically excited with a single horn. The asymmetric first mode was isolated with the horn one inch below and one inch to the left of center of the bottom of the patch. This took advantage of one of the two strongest antinodes. The horn was centered one inch below the patch to excite the symmetric second mode; one inch above the patch and to the left of center to drive the asymmetric third mode; one inch below the left bottom corner of the patch for the fourth mode; and one inch to the left of the patch to drive the fifth mode.

As the frequency was increased, faint mode shapes occurred once again at various frequencies. The lowest recognizable pattern was a symmetric mode with three antinodes at 174 Hz. The three-lobed Lissajous figure confirmed that this was not a natural frequency. It indicated that the panel was vibrating at three times the frequency of the noise with which it was being driven. This made sense because the true symmetric second mode was at 523 Hz, which

was approximately three times 174 Hz. A similar behavior occurred for the asymmetric first mode. A faint asymmetric mode at 253 Hz had a corresponding two-lobed Lissajous figure. Thus, the panel was vibrating at twice the frequency of the excitation noise. This was consistent because the true first mode occurred at twice 253 Hz, or 506 Hz.

The asymmetric first mode was 2% below the first mode of the cutout panel and 1% below the first mode of the solid panel. The mode shape of the solid panel was restored except for slight, yet symmetric, distortion at the boundary of the patch. The four fringe patterns bowed outward slightly. Overall, however, the patch acted as part of the total panel rather than displaying its own unique fringe patterns. Interestingly, the mode switch that had occurred between the first and second modes in the cutout panel had been reversed by the presence of the patch.

The symmetric second mode was 4% lower than for the cutout panel and only 1% higher than for the solid panel. The mode shape of the solid panel had once again been restored by the patch, reversing the aforementioned mode switch. As with first mode, there was a slight bowing of fringe pattern at the patch boundary and some slight distortion in the vertical direction. Overall, however, the patch behaved as an integral part of the panel. Thus, the behavior at the two lower and stronger natural frequencies was dominated by the overall composite panel.

As in the 0° patch, the effect of the patch was introduced in the higher modes as displacement patterns became more localized in the panel. The symmetric third mode had a 7% higher frequency than third mode of the patched panel, while its frequency was 1% lower than the solid panel. Mode shapes were out of sequence at these higher modes as described in the previous section. The panel exhibited the effects of the aluminum patch and rivets, as bowing and more severe distortion at the patch boundaries occurred.

Fourth mode was 7% higher than in the unpatched panel and 4% higher than in the solid panel. Fifth mode was 8% higher than the corresponding mode for the unpatched panel versus 3% lower than fifth mode for the solid panel. The mode shapes were quite different, again showing the inconsistency in mode shape behavior at the higher modes.

Overall, the predictability of panel behavior decreased at the higher modes. Localized effects begin to appear at these higher-order modes. Patch and rivet orientation, and differences in the quality of the repair resulted in unequal stress distribution and stiffness changes, causing unique behavior in the vicinity of the repair. The boundary conditions appeared to be as reliable as they were with the other panels. However, the repair restored the natural frequencies and mode shapes at the two lowest and strongest modes.

Table 6.7. 90° Repaired Panel Results  
Natural Frequency (Hz)

Source	Mode Number				
	1	2	3	4	5
Repair (Experiment)	509	523	706	758	796
Repair (NISA)	500	535	749	800	n/a
Differ <sup>a</sup> (%)	-2	+2	+6	+6	n/a
Cutout (Experiment)	519	546	656	712	733
Differ <sup>b</sup> (%)	-2	-4	+7	+6	+8
Solid (Experiment)	514	519	716	727	821
Differ <sup>c</sup> (%)	-1	+1	-1	+4	-3

a -- % difference between experimental and NISA results

b -- % difference between repaired panel and unrepaired panel (experimental)

c -- % difference between repaired panel and solid panel (experimental)

# REPAIRED "90" CUTOUT

SOLID vs CUTOUT vs REPAIR

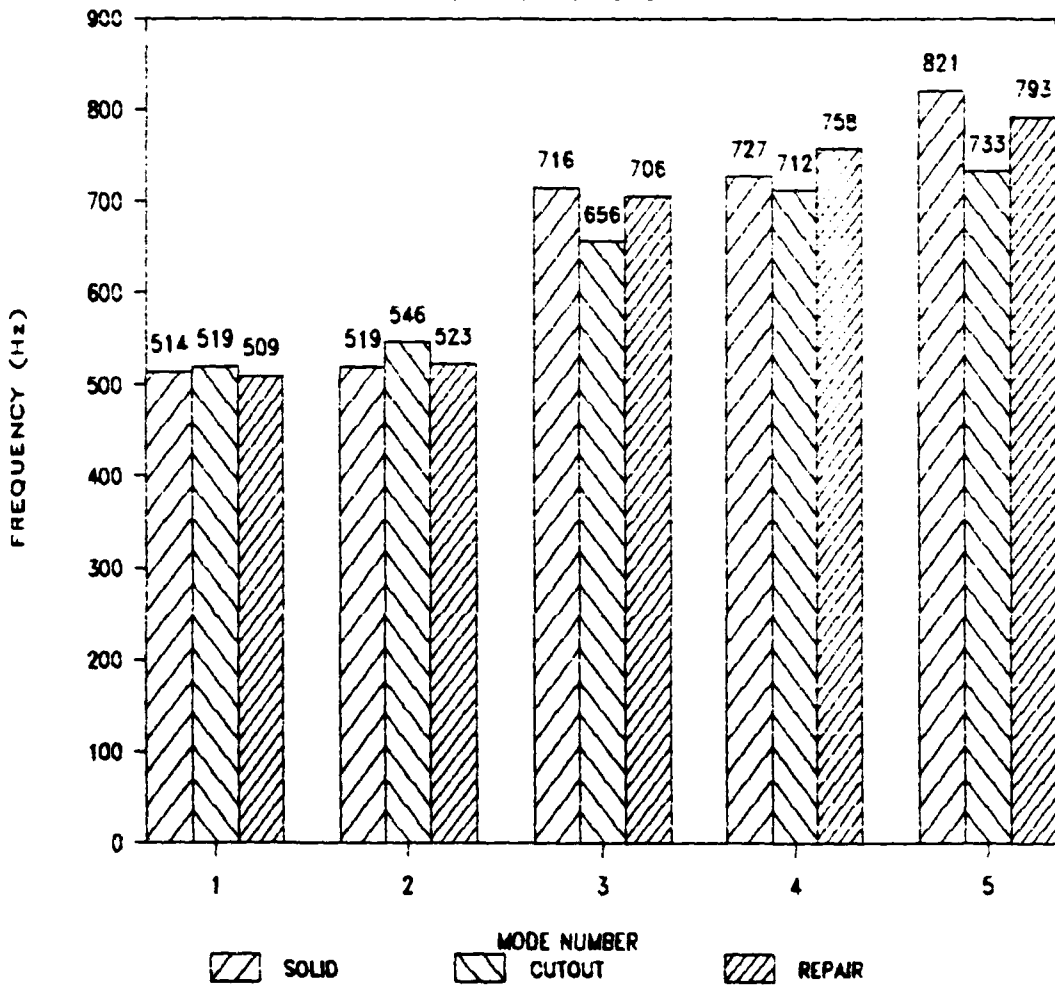


Figure 6.48. Summary of Repair Effect on 90° Cutout Panel

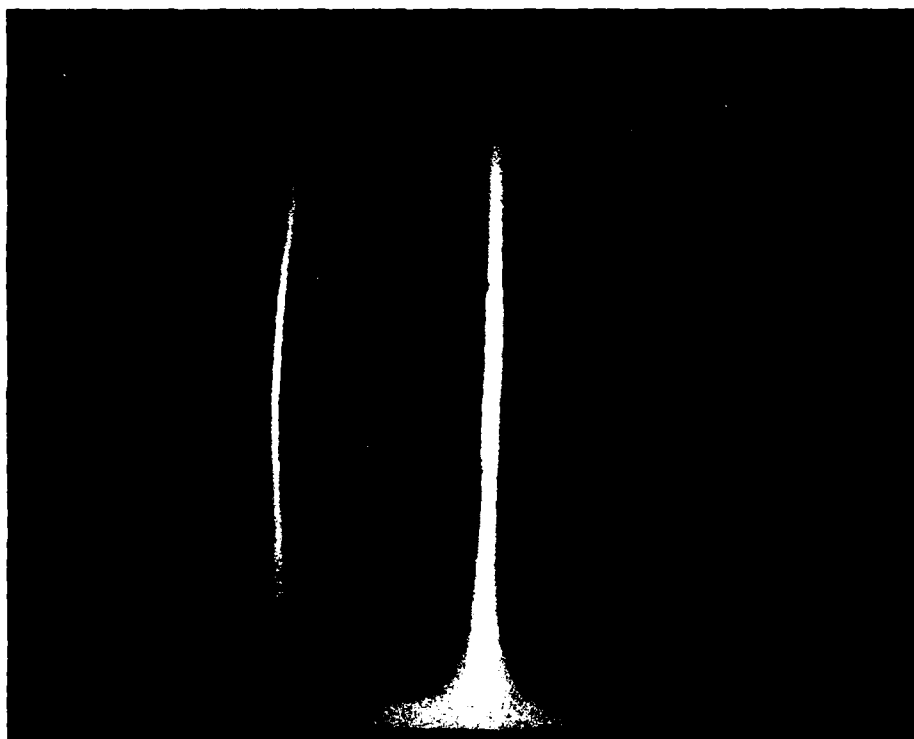


Figure 6.49. 90° Repaired Panel--Mode 1

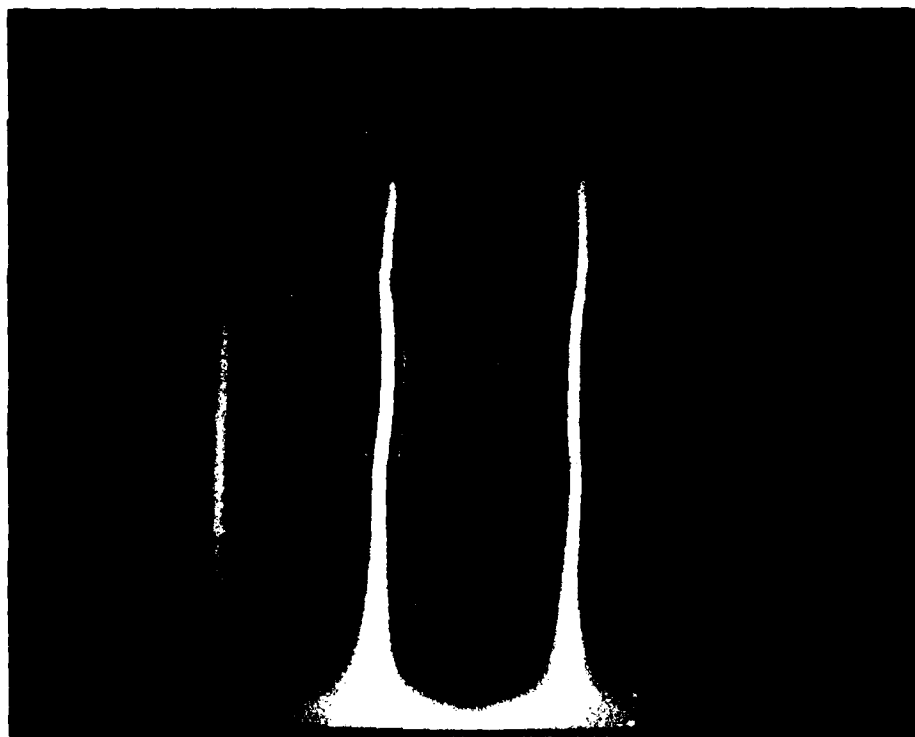


Figure 6.50. 90° Repaired Panel--Mode 2

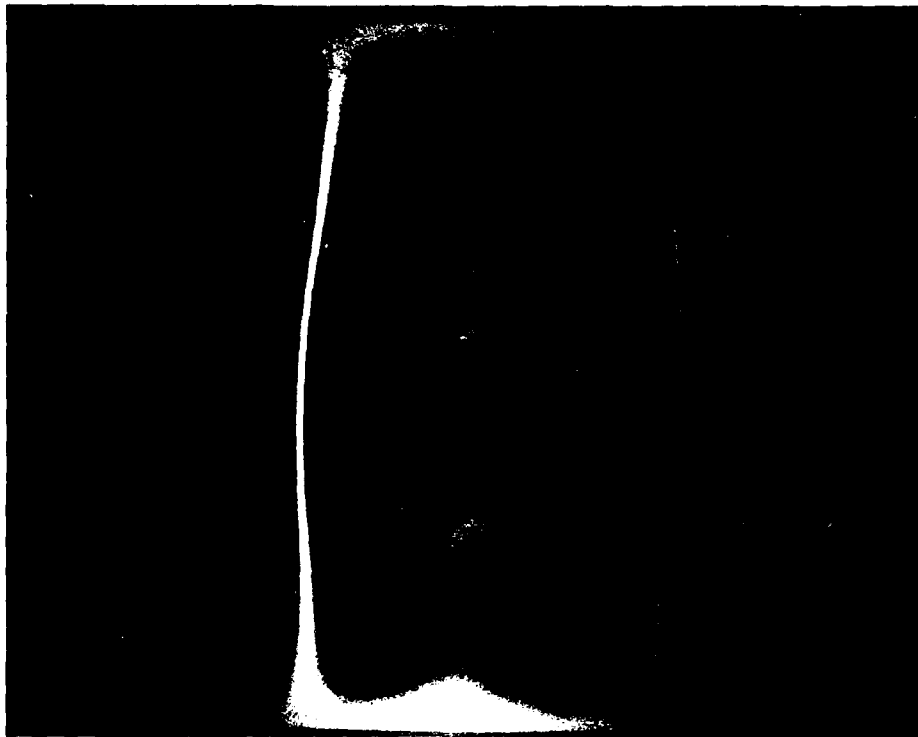


Figure 6.51. 90° Repaired Panel--Mode 3

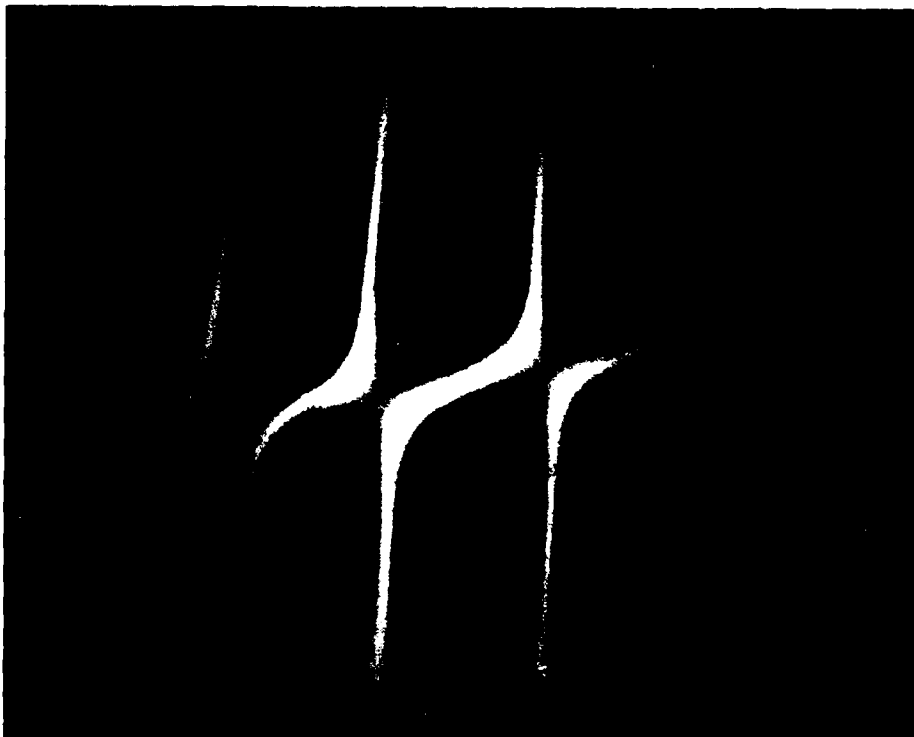


Figure 6.52. 90° Repaired Panel--Mode 4

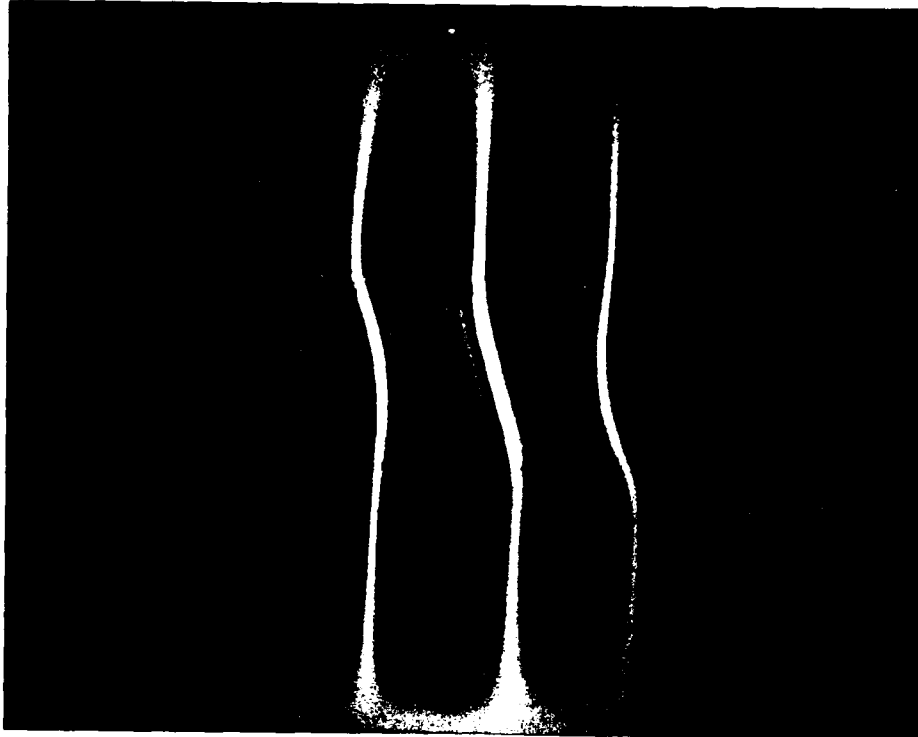


Figure 6.53. 90° Repaired Panel--Mode 5

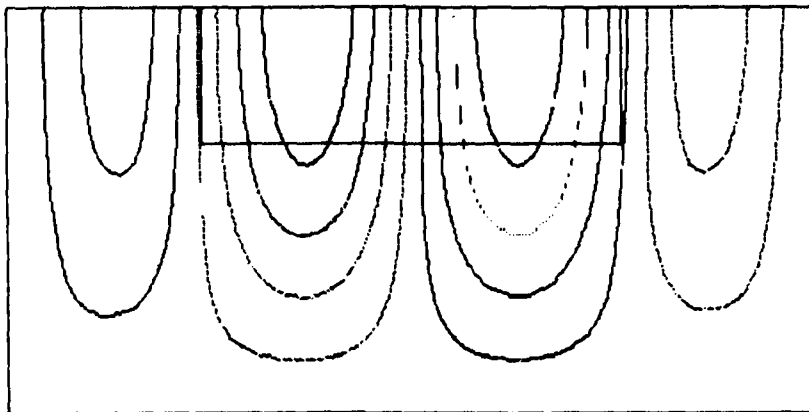


Figure 6.54. 90° Repaired Panel--Mode 1 (NISA)

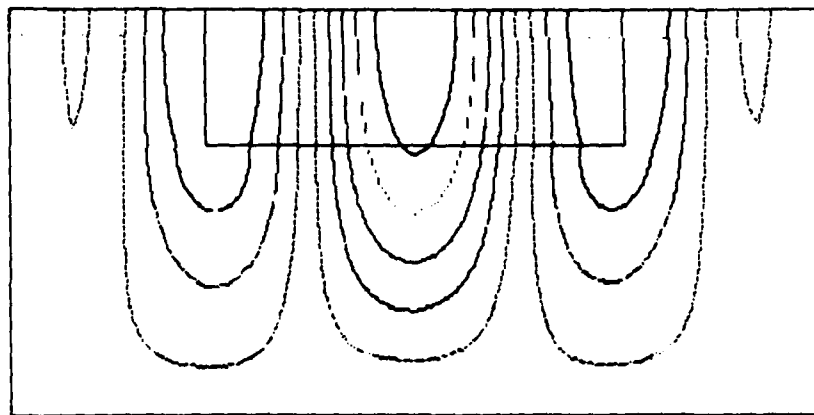


Figure 6.55. 90° Repaired Panel--Mode 2 (NISA)

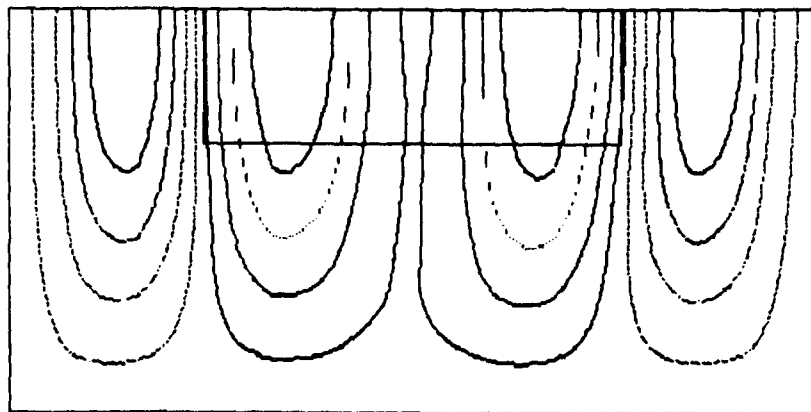


Figure 6.56. 90° Repaired Panel--Mode 3 (NISA)

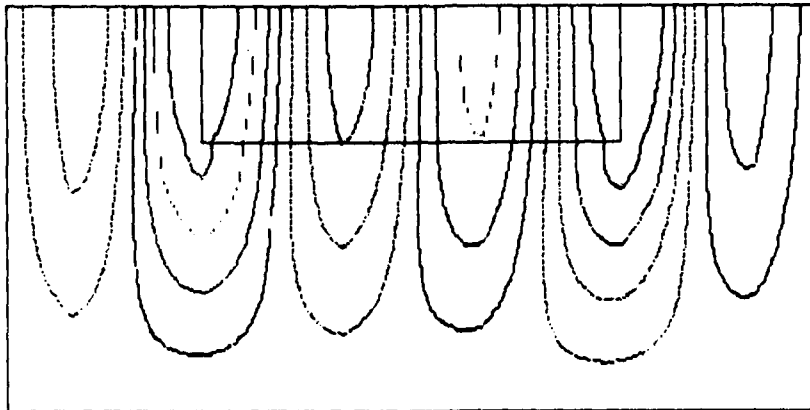


Figure 6.57. 90° Repaired Panel--Mode 4 (NISA)

Repaired +45° Cutout Panel. The natural frequencies for the repaired +45° cutout panel are presented in Table 6.8. A graphical summary is provided in Figure 6.58, followed by the mode shapes in Figures 6.59 through 6.63. A NISA finite element analysis of this panel was not done. As in the other repaired panels, restoration of the solid panel mode shapes and recovery of stiffness at the expense of additional mass was observed.

As before, the single horn was located to take advantage of antinodes and nodal lines when exciting the various mode shapes. The asymmetric first was isolated with the horn

three inches below the extreme right corner of the patch. The symmetric second and third modes were excited most clearly when the horn was centered two inches below the patch. Fourth and fifth modes were obtained when the horn was located one inch above the top right corner of the patch and four inches above the extreme left corner of the patch, respectively.

The same frequency-scanning technique was used to observe the dynamic behavior of this panel. The difference in the thermal activity of the aluminum and rivets versus the composite material was again evident. Faint mode shapes were once observed during the frequency sweep from 75 Hz to the fundamental frequency of 506 Hz. A faint asymmetric mode and an associated three-lobed Lissajous figure were noted at 170 Hz. This was consistent, since it occurred at 170 Hz, about one-third of the 506 Hz fundamental frequency. Similarly, a two-lobed Lissajous figure accompanied a faint asymmetric mode at 253 Hz, which is one-half of the first mode. Similar phenomena occurred at other frequencies below the fundamental frequency.

The asymmetric first mode was a 1% increase over the frequency of the first mode of the cutout panel and a 2% decrease from the solid panel first mode. The general mode shape of the solid panel was restored. There was some distortion at the boundaries of the patch, especially where

they coincided with the asymmetric antinodes. The fringe bowing noted in the  $90^\circ$  patch was again evident in this panel. Overall, however, the patch behaved as part of the overall panel, rather than displaying unique fringe patterns.

The symmetric second mode was 2% lower than in the cut-out panel and 1% higher than in the solid panel. The mode shape of the solid panel was once again restored by the repair. As with first mode, slight bowing at the patch boundary and some fringe distortion in the vertical direction were observed. Overall, the patch again behaved as an integral part of the panel. Thus, as in  $0^\circ$  and  $90^\circ$  patched panels, the behavior of the overall composite panel was dominant at the two lower and stronger natural frequencies.

Patch effects were again introduced into the panel at the higher modes as unique behavior became more localized. The third mode was symmetric and had a 14% higher resonant frequency than third mode of the unpatched panel. This frequency was only 1% higher than that of the solid panel. The mode shape switched its sequence in the frequency order with respect to its sequence in the solid panel, now resembling the fourth mode. The panel exhibited some effects of the aluminum patch and rivets. The bowing effect was present, as well as more severe fringe distortion at the patch boundaries. In addition, the center antinode did not

emanate vertically through the patch. Instead, one small antinode appeared below the patch and one appeared above it. The patch itself, however, remained relatively stiff in the vertical direction between these two small antinodes.

The fourth mode was 15% higher than the same mode for the unpatched panel and 9% higher than for the solid panel. The mode shape sequence changed once again. The fifth mode was 6% higher than the corresponding mode for the unpatched panel versus a negligible change from the fifth mode of the solid panel. The mode shape was distorted. The two center antinodes were biased along the patch boundary, showing the localized nature of the patch's stiffening effect. The two center antinodes were biased along the boundary of the patch and the two larger antinodes had distinct deformities that revealed the increasingly significant stiffening effect of the patch.

Overall, this repaired panel displayed similar behavior to that of the 0° and 90° repaired panels. The first two natural frequencies were restored to within 2% of the solid panel and the mode shapes were restored, with the exception of some slight distortion at the patch boundaries. The properties of the total panel dominated the behavior of these two strong modes. The higher-order, weaker modes reflected the increased influence of the patch and the very stiff overlap area where it is riveted to the composite material.

Table 6.8. +45° Repaired Panel Results  
Natural Frequency (Hz)

Source	Mode Number				
	1	2	3	4	5
Repair (Experiment)	506	525	721	789	820
Cutout (Experiment)	500	538	631	685	775
Differ <sup>a</sup> (%)	+1	-2	+14	+15	+6
Solid (Experiment)	514	519	716	727	821
Differ <sup>b</sup> (%)	-2	+1	+1	+9	0

a -- % difference between repaired panel and unrepaired panel (experimental)

b -- % difference between repaired panel and solid panel (experimental)

# REPAIRED "+45" CUTOUT

SOLID vs CUTOUT vs REPAIR

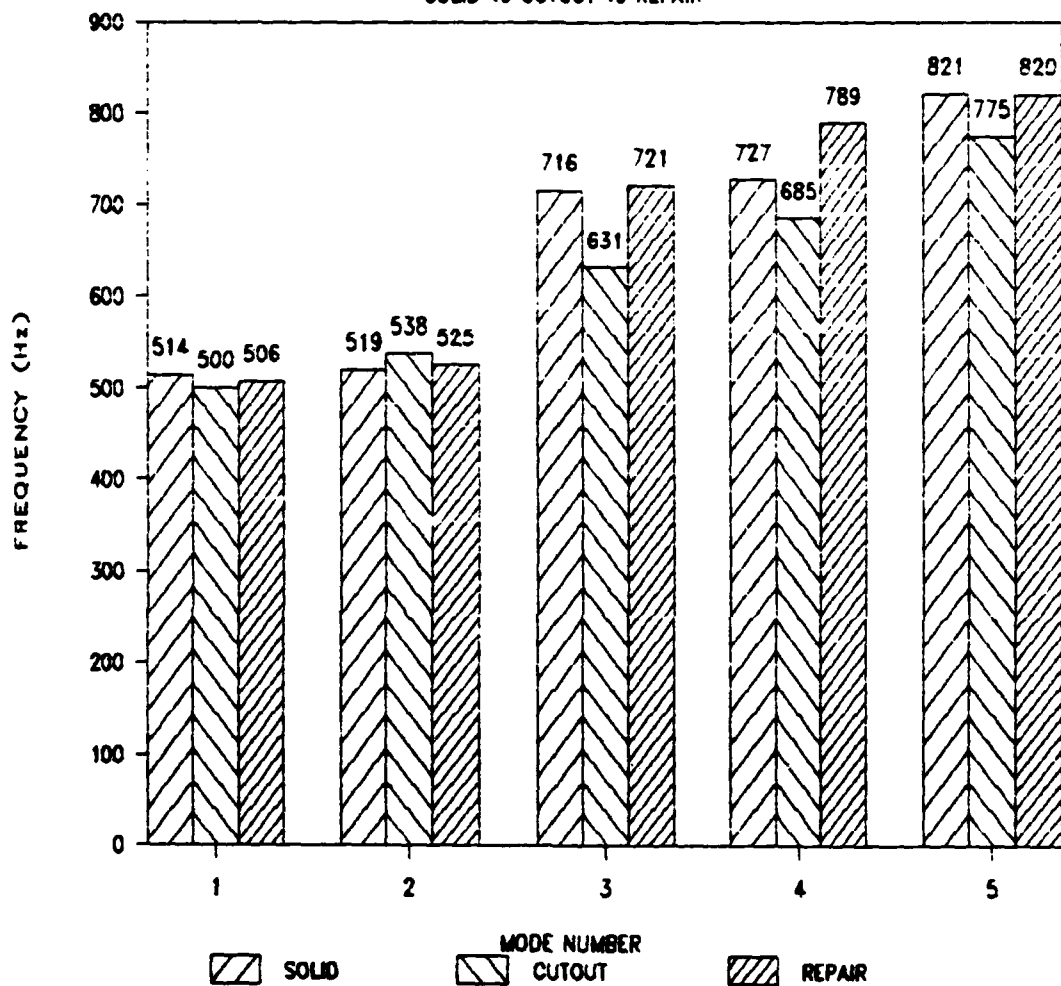


Figure 6.58. Summary of Repair Effect on +45° Cutout Panel

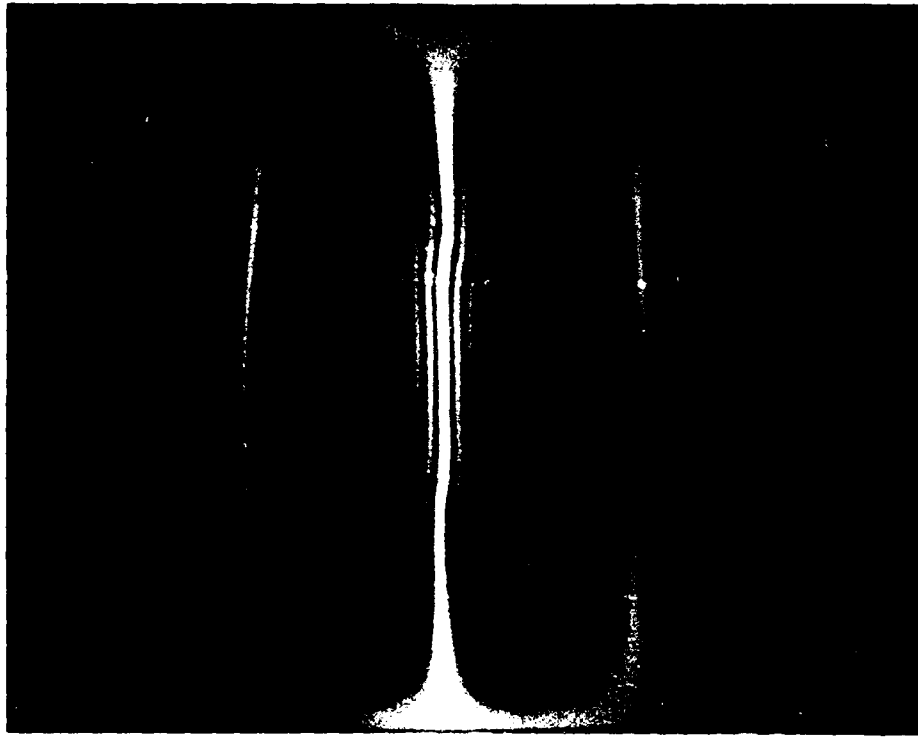


Figure 6.59. +45° Repaired Panel--Mode 1

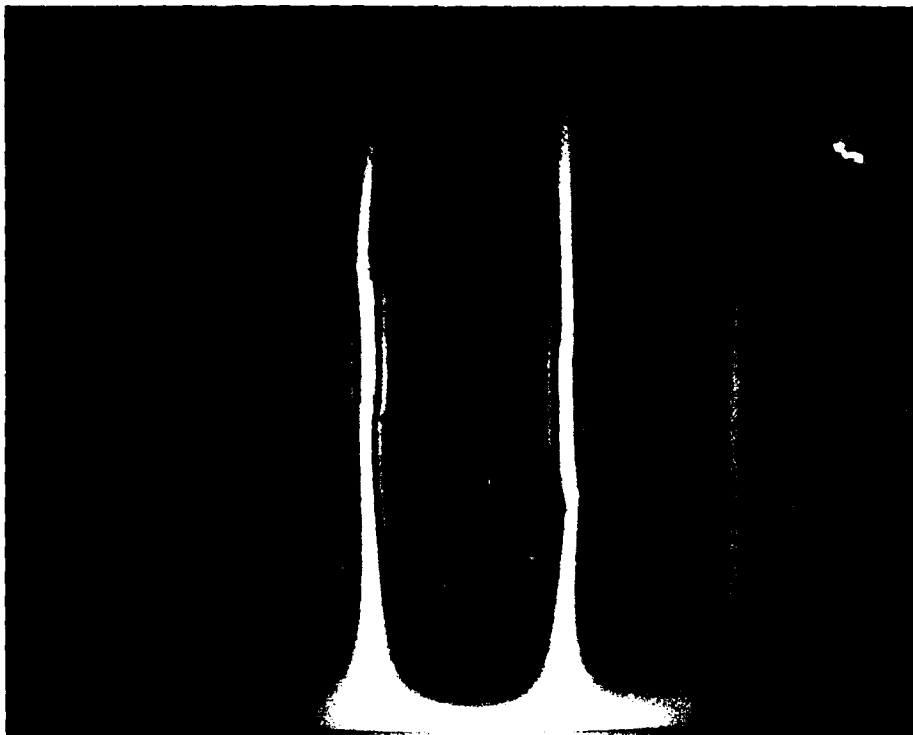


Figure 6.60. +45° Repaired Panel--Mode 2



Figure 6.61. +45° Repaired Panel--Mode 3

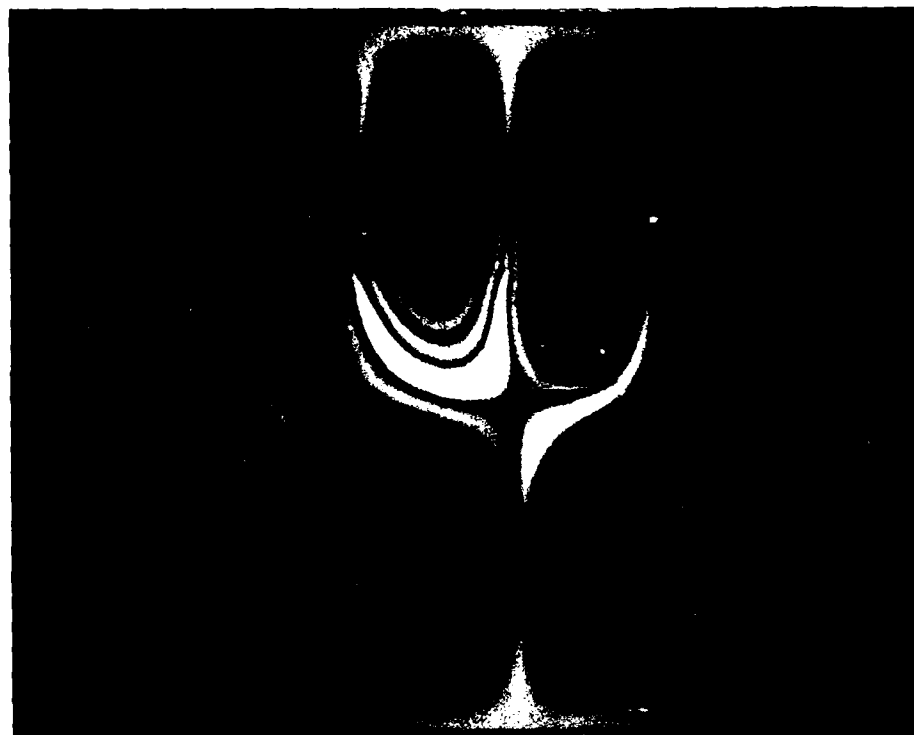


Figure 6.62. +45° Repaired Panel--Mode 4

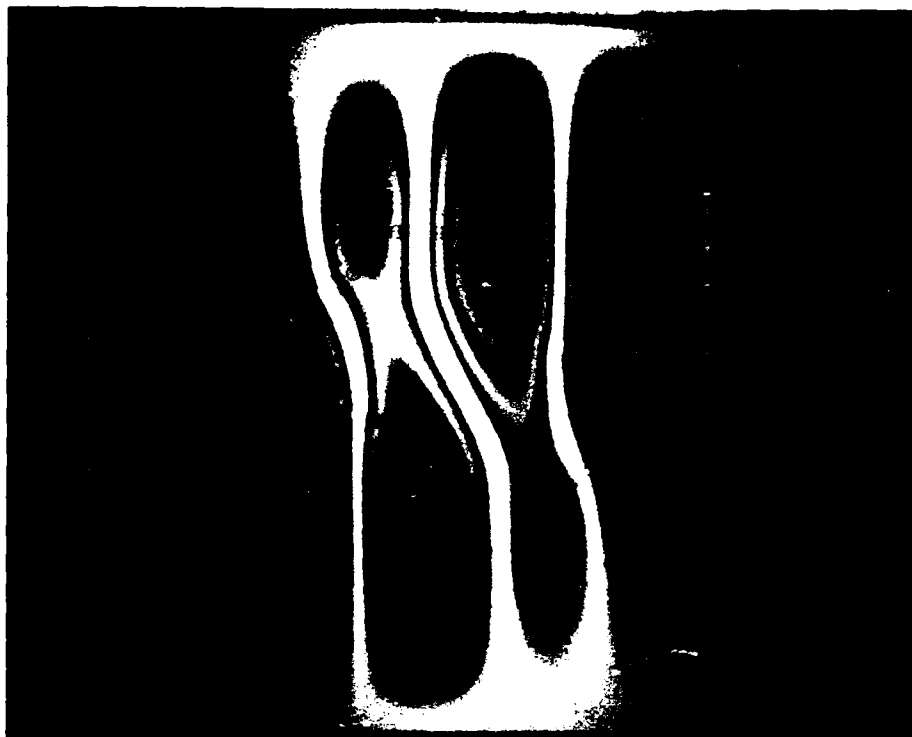


Figure 6.63. +45° Repaired Panel--Mode 5

Repaired -45° Cutout Panel. The natural frequencies for the repaired -45° cutout panel are presented in Table 6.9. A graphical summary is provided in Figure 6.64, followed by the mode shapes in Figures 6.65 through 6.69. A NISA finite element analysis of this panel was not done. The results of this repair were very similar to the results observed in the +45° panel. The trends in frequency change between the repaired panel and the cutout panel, and between the repaired panel and the solid panel, were very similar for both this panel and the +45° panel. Mode shapes were also very similar. This section will highlight the similarities, but concentrate on the differences.

The asymmetric first and fifth modes were activated with the horn three inches above and one inch inboard from the extreme right corner of the patch. To excite the symmetric second and third modes, the horn was centered three inches above the patch. It was located three inches directly above the extreme right corner of the patch to isolate the fourth mode shape.

The dissimilar thermal activity of the aluminum patch, rivets, and composite material was observed. Mode shape behavior observed while scanning the frequency range below first mode was similar to that observed in the other panels. The photonic sensor proved to be a reliable and necessary instrument in isolating true natural modes.

The asymmetric first mode at 505 Hz was only 1 Hz less than first mode for the +45° patched panel. The fundamental mode shapes for these two repaired panels were mirror images and, coincidentally, correlate well with the first mode of the solid panel. The frequency change from the solid panel was less than 2%. The change from the cutout panel was a 4% decrease. This would indicate that the additional stiffness introduced by the patch was less significant than the added mass of the patch and rivets.

The symmetric second mode was within 2% of the second mode of the +45° patched panel, and again, had a very similar mode shape. The first mode shape of the solid panel was

restored, with slight bowing and distortion at the patch boundaries. Like first mode, second mode was also 4% lower than that of the unrepaired panel. This further indicates that mass increase dominated the change. In spite of this, the mode shape showed that the patch behaved, in general, as an integral part of the overall panel, rather than displaying unique mode shapes. As before, the two lower and stronger natural modes were dominated by the total behavior of the composite panel.

Patch effects were introduced in the higher modes as the displacements became more localized in the panel. The third mode was symmetric, and like third mode in the +45° patched panel, had over a 10% increase in frequency from the cutout panel. The localized mode shapes were similar around the patch, but the two largest antinodes showed the same distinct biasing toward the -45° fiber direction.

The fourth mode was 14% higher than the same mode for the unpatched panel and 3.2% higher than for the solid panel. Patching the +45° panel had increased its frequency by a similar amount (15%). The mode shapes differed for these modes. Once again, at the higher-order modes there was the tendency to switch the sequence in which specific mode shapes appeared. The effect these patches had on the fifth natural frequency differed. The -45° patch had a 2% frequency decrease from its corresponding unpatched panel,

while the +45° patch caused a 6% increase. Each repair restored the fifth natural frequency of the solid panel to within 2% of its original value. The mode shapes were, however, quite different. The localized effects of the patch were evident by the distortion and biasing of the central antinodes.

Thus, the behavior of the panel at the two lower, stronger modes was consistent and indicative of the patch behaving as an integral part of the total panel. As the frequencies increased, localized behavior increased, and resulted in distorted and unpredictable mode shapes and frequencies.

Table 6.9. -45° Repaired Panel Results  
Natural Frequency (Hz)

Source	Mode Number				
	1	2	3	4	5
Repair (Experiment)	505	516	717	750	806
Cutout (Experiment)	528	538	648	659	823
Differ <sup>a</sup> (%)	-4	-4	+11	+14	-2
Solid (Experiment)	514	519	716	727	821
Differ <sup>b</sup> (%)	-2	-1	0	+3	-2

a -- % difference between repaired panel and unrepaired panel (experimental)

b -- % difference between repaired panel and solid panel (experimental)

# REPAIRED "-45" CUTOUT

SOLID vs CUTOUT vs REPAIR

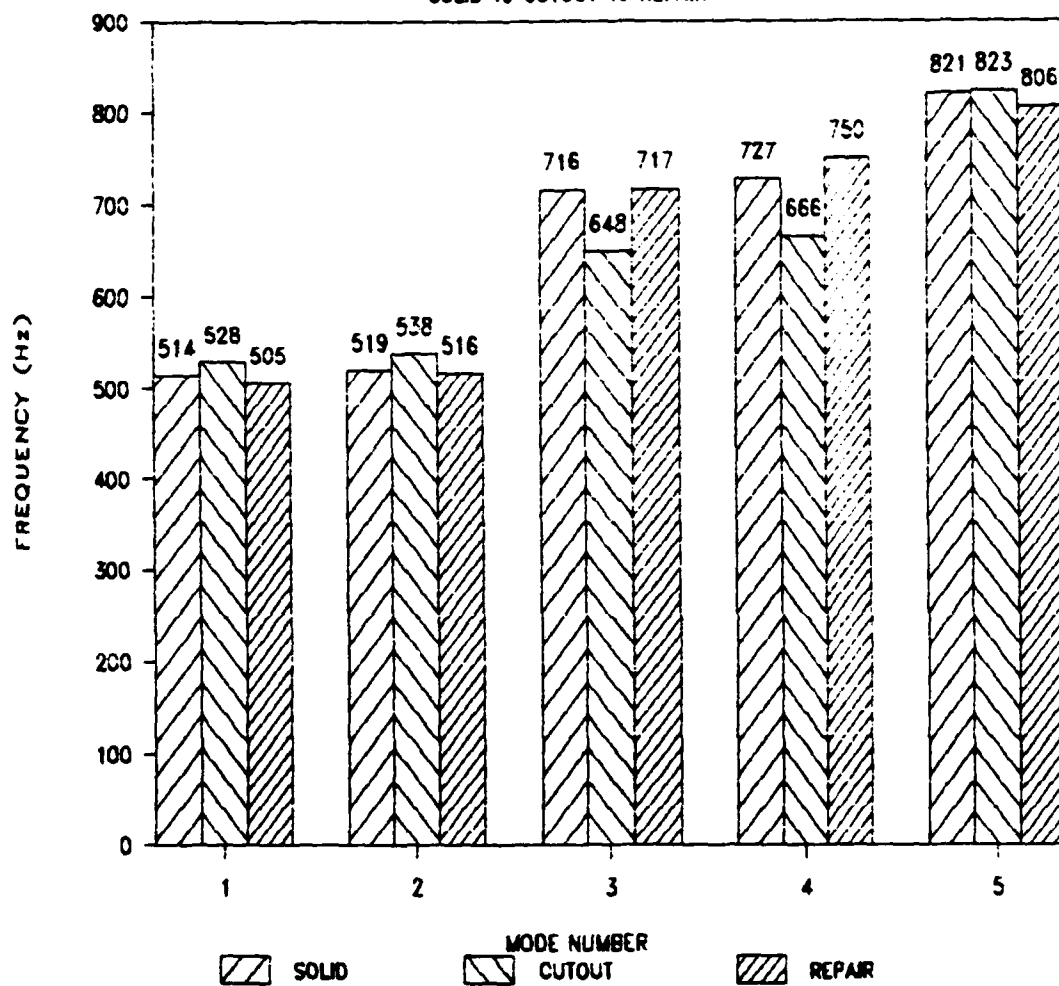


Figure 6.64. Summary of Repair Effect on -45° Cutout Panel

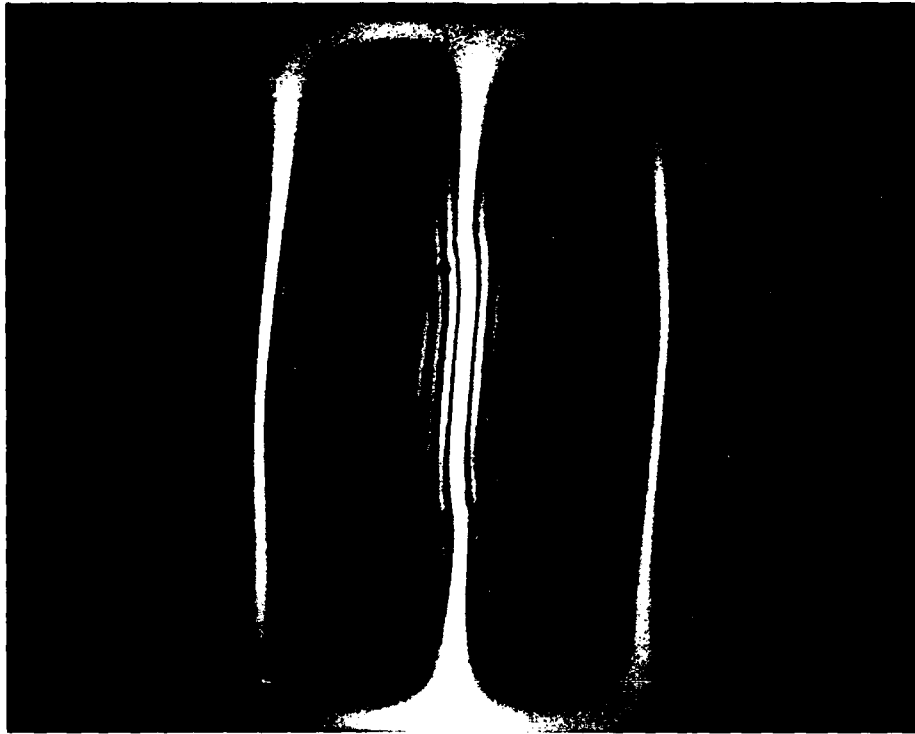


Figure 6.65. -45° Repaired Panel--Mode 1

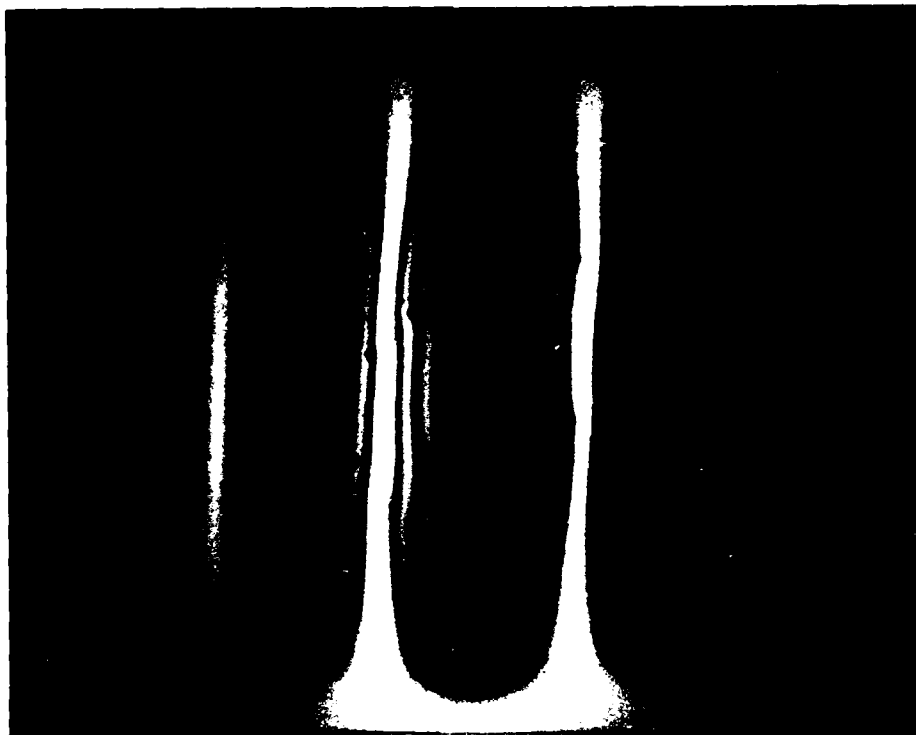


Figure 6.66. -45° Repaired Panel--Mode 2

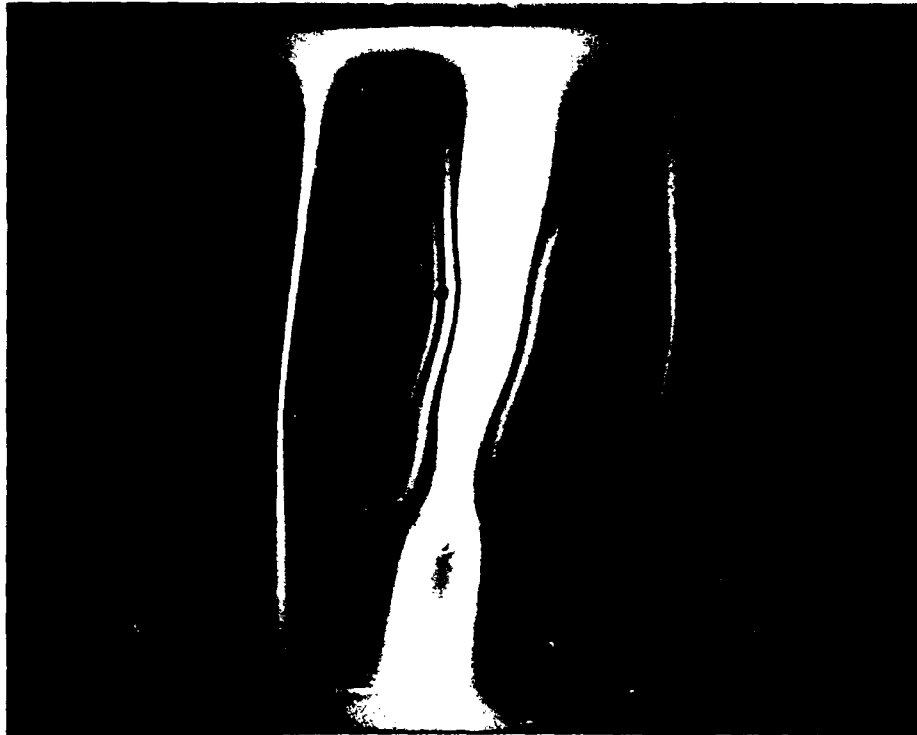


Figure 6.67. -45° Repaired Panel--Mode 3

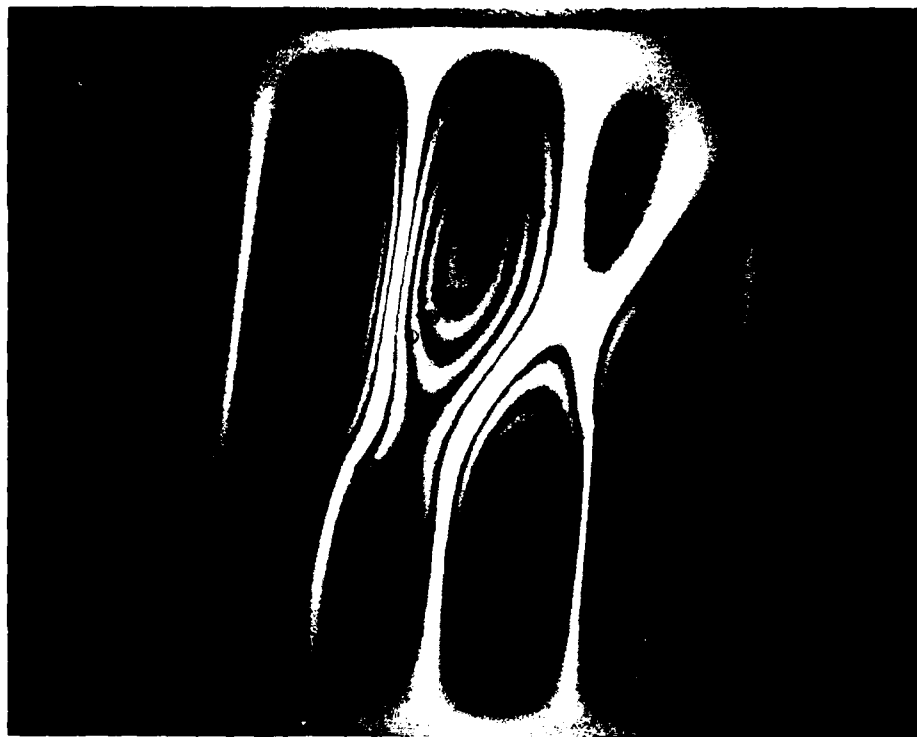


Figure 6.68. -45° Repaired Panel--Mode 4

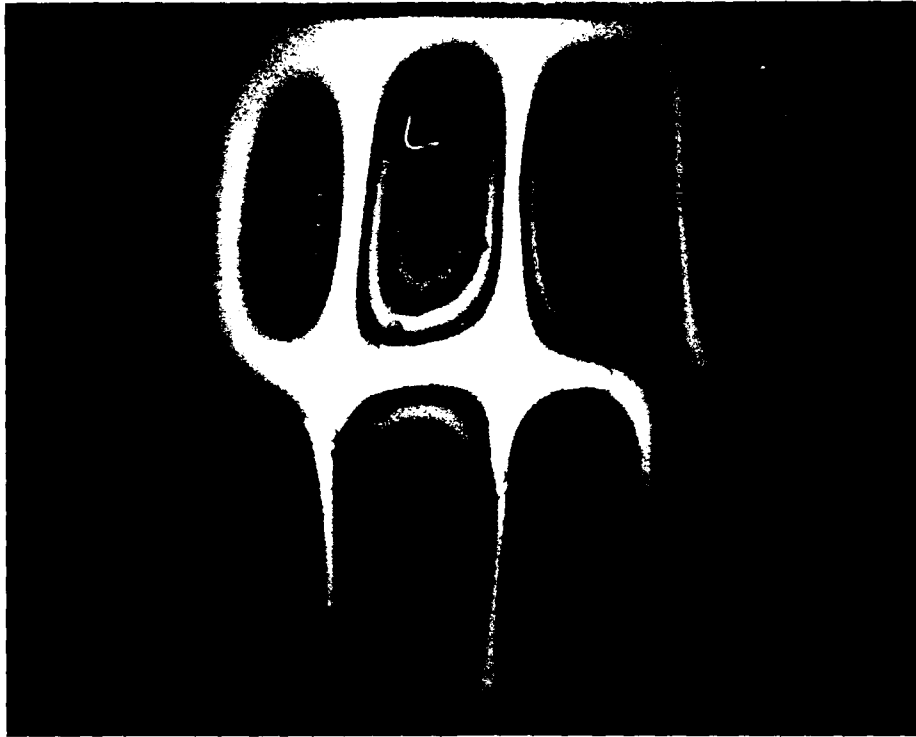


Figure 6.69. -45° Repaired Panel--Mode 5

### Repair Effects

This section summarizes the observations about the effects of the field repairs on the natural frequencies and mode shapes of the composite panels. Comparisons are made between each repaired panel and the corresponding cutout panel, and between each repaired panel and the solid panel. Emphasis is on the experimental results, with a brief summary of the NISA finite element predictions at the end.

It is important to recognize that the imperfect boundary conditions, the variables introduced by the unsophisticated field-type repairs, and the proximity of the natural

frequencies between pairs of adjacent modes made it difficult to identify any but the most general trends in the effects of repairs on the modal behavior of these panels. The most significant trends observed in the experimental phase concerned the behavior of the panels at the first two modes versus the behavior at the higher modes. In addition, the 0° and the 90° panels exhibited different trends, while the +45° and -45° panels showed significant similarities. In general, the modal behavior at the two lowest frequencies was dominated by the characteristics of the overall composite panel, while behavior at the higher frequencies showed increasing evidence of the effects of the aluminum patch and rivets.

Recalling, in a very simplified fashion, that the natural frequency of a structure is proportional to the square root of its stiffness while being inversely proportional to the square root of its mass, the relative effects of mass changes to stiffness changes were considered when trying to understand the behavior of the panels before and after they were repaired. The effects of the additional mass of the aluminum patch and rivets was independent of patch orientation, while the stiffness effects predictably appeared to be related to the orientation of the patch with respect to the more sensitive circumferential direction of the panel.

The frequency difference between the 0° repaired and the 0° cutout panel was negligible for the fundamental frequency, indicating that the mass and stiffness added to the cutout by the repair had equivalent effects on the behavior of the panel at this strongest asymmetric mode. This contrasted significantly with the 15% decrease from the fundamental frequency of the solid panel. This result indicated that the impact of the mass replaced by the patch greatly exceeded the impact of the stiffness that was replaced. This made sense when it was observed that the long axis of the patch was oriented away from the direction in which it would have had the greatest stiffening effect on the panel. It was noted that the two long lines of rivets coincided with the two major antinodes of the first mode. The additional mass along these critical regions tended to lower the frequency. In contrast, these two lines of rivets coincided with the two major node lines of the second mode. In this case, the impact of the additional mass was significantly reduced in comparison to the stiffness added by the patch.

The negligible difference between the fundamental frequency of the 90° repaired and the 90° unrepaired patch was the same as between the repaired panel and the original solid panel. This indicated that the orientation of the long axis of the patch along the circumferential direction

of the panel increased the stiffening effect of the patch, while the impact of the additional mass remained constant. Again, these effects were most consistent at the fundamental frequency and tended to become less predictable at the higher modes as the behavior was decreasingly dominated by overall panel behavior and increasingly influenced by localized behavior, such as that of the dissimilar patch material.

The behavior of the  $+45^\circ$  and  $-45^\circ$  panels was very similar with respect to patch effects. The frequencies of the  $+45^\circ$  and  $-45^\circ$  patched panels were very similar, within 5%, even at the higher modes. The mode shapes were very similar and reflect restoration of the modal behavior of the original solid panel. Frequency changes between these panels and the corresponding cutout panels, and between these panels and the solid panel, was small at the two lowest modes. Significant stiffening was apparent, though, when the patched panels were compared to the higher modes of the cutout panels. This reinforced the observation that the stiffening effect of the patches was more dominant at the higher modes where localized behavior was more influential on overall panel behavior.

The asymmetric versus symmetric nature of the various modal behaviors was considered. Since the patch was centered on the panel, the patch behaved differently, depending

on the nature of the overall panel modes. In the asymmetric modes, one end of the patch tried to displace outward, while the opposite end tried to displace inward, similar to a seesaw effect. The result was that the patch moved more as a rigid body within the panel. In the symmetric modes, however, where the center of the panel displaced opposite to the regions directly to either side of center, the patch behaved as a rigid body by moving in one direction with the panel, or it resisted rigid body motion as it tried to flex in the center. The expected effect was the localized stiffening in the higher modes, where the waves were shorter and did not span the entire patch. This was especially significant when the long axis of the patch was oriented circumferentially on the panel.

Finite element models of the 0° and 90° repaired panels were made using NISA. The limitations on mesh size restricted the accurate modeling of the rivet connections and overlap area. The resultant models resembled perfectly bonded patches more than they resembled mechanically fastened patches. The predictions for the 0° patched panel were consistent with the 10%-20% differences noted in the solid and cutout panels, except for the second mode, where the difference was only 1%. The predictions for the 90° patch are inconsistent, however, as they were within 2%-6% of the observed experimental results. While they are very

good results when considered alone, they are very questionable when considered with the trend established by the other sets of NISA results.

The effects of patch eccentricity were not obvious in the panel behavior. The nature of the mode shapes, which depicted behavior normal to the panel surface, did not reveal any significant changes due to the midsurface of the patch being offset from the midsurface of the panel by 0.036 inches.

Finally, it is significant to note that the mode shapes of the original solid panel were restored by the repair. The first three modes were consistently restored to resemble the first three modes of the solid panel. The higher-order modes were restored, but not necessarily in the same sequence. The most significant observation was that at the lower modes, the patch behaves as an integral part of the panel, while at the higher modes, patch characteristics began to influence the increasingly localized modal behavior.

#### NISA Analysis

The results of the finite element models were presented in the specific sections for each panel. The numerically determined natural frequencies and mode shapes were compared with their experimentally determined counterparts. The results are summarized in Table 6.10.

Table 6.10 NISA Results Summary  
 (% NISA differs from experimental result)

Panel	Mode Number			
	1	2	3	4
Solid	+9	+13	+11	+16
0° Cutout	+12	+15	+12	+11
90° Cutout	+13	+7	+12	+14
0° Repair	+12	-1	+10	+19
90° Repair	-2	+2	+6	+6

The natural frequencies of the solid, cutout, and 0° repaired panels were consistently high, with the noticeable exception of the second mode of the 0° repaired panel. The 90° repaired panel results were completely inconsistent with the other NISA predictions. The mode shape for the fundamental mode of each case was always accurate. In general, however, the other mode shapes were out of sequence.

The mode shapes predicted by NISA are presented along with the experimental results for each panel in previous sections of this chapter. They showed very little of the biasing effects that were present in the experimental results. This could be attributed to the perfect conditions modeled by the finite element code as compared to the imperfect conditions in the real panels. These imperfections could be caused by the boundary conditions imposed by the

test fixture, by minute irregularities in the panel material and geometry, and even by subtle inconsistencies in the way the panels were acoustically excited.

The shapes for the first two modes of the 90° cutout panel showed an interesting correlation with those observed experimentally. The actual panel displayed the previously discussed mode switching behavior. Unlike the other panels, this panel had a symmetric first mode and an asymmetric second mode. The NISA prediction for the first mode showed a tendency toward symmetry; however, it was not completely symmetric since the largest, strongest antinode was slightly right of center. Similarly, second mode also tended toward symmetry, with the dominant antinode slightly left of center. It was significant that these two modes were only 1 Hz apart, as opposed to the experimental results that were 27 Hz apart. The NISA predictions did not clearly separate the two modes, as evidenced by the close frequencies and very similar mode shapes. Thus, there was no dominant fundamental mode, as the usually symmetric second mode tried, but failed, to become first mode. As previously discussed, this unusual behavior occurred in the experimental results, where the symmetric mode actually became the fundamental mode for the 90° cutout.

The limitations of the PC version of NISA were largely imposed by the insufficient disk space to run a sufficiently

fine mesh. This was not, however, as significant a problem when using the isoparametric elements as it would be if the shell were approximated by a limited number of faceted quadrilateral plate elements as is done in STAGSC-1. The inclusion of transverse shear effects in the composite shell element could have artificially stiffened the model. Since the panels were extremely thin, with a thickness-to-radius ratio of 1:333, transverse shear effects should be negligible. In fact, the Kirchoff-Love hypothesis is usually invoked for such thin shells. The only composite element available in NISA does not use this hypothesis; rather, it includes transverse shear.

Cook cites problems that arise when isoparametric elements formulated to handle transverse shear are used to evaluate very thin plates and shells [6:263,283]. Numerical errors may arise when Gauss quadrature insufficiently handles through-the-thickness integration. Specifically, if the  $2 \times 2 \times 1$  rule is used to integrate the element stiffness matrix  $[k]$ , it may produce errors as the curvature of the element increases. This would account for the better agreement with Yen's composite flat plate results investigated in Appendix E; and for the slightly better results obtained for Monahan's isotropic flat plate versus the results for Soedel's isotropic cylindrical panel when using the general shell element.

Round-off error would be more significant in the PC version, where word size is smaller than on a mainframe computer. The large amount of numerical operations performed in solving an eigenvalue problem would rapidly compound the slightest round-off error made during each operation.

With respect to the models of the repaired panels, the limitations on mesh size restricted the accurate portrayal of the rivet connections and overlap area. The resulting models resembled perfectly bonded patches more than they resembled mechanically fastened patches. As mentioned before, the predictions for the 0° patched panel were consistent with the 10%-20% differences noted in the solid and cutout panels, except for the second mode where the difference was only 1%. The predictions for the 90° patch were inconsistent, however, as they were within 2%-6% of the observed experimental results. While they were very good results when considered alone, they were questionable when considered with the trend established by the other NISA results. Finally, the mode shapes for these models displayed very little evidence of the patch, once again indicative of the problem of mathematically portraying an imperfect subject with a perfect model. A much finer mesh would have to be achieved to better model the individual characteristics of the rivets, holes, and dissimilar patch. This concludes the detailed discussion of the experimental and numerical results. A summary of conclusions that were drawn from these results is presented in Chapter 7.

## VII. Conclusions

In summary, this thesis investigated the effects of simulated Aircraft Battle Damage Repairs on the natural frequencies and mode shapes of cylindrically curved, graphite/epoxy composite panels. An unsophisticated, field-level repair technique was developed and used to repair the various rectangular cutouts. Interferometric holography was used to experimentally determine the natural frequencies and mode shapes. An initial evaluation was made of the usefulness of the PC version of NISA in predicting the same natural frequencies and mode shapes.

A brief list of conclusions that can be drawn from the data and observations presented in this thesis includes:

1. Mechanically fastened patches of dissimilar material will alter the natural frequencies of composite panels. In general, the effect of additional mass introduced by a patch is independent of patch orientation, whereas the change in stiffness will be affected by patch orientation. A patch with its long axis in the circumferential direction of a cylindrical panel will introduce a greater stiffening effect.

2. The fastener region will have two significant effects. First, if the fasteners coincide with an antinode,

their mass will have a significant effect on lowering the natural frequency. If they coincide with a node, their mass will have a minimal effect. Second, the fastener region will be stiffer because the patch overlaps the composite, resulting in a region of thicker material.

3. The mode shapes of the original, undamaged panel will be recovered when the patch is applied. At the two lowest modes, the asymmetric fundamental mode and the symmetric second mode, the behavior of the total panel will dominate any patch effects. As the frequencies increase and panel behavior becomes more localized, the effects of the patch will dominate the adjacent regions of the panel, causing alterations in total panel behavior.

4. The NISA 3D Composite General Shell Element which takes into account transverse shear effects, artificially stiffens the model, resulting in natural frequencies that are too high in composite thin shell problems. The 3D Thin Shell (Discrete Kirchoff) Element and the 3D General Shell Element provide better accuracy for isotropic thin shell problems; however, they are not designed for anisotropic composite shell problems. The source of error in the 3D Composite General Shell Element is most likely related to the method with which it handles composite materials rather than with the way it handles thin cylindrical shells.

5. NISA accurately predicted the fundamental mode shape for all but the 90° cutout panel. It predicted mode shapes similar to the experimentally observed mode shapes for the next three modes; however, they were often out of sequence.

6. The PC version did not have sufficient memory to accurately model more complex shapes, such as the +45° and -45° cutout panels; to conduct a comprehensive convergence study; nor to accurately model the riveted patches.

### VIII. Recommendations for Further Study

1. Different gauge patches should be used to further study the mass versus stiffening effect of field-level repairs.
2. Different cutout sizes and shapes should be used to further study the effect of patch shape and orientation.
3. A similar study should be made of the effects of bonded field-level repairs, such as the RMX patch and the Philadelphia Box patch.
4. A similar study should be conducted using other boundary conditions, such as free or simply supported boundary conditions.
5. A similar study should be conducted using different ply layups and thicknesses to represent a wider variety of composite aircraft structures.
6. Other finite element codes, such as NASTRAN and STAGSC-1, should be used to determine how well they predict the effects of repairs on composite materials.
7. Additional detailed study of the NISA solution to a variety of well-known free vibration problems should be conducted to determine the limitations of the PC version for this type of analysis.

## BIBLIOGRAPHY

1. Ashwell, D.G., and R.H. Gallagher. Finite Elements for Thin Shells and Curved Members. London: John Wiley and Sons, Ltd., 1976.
2. Bert, Charles W. "Analysis of Shells," Structural Design and Analysis, Part I, edited by Lawrence J. Broutman and Richard H. Krock, Composite Materials, Volume 7, edited by C.C. Chamis. New York: Academic Press, Inc., 1975.
3. Bohlmann, R.E., and others. "Bolted Field Repair of Graphite/Epoxy Wing Skin Laminates," Joining of Composite Materials, ASTM STP749, edited by K.T. Kedward, American Society for Testing and Materials, 1981, pp. 97-116.
4. Calcote, Lee R. The Analysis of Laminated Composite Structures. New York: Van Nostrand Reinhold Company, 1969.
5. Caulfield, Henry J., and Sun Lu. The Applications of Holography. New York: Wiley-Interscience, 1970.
6. Cook, Robert D. Concepts and Applications of Finite Element Analysis (Second Edition). New York: John Wiley and Sons, 1981.
7. Cyr, Capt Garry J. Effects of Cutout Orientation on Natural Frequencies and Mode Shapes of Curved Rectangular Composite Panels. Master's Thesis, AFIT/GAE/AA/86D-3. School of Engineering, Air Force Institute of Technology, (AU), Wright-Patterson Air Force Base, Ohio, December 1986.
8. Department of the Air Force. F-16A ABDR Procedures Manual. TO 1F-16A-39. Washington: HQ USAF.
9. Department of Defense. Military Standardization Handbook: Metallic Materials and Elements for Aerospace Vehicle Structures. MIL-HDBK-5D. Washington: DOD, 1 June 1983.
10. Dominguez, J. Design and Test of Rapid Repair of Large Area Damage of Graphite/Epoxy Structure: Final Report, September 1985-October 1986. Project No. RR22-F14. Warminster, Pennsylvania: Naval Air Development Center, February 1987 (AD-B116 474).

11. Engineering Mechanics Research Corporation. NISA User's Manual (Numerically Integrated Elements for System Analysis) (Release 86.6). Troy, Michigan, 1986.
12. Hinkle, T., and J. Van Es. Battle Damage Repair of Composite Structures: Final Report, February 1984-June 1987. AFWAL TR-87-3104. Contract F33615-83-C-3246. St. Louis, Missouri: McDonnell Aircraft Company, March 1988.
13. Hoehn, George, and Charles Ramsey. "Test Verification of Improvements to Bolted Repair Design Methodology," Proceedings of the Second DOD/NASA Composite Repair Technology Workshop. 339-360. San Diego, California, 4-6 November 1986.
14. Hoskin, Brian C., and Alan A. Baker, eds. Composite Materials for Aircraft Structures. New York: American Institute of Aeronautics and Astronautics, Inc., 1986.
15. Irons, Bruce M. "A Frontal Solution Program for Finite Element Analysis," International Journal for Numerical Methods in Engineering, 2-1: 5-32 (January-March 1970).
16. Jones Robert M. Mechanics of Composite Materials. New York: Hemisphere Publishing Corporation, 1975.
17. Jones, Robert M., and Harold S. Morgan. "Buckling and Vibration of Cross-Ply Laminated Circular Cylindrical Shells," Proceedings of the AIAA 12th Aerospace Sciences Meeting. Paper No. 74-33. New York: American Institute of Aeronautics and Astronautics, January 1974.
18. Kock, Winston E. Lasers and Holography, and Introduction to Coherent Optics. New York: Dover Publications, Inc., 1981.
19. Maddux, Gene, Engineer, Flight Dynamics Laboratory, Wright-Patterson Air Force Base, Ohio. Personal interviews, 3 March-4 November 1988.
20. Martin, W. Advance Filed Level Repair Materials Technology for Composite Structures: Final Report, February 1984-June 1987. AFWAL-TR-87-4109. Contract F33615-84-C-5307. Hawthorne, California: Northrop Corporation, October 1987.

21. Meirovitch, Leonard. Analytical Methods in Vibrations. New York: MacMillan Publishing Co., Inc., 1967.
22. ----- . Elements of Vibrations Analysis (Second Edition). New York: McGraw-Hill Book Company, 1986.
23. Mindlin, R.D. "Influence of Rotatory Inertia and Shear on Flexural Motions of Isotropic, Elastic Plates," Journal of Applied Mechanics, 18: 31-38 (March 1951).
24. Monahan, 1st Lt Jon. Natural Frequencies and Mode Shapes of Plates with Interior Cut-Outs. Master's Thesis, AFIT/GAM/MC/71-1. School of Engineering, Air Force Institute of Technology (AU), Wright-Patterson Air Force Base, Ohio, September 1970.
25. Myhre, Herbert S., and others. Advanced Composite Repair Guide: Final Report, July 1979-January 1982. AFWAL-TR-83-3092. Contract F33615-79-C3217. Hawthorne, California: Northrop Corporation, March 1983 (AD-8077 732).
26. Newport Corporation. Operator's Manual for HC-300 Holographic Recording Device. Fountain Valley, California.
27. Otz, G.E., and R.E. Bohlmann. McDonnell Aircraft Company. Damage Tolerance and Repair of Forward Fuselage Structure: Final Report, 18 May 1981-24 February 1984. Contract N00019-80-G-101. St. Louis, Missouri: McDonnell Aircraft Company, September 1984 (AD-B095 241).
28. Palazotto, Anthony N. Class handouts distributed in MECH 741, Advanced Topics in Composite Materials. School of Engineering, Air Force Institute of Technology, (AU), Wright-Patterson Air Force Base, Ohio, April 1988.
29. Rajamani, A., and R. Prabhakaran. "Dynamic Response of Composite Plates with Cut-Outs, Part II: Clamped-Clamped Plates," Journal of Sound and Vibration, 54-4: 565-576 (22 October 1977).
30. Reddy, J.N., and C.F. Liu. "A Higher Order Shear Deformation Theory of Laminated Elastic Shells," International Journal of Engineering Science 23, No. 3: 319-330 (1985).

31. ----- . "Stability and Vibration of Isotropic, Orthotropic and Laminated Plates According to a Higher-Order Shear Deformation Theory," Journal of Sound and Vibration, 98: 157-170 (1985).
32. Reissner, Eric. "The Effect of Shear Deformation on the Bending of Elastic Plates," Journal of Applied Mechanics, 12: A69-A77 (March 1945).
33. Saada, Adel S. Elasticity Theory and Applications. Malabar, Florida: Robert E. Krieger Publishing Company, 1987.
34. Sanders, A.L., and others. Rapid Repair of Battle Damaged Aircraft Structure: Final Report, September 1980-January 1984. AFWAL-TR-84-3034. Contract F33615-80-C-3235. Los Angeles: Rockwell International Corporation, May 1985.
35. Soedel, Werner. Vibrations of Plates and Shells. New York: Marcel Dekker, Inc., 1981.
36. Stetson, Karl A. "Holographic Vibration Analysis," Holographic Nondestructive Testing, edited by Robert K. Erf. New York: Academic Press, 1974.
37. Stone, Robert H. "Development of Field Level Repairs for Composite Structures," The Repair of Aircraft Structures Involving Composite Materials. AGARD Conference Proceedings No. 402, NATO Advisory Group for Aerospace Research and Development. Loughton, England: Specialised Printing Services Limited, October 1986.
38. Tisler, T.A. Collapse Analysis of Cylindrical Composite Panels with Large Cutouts Under Axial Loads. Master's Thesis, AFIT/GAE/AA/86D-18. School of Engineering, Air Force Institute of Technology (AU), Wright-Patterson Air Force Base, Ohio, December 1986.
39. Ugural, A.C. Stresses in Plates and Shells. New York: McGraw-Hill Book Company, 1981.
40. Unterseher, Fred, and others. Holography Handbook. Berkeley, California: Ross Books, 1982.
41. Van Es, J. "Battle Damage Repair of Composites," Proceedings of the Second DOD/NASA Composite Repair Technology Workshop. 361-376. San Diego, California, 4-6 November 1986.

42. Walley, Capt Richard A. Natural Frequencies and Mode Shapes of Curved Composite Panels with Interior Cutouts. Master's Thesis, AFIT/GAE/AA/85D-16. School of Engineering, Air Force Institute of Technology, (AU), Wright-Patterson Air Force Base, Ohio, December 1985 (AD-A165 269).
43. Waters, James P. "Holography," Holographic Nondestructive Testing, edited by Robert K. Erf. New York: Academic Press, 1974.
44. -----. "Interferometric Holography," Holographic Nondestructive Testing, edited by Robert K. Erf. New York: Academic Press, 1974.
45. Wentworth, Stanley E., and Michael S. Sennett. "Unconventional Approaches to Field Repair," The Repair of Aircraft Structures Involving Composite Materials. AGARD Conference Proceedings No. 402, NATO Advisory Group for Aerospace Research and Development. Loughton, England: Specialised Printing Services Limited, October 1986.
46. Whitney, J.M. "The Effect of Transverse Shear Deformation on the Bending of Laminated Plates," Journal of Composite Materials, 3: 534-547 (July 1969).
47. Whitney, J.M., and C.T. Sun. "A Higher Order Theory for Extensional Motion of Laminated Anisotropic Shells and Plates," Journal of Sound and Vibration, 30: 85 (1973).
48. -----. "A Refined Theory for Laminated Anisotropic Cylindrical Shells," Journal of Applied Mechanics, 41: 47 (1974).
49. Yen, S.C., and F.M. Cunningham. "Vibration Characteristics of Graphite-Epoxy Composite Plates," Proceedings of the 1985 SEM Spring Conference on Experimental Mechanics. 60-67. Brookfield Center, Connecticut: Society for Experimental Mechanics, 1985.
50. Zienkiewicz, O.C. The Finite Element Method in Engineering Science. London: McGraw-Hill Publishing Company Limited, 1971.

Appendix A: Holography Test Equipment

The following is a list of the equipment used in conducting the interferometric holography experiments during this thesis.

Atlas Sound Horn (2 ea)  
60 Watts

Bogen MOS-FET High-Performance Power Amplifier  
Model HTA-125

Coherent Radiation Laboratories Power Meter  
Model 202; S/N 118

Hewlett-Packard Function Generator  
Model 3310B; S/N 1201A06275

Hewlett-Packart Universal Counter  
Model 5316A; S/N 2308A04211

JVC Color Video Camera  
Model GX-S700; S/N 06120234

Newport Research Corporation Beam Splitter  
Model 960A

Newport Research Corporation Holographic Camera  
Model HC 310; S/N 7090034

Newport Research Corporation Holographic Camera  
Controller  
Model HC320; S/N 7090034

Newport Research Corporation Mirror  
Model 630A-2

Newport Research Corporation Shutter  
Model 884

Newport Research Corporation Spatial Filter (2 ea)  
Model 900

Newport Research Corporation Universal Shutter System  
Model 880; S/N 1154.1121

Panasonic Recorder-Reproducer  
Model AG-2200; S/N A6HF00721

Sharp Newvicon Color Video Camera  
Model QC-54; S/N 264978

Sony Trinitron Color Receiver/Monitor  
Model CVM-1250; S/N 012115

Spectra-Physics Exciter  
Model 261; S/N 3110390

Spectra-Physics Laser  
Model 125A; S/N 3610621

Spectra-Physics Power Meter  
Model 401C; S/N 1627

Tektronix Dual Trace Amplifier (2 ea)  
S/N 116125  
S/N B086362

Tektronix Oscilloscope  
Model 7603

## Appendix B: Holography Procedure with NRC HC-300 System

Holography procedures vary with the type of holography and the system and setup being used. The following steps were developed for using the NRC HC-300 Thermoplastic Holography System. The basic setup is the same as for the traditional wet chemical process. The essential differences are in the much-simplified procedures for making the holographic recording.

1. CAUTION: A laser eye exam is required before using the laser for the first time. In addition, instruction in the setup, care, and use of the laser should be received prior to the first use to prevent personal injury or equipment damage.

2. All mirrors and lenses must be clean. Dirt, dust, and scratches will severely degrade the quality of the laser light and, consequently, the quality of the holograms. Optical equipment should be treated with extreme care. Cover the items when not in use. If cleaning is necessary, acetone or a similar cleaning fluid should be dripped lightly onto the optical surface and then gently wiped with lens tissue to absorb the fluid and dust. Mirrors and lenses should not be rubbed.

3. The air table must be charge so that the table is "floating," or isolated from vibrations in the room and building. Also, a source of clean, dry compressed air at 5 to 10 psi must be connected through the HC-300 Controller Unit to the HC-300 Camera Unit.

4. Turn on the laser with the toggle switch on the Spectra-Physics Exciter. The laser has a 15-30 minute warm-up period, during which time no adjustments should be made to the laser.

5. After the laser is warmed up, turn on the NRC Universal Shutter System. Set it to the manual position and trigger the shutter to the open position so that the laser beam passes through the shutter opening.

6. Place the Spectra-Physics Power Meter in the laser beam path after the shutter. Setting the sensitivity scale to 100 mW, read the laser power output on the scale. The output should be 50+ mW. If the power level is less than 50 mW, then laser alignment should be checked and adjusted for optimum output. If it is still below 50 mW, then cleaning is necessary, after which alignment will have to be rechecked and readjusted.

7. Once the laser is providing 50+ mW, remove the Power Meter. Next, the ratio of the intensity of the reference

beam to the object beam must be measured at the position where the beams will interfere at the thermoplastic plate. The Coherent Radiation Laboratories Power Meter (borrowed from the Flight Dynamics Lab) or a similar instrument is used for this. The desired ratio for thermoplastic holograms is 10:1, in accordance with the HC-300 Operator's Manual. The adjustment of this ratio is an iterative process, with the ratio being adjusted with the variable beam splitter. First, block off the reference beam and note the intensity of the object beam measured at the thermoplastic plate position. Next, block off only the object beam and observe the intensity of the reference beam at the same location. If the ratio is not 10:1, make adjustments with the beam splitter, noting the setting on the scale around the circumference of the instrument. Repeat the intensity readings as before and make further adjustments until the desired ratio is attained.

8. After the light intensities are correct, remove the Power Meter and turn off the shutter. Set it to automatic mode and pre-select a ten-second exposure time for real-time holograms. This exposure time may be varied according to the intensity of the light and the quality of the resulting holograms. Ten seconds worked well for real-time holograms in this thesis, while a five-second exposure time resulted in high quality time-average holograms.

9. Insert a thermoplastic plate into the camera mount in accordance with the operator's manual. With all lights, to include the laser beam, turned off, press the "Erase" button on the HC-300 controller Unit. A light inside the Camera Unit will illuminate and heat the thermoplastic plate to erase any images already on it by softening the thermoplastic material. When the light goes out, air is forced over the plate to cool it. Next, the high-voltage coronatron rises from the Camera Unit and charges the plate. When this is complete, the "Expose" button and then the "Busy" button will illuminate. This signals that the plate is prepared to make a new recording. At this time, activate the shutter to automatically expose the plate for 10 seconds. When the exposure time is complete and the laser beam has been turned off, press the "Busy" button to activate the develop cycle that takes about 10 to 15 seconds. When this is complete, the "Erase" button illuminates to indicate that the hologram recording cycle is complete and the system is prepared to make the next hologram. If the "Fault" light comes on, a good quality hologram has not been made. The operator's manual describes the corrective actions necessary to overcome this problem.

10. If the "Fault" light did not illuminate, then the thermoplastic plate should have captured an image of the

object--a hologram. The hologram can be seen by triggering the shutter in the manual mode and peering "through" the plate to observe the image that is now reconstructed by the interference of the reference beam.

11. At this point, the experimental procedures described in Chapter IV can be followed to determine natural frequencies and mode shapes with real-time holograms and to record specific modes with time-average holograms. Note that a photograph must be taken of the time-average hologram with the plate mounted in the HC-300 Camera Unit before that specific plate can be erased to make another hologram on it. The limitation is the number of thermoplastic plates that are available for recording and storing a series of mode shapes. The Tech Photo Lab provided the specialized support needed for obtaining good quality photographs of the time-average holograms.

Appendix C: Sample NISA Input File

The following is the input file used to model the solid panel by taking advantage of the symmetry and modeling only the bottom half of the panel. Comments about selected lines are included to the right.

```
**CH12.I                                     (Input file name)
**THESIS -- Composite Half Panel (Solid)
ANALYSIS = EIGENVALUE
FILE NAME = C:CH12
SAVE FILE = 26,27
WARN = GO
EXEC = CGO
RESEQUENCE = ON
AUTO = ON          (Rotation constrained about shell normal)
ELEMENT ECHO = ON
NODE ECHO = ON
EIGEN EXTRACTION = SUBSPACE,CONVENTIONAL
MASS FORMULATION = CONSISTENT
DEBUG = ON

*A1      TITLE
COMPOSITE CURVED SOLID PANEL (12x06; 2d order)

*C1      ELEMENT TYPE
1, 32, 2      (8-Noded Composite General Shell Element)

*D1      REAL CONSTANTS                       (Ply Thickness)
**REAL CONSTANT TABLE NO. 1
1, 8
0.005////////

*D2      LAMINATE ORIENTATION (Fiber angles wrt structural axis)
** ROTATION ANGLES TABLE NO. 1
1, 8
90.00////////
** ROTATION ANGLES TABLE NO. 2
2, 8
45.00////////
** ROTATION ANGLES TABLE NO. 3
3, 8
-45.00////////
** ROTATION ANGLES TABLE NO. 4
4, 8
0.00////////

*D3      LAMINA SEQUENCE                     (Describes each ply)
** COMPOSITE SHELL LAMINATION SEQUENCE DATA, TABLE NO. 1
8,0, 1,1,1,1,1,1,1,1, 1,2,3,4,4,3,2,1, 1,1,
1,1,1,1,1,1
```

```

*E1      ELEMENT DEFINITION
$ $      -6, 50, 12, 2
1,       1, 2, 3, 28, 53, 52, 51, 26, 1,1,1,12,2,1,2

*F1      NODAL COORDINATES
-25, 1, 25, 25, 0.00, 0.00, 0.50, 1 (Cylindrical
                                         coordinates)
1 $      12.00 -29.09551303, 0.00, 1
25, 1, 1, 0, 12.00 29.09551303, 0.00, 1

*H1      MATERIAL PROPERTIES TABLE
EX ,     1, 0, .1884E8
EY ,     1, 0, .1468E7
NUXY,    1, 0, .2799E0
GXY ,    1, 0, .9099E6
GXZ ,    1, 0, .9099E6
GYZ ,    1, 0, .72792E6
DENS,    1, 0, .1516227E-3

*12      EIGENVALUE ANALYSIS CONTROL
4, 0, 50, 0, 0.0, 0.0, 1.0E-5, 0.0

*13      OUTPUT CONTROL
0, 0, 0,, -1, 0, 1

*J1      BOUNDARY CONDITIONS
1, UX, 0.0, 25, 1, UY, UZ, ROTX, ROTY, ROTZ (Clamped)
26, UX, 0.0, 301, 25, UY, UZ, ROTX, ROTY, ROTZ (Clamped)
50, UX, 0.0, 325, 25, UY, UZ, ROTX, ROTY, ROTZ (Clamped)
302, UZ, 0.0, 324, 1, ROTX, ROTY (Axis of symmetry)

*P1      MODE SELECTION FOR OUTPUT
1,1,1,1

*Z1      DATA DECK TERMINATOR

```

## Appendix D: NISA Element Formulation

This appendix summarizes the formulation of an isoparametric shell element like the NISA 3D Laminated Composite General Shell Element, NKTP 32, used to analyze the composite panels tested in this thesis. The 3D General Shell Element, NKTP 20, follows a similar formulation while the 3D Thin Shell (Kirchoff Discrete) Element, NKTP 40, has a different formulation that will not be discussed here. Each of these elements was used in the preliminary NISA study described in Appendix E. The summary that follows is from the formulations presented by Cook [6] and Zienkiewicz [50].

NISA uses isoparametric elements to model composite shells. These elements can model curved shapes and can have more nodes, thereby better representing the geometry of a curved shell and allowing increased degrees of freedom in a model without increasing the number of elements. The nodes describe the geometry of an element by defining the global coordinates,  $\{x, y, z\}$ , in terms of nodal coordinates  $\{\bar{c}\}$  such that  $\{x, y, z\} = [\bar{N}']\{\bar{c}\}$ . Similarly, these nodes describe the displacement  $\{u, v, w\}$  of discrete points in terms of nodal degrees of freedom  $\{\bar{d}\}$  such that  $\{u, v, w\} = [\bar{N}]\{\bar{d}\}$ . The interpolation, or shape, functions  $[\bar{N}]$  and  $[\bar{N}']$  are functions of a natural coordinate system,  $\{\xi, \eta, \zeta\}$ . An element is isoparametric when  $[\bar{N}]$  and  $[\bar{N}']$  are identical. These

functions guarantee  $C_0$  continuity in the distorted elements as long as displacement continuity is preserved in the parent element defined by the natural coordinates and a one-to-one relationship exists between the natural coordinates and the global coordinates defining an element.

The NKTP 32 element used in this thesis was an eight-noded element with the natural coordinate system shown in Figure D.1. This element is essentially a compromise between a flat quadrilateral element and a solid element. It accounts for transverse shear deformation to handle thick shells, yet is designed to model thin shells as well.

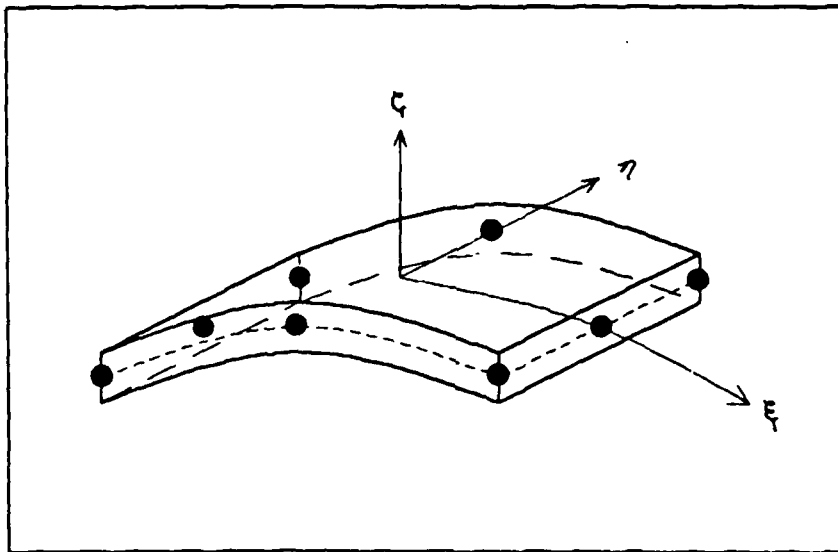


Figure D.1. NKTP 32 Element Natural Coordinate System

The formulation starts with a solid element. Subscripts p and q indicate coordinates on the  $\zeta = -1$  and  $\zeta = +1$  surfaces, respectively; and  $i = 1, \dots, 8$ . The geometry of the element is defined by

$$\begin{Bmatrix} x \\ y \\ z \end{Bmatrix} = \sum N_i \frac{1-\zeta}{2} \begin{Bmatrix} x_{ip} \\ y_{ip} \\ z_{ip} \end{Bmatrix} + \sum N_i \frac{1+\zeta}{2} \begin{Bmatrix} x_{iq} \\ y_{iq} \\ z_{iq} \end{Bmatrix} \quad (D.1)$$

where the shape functions,  $N_i$ , are functions of  $\zeta$  and  $\eta$  only.

Now, since NKTP 32 element has nodes only on the midsurface, the nodal coordinates for this element are

$$\{x_i \ y_i \ z_i\} = (\{x_{ip} \ y_{ip} \ z_{ip}\} + \{x_{iq} \ y_{iq} \ z_{iq}\})/2 \quad (D.2)$$

To account for element thickness,  $t_i$ , a vector  $\bar{C}_i$  normal to the midsurface and spanning  $t_i$  is defined as

$$\bar{C}_i = \{x_{iq} \ y_{iq} \ z_{iq}\} - \{x_{ip} \ y_{ip} \ z_{ip}\} \quad (D.3)$$

$\bar{C}_i$  is depicted in Figure D.2. Note that  $|\bar{C}_i| = t_i$ . (D.4)

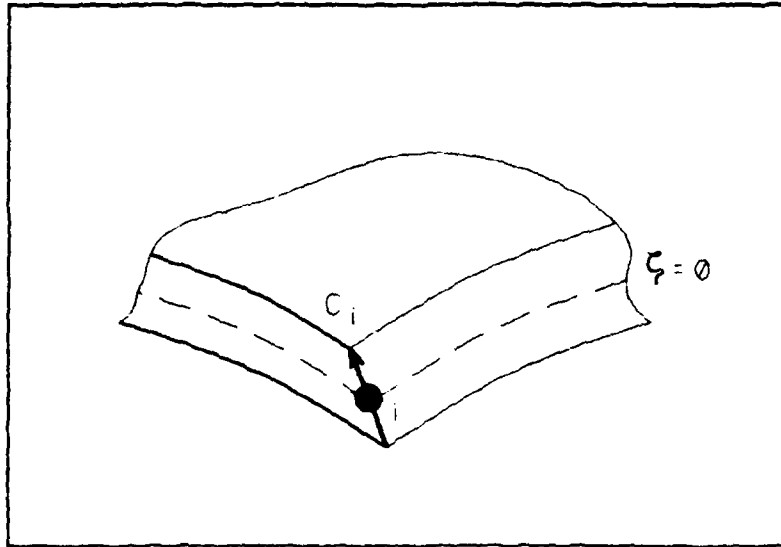


Figure D.2. Thickness Vector  $\bar{C}_i$

Substituting Equations D.2 and D.3 into D.1 yields the following expression for element geometry

$$\{x \ y \ z\} = N_i \{u_i \ v_i \ w_i\} + N_i \frac{z}{2} \bar{C}_i \quad (D.4)$$

The displacement field is given by

$$\begin{Bmatrix} u \\ v \\ w \end{Bmatrix} = \sum N_i \begin{Bmatrix} u_i \\ v_i \\ w_i \end{Bmatrix} + \sum N_i z \frac{t_i}{2} [\bar{u}_i] \begin{Bmatrix} \alpha_i \\ \beta_i \end{Bmatrix} \quad (D.5)$$

where the first term is the contribution of the displacement degrees of freedoms,  $u_i$ ,  $v_i$ , and  $w_i$ ; and the second term is

the contribution of the rotational degrees of freedom,  $\alpha_i$  and  $\beta_i$ , as shown in Figure D.3.

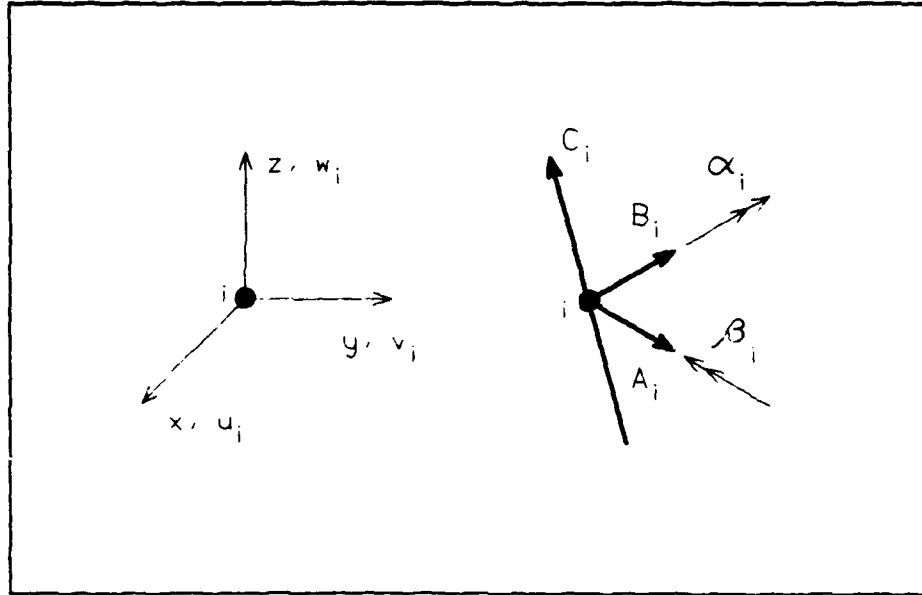


Figure D.3. Displacement and Rotation Degrees of Freedom

Small rotations,  $\alpha_i$  and  $\beta_i$ , cause displacements given by  $u'_i$  and  $v'_i$  such that

$$u'_i = (\zeta t_i/2) \alpha_i \quad \text{and} \quad v'_i = (\zeta t_i/2) \beta_i \quad (\text{D.6})$$

These displacements are transformed into global displacement components by the direction cosine matrix

$$[\bar{u}_i] = \begin{bmatrix} l_{Ai} & l_{Bi} \\ m_{Ai} & m_{Bi} \\ n_{Ai} & n_{Bi} \end{bmatrix} \quad (\text{D.7})$$

where

$$\{l_{Ai} \ m_{Ai} \ n_{Ai}\} = \bar{A}_i/A_i \quad \text{and} \quad \{l_{Bi} \ m_{Bi} \ n_{Bi}\} = \bar{B}_i/B_i \quad (D.8)$$

such that

$$\begin{Bmatrix} u_i \\ v_i \\ w_i \end{Bmatrix}_{\alpha\beta} = [\bar{u}_i] \begin{Bmatrix} u'_i \\ v'_i \end{Bmatrix} \quad (D.9)$$

Thus, total displacement of a point in the element is given by

$$\{u \ v \ w\} = \sum N_i (\{u_i \ v_i \ w_i\} + \{u_i \ v_i \ w_i\}_{\alpha\beta}) \quad (D.10)$$

After identifying the geometry given by Equation D.4 and the displacement field given by Equation D.10, strain-displacement relations are established. For a solid shell element

$$\{e_x \ e_y \ e_z \ \gamma_{xy} \ \gamma_{yz} \ \gamma_{zx}\} = [\bar{H}] \{u_{,x} \ u_{,y} \ u_{,z} \ \dots \ w_{,z}\} \quad (D.11)$$

where the subscript ,i indicates the partial derivative with respect to i, and  $[\bar{H}]$  is

$$[\bar{H}] = \begin{bmatrix} 1 & 0 & 0 & 0 & 0 & 0 & 0 & 0 & 0 \\ 0 & 0 & 0 & 0 & 1 & 0 & 0 & 0 & 0 \\ 1 & 0 & 0 & 0 & 0 & 0 & 0 & 0 & 1 \\ 0 & 1 & 0 & 1 & 0 & 0 & 0 & 0 & 0 \\ 0 & 0 & 0 & 0 & 0 & 1 & 0 & 1 & 0 \\ 0 & 0 & 1 & 0 & 0 & 0 & 1 & 0 & 0 \end{bmatrix} \quad (D.12)$$

and

$$\{u, x, u, y, \dots, w, z\} = [\bar{\Gamma}\bar{\Gamma}\bar{\Gamma}]\{u, u, \dots, w, \} \quad (D.13)$$

where  $\bar{\Gamma}$  is the inverse of the Jacobian  $[\bar{J}]$ ,

$$[\bar{J}] = \begin{bmatrix} x, \xi & y, \xi & z, \xi \\ x, \eta & y, \eta & z, \eta \\ x, \zeta & y, \zeta & z, \zeta \end{bmatrix} \quad (D.14)$$

Now Equation D.5 can be written

$$\begin{Bmatrix} u, \xi \\ u, \eta \\ u, \zeta \end{Bmatrix} = \sum \begin{bmatrix} \bar{N}_{i, \xi} & 0 & 0 \\ N_{i, \eta} & 0 & 0 \\ 0 & 0 & 0 \end{bmatrix} \begin{Bmatrix} u_i \\ y_i \\ z_i \end{Bmatrix} +$$

$$\sum \frac{t_i}{2} \begin{bmatrix} \zeta N_{i, \xi} & 0 & 0 \\ \zeta N_{i, \eta} & 0 & 0 \\ N_i & 0 & 0 \end{bmatrix} [\bar{u}_i] \begin{Bmatrix} \alpha_i \\ \beta_i \end{Bmatrix} \quad (D.15)$$

$$\begin{Bmatrix} v, \xi \\ v, \eta \\ v, \zeta \end{Bmatrix} = \sum \begin{bmatrix} 0 & N_{i, \xi} & 0 \\ 0 & N_{i, \eta} & 0 \\ 0 & 0 & 0 \end{bmatrix} \begin{Bmatrix} u_i \\ y_i \\ z_i \end{Bmatrix} +$$

$$\sum \frac{t_i}{2} \begin{bmatrix} 0 & \zeta N_{i, \xi} & 0 \\ 0 & \zeta N_{i, \eta} & 0 \\ 0 & N_i & 0 \end{bmatrix} [\bar{u}_i] \begin{Bmatrix} \alpha_i \\ \beta_i \end{Bmatrix} \quad (D.16)$$

$$\begin{Bmatrix} w, \xi \\ w, \eta \\ w, \zeta \end{Bmatrix} = \sum \begin{bmatrix} 0 & 0 & N_{i, \xi} \\ 0 & 0 & N_{i, \eta} \\ 0 & 0 & 0 \end{bmatrix} \begin{Bmatrix} u_i \\ y_i \\ z_i \end{Bmatrix} + \\
 \sum \frac{t_i}{2} \begin{bmatrix} 0 & 0 & \zeta N_{i, \xi} \\ 0 & 0 & \zeta N_{i, \eta} \\ 0 & 0 & N_i \end{bmatrix} [\bar{u}_i] \begin{Bmatrix} \alpha_i \\ \beta_i \end{Bmatrix} \quad (D.17)$$

Combining Equations D.11 through D.17, the strain-displacement equation becomes

$$\{e_x \ e_y \ e_z \ \gamma_{xy} \ \gamma_{yz} \ \gamma_{zx}\} = [\bar{B}_i] \{u_i \ v_i \ w_i \ \alpha_i \ \beta_i\} \quad (D.18)$$

where  $[\bar{B}_i]$  is a 6 x 5 matrix relating strain to displacement. The complete strain-displacement matrix  $[\bar{B}]$  is made up of a  $[\bar{B}_i]$  matrix for each node. Thus, it will be a 48 x 40 matrix for the eight-noded NKTP 32 element.

The stiffness matrix for this element can now be defined as

$$[\bar{k}] = \int_V [\bar{B}]^T [\bar{E}] [\bar{B}] dV \quad (D.19)$$

recalling from Chapter II that, for a laminated composite, the material stiffness matrix  $[\bar{E}]$  is composed of extensional terms,  $[A]$ , extensional-bending coupling terms,  $[B]$ , and bending terms,  $[D]$ , such that it is written

$$\begin{bmatrix} & : & \\ A & : & B \\ & : & \\ \hline & : & \\ B & : & D \\ & : & \end{bmatrix}$$

Applying the determinant  $J$  of the Jacobian matrix  $[\bar{J}]$  to integrate Equation D.19, the element stiffness matrix becomes

$$[\bar{k}] = \int_{-1}^1 \int_{-1}^1 \int_{-1}^1 [\bar{B}]^T [\bar{E}] [\bar{B}] J d\xi d\eta d\zeta \quad (D.20)$$

When the thickness-to-radius ratio is small, the  $\zeta$  terms in  $[\bar{J}]$  can be neglected, resulting in  $[\bar{J}]$  as a function of  $\xi$  and  $\eta$  only. Then separating strain-displacement matrix  $[\bar{B}]$  (not the composite material extensional-bending matrix) into an extensional part,  $[\bar{B}_0]$ , and a bending part,  $[\bar{B}_1]$ , the total can be written

$$[\bar{B}] = [\bar{B}_0] + [\bar{B}_1] \quad (D.21)$$

Integrating  $\zeta d\zeta$ ,  $d\zeta$ , and  $\zeta^2 d\zeta$ , yields 0, 2, and 2/3, respectively, leading to the following element stiffness matrix equation

$$[k] = \int_{-1}^1 \int_{-1}^1 \left( 2[\bar{B}_0]^T [\bar{E}] [\bar{B}_0] + \frac{2}{3} [\bar{B}_1]^T [\bar{E}] [\bar{B}_1] \right) J d\xi d\eta \quad (D.22)$$

where, for the quasi-isotropic composite panel studied in this thesis,  $[\bar{E}]$  is symmetric with respect to  $\zeta = 0$ .

Having derived the element stiffness matrix  $[\bar{k}]$ , each one is then assembled into a structural stiffness matrix  $[\bar{K}]$ . This is the  $[\bar{K}]$  matrix used in Equation 2.28 for the development of the eigenvalue problem.

A consistent mass matrix  $[\bar{m}]$  is required for the NKTP 32 element. For the eight-noded element,  $[\bar{m}]$  is a 24 x 24 positive definite matrix. Each element mass matrix is assembled into the structural mass matrix  $[\bar{M}]$  in the same way that the element stiffness matrices are assembled into the structural mass matrix. The matrix  $[\bar{M}]$  is also used in Equation 2.28 to develop the eigenvalue problem.

This completes a summary of the formulation of a general shell element similar to the NKTP 32 element used by NISA. This summary follows from Cook [6], Zienkiewicz [50], and the NISA Manual [11].

## Appendix E: Preliminary NISA Study

A preliminary study was made of NISA solutions to a variety of closed-form vibration problems. The purpose was to establish the accuracy of NISA in solving relatively simple problems before using it to analyze the more difficult composite cylindrical panel studied in this thesis. The test cases were chosen to compare NISA accuracy with flat plates versus cylindrical shells, and with isotropic materials versus anisotropic, laminated composite materials.

Three documented cases were used: one was Monahan's analysis of a thin aluminum flat plate [24], one was Yen's analysis of a thin composite flat plate [49], and one was Soedel's analysis of a thin steel cylindrical shell [35]. The accuracy of three NISA shell elements was investigated. These elements included the 3D Thin Shell (Discrete Kirchhoff) Element, NKTP 40; the 3D General Shell Element, NKTP 20; and the 3D Laminated Composite General Shell Element, NKTP 32.

Monahan studied the natural frequencies and mode shapes of a fully clamped, 10 x 7-inch thin aluminum plate. He used a closed-form theoretical technique, developed a finite element solution, and performed holographic experimental analysis. His results are summarized in Table E.1. The predictions of three NISA models were compared with his

results. Each model had a 10 x 7 element mesh. The first model used four-noded NKTP 40 elements; the second used four-noded NKTP 20 elements; and the third used eight-noded NKTP 20 elements. These results are also presented in Table E.1.

Table E.1. Monahan's Aluminum Plate  
(Natural Frequencies in Hz)

Source	Mode				
	1	2	3	4	5
Monahan					
Theory	273	436	657	708	809
FEM	273	437	660	715	812
Experimental	238	400	601	656	750
NISA					
NKTP 40 (4 nodes)	273	437	661	712	815
NKTP 20 (4 nodes)	283	458	754	792	900
NKTP 20 (8 nodes)	275	444	666	731	845

The NKTP 40 element, based on Kirchoff's thin plate theory that ignores transverse shear effects, agreed with Monahan's theoretical and experimental results within 1% for each mode. The eight-noded NKTP 40 element, which includes transverse shear effects, agreed to within 0% for first mode to within 4% for fifth mode. The four-noded NKTP element did not agree as well, differing by as much as 15% for third mode.

Yen studied a fully-clamped, 12 x 12-inch, thin graphite/epoxy plate. He used a closed-form Galerkin technique, the NASTRAN finite element code, and an experimental method to obtain the results given in Table E.2. Eight-noded NKTP 32 elements were assembled in an 8 x 8 element mesh to model this composite plate. The NISA results are also in Table E.2.

Table E.2. Yen's Composite Plate  
(Natural Frequencies in Hz)

Source	Mode				
	1	2	3	4	5
Yen					
Theory	102	282	336	421	543
FEM	101	287	346	426	567
Experimental	89	270	325	415	560
NISA					
NKTP 32 (8 nodes)	103	299	354	434	664
		*185/237		**452/526/575	

NISA predicted more modes between 100 Hz-600 Hz than Yen reported. However, when like mode shapes were correlated between NISA and Yen's results, the frequency differences ranged from 1% to 6% for the first four modes and jumped to 22% for the fifth mode. The intermediate modes predicted by NISA are indicated in Table E.2 by single and double asterisks (\* and \*\*). No explanation is given for the

appearance of additional mode shapes in NISA; these mode shapes, though, were consistent with the expected behavior of a fully-clamped, quasi-isotropic plate.

Soedel presented a theoretical solution for the natural frequencies and mode shapes of a thin, isotropic cylinder. The NISA NKTP 40 element and the NKTP 20 element were used to solve this problem. These models consisted of 10 x 5 and 20 x 5 element meshes. The results are compared to Soedel's results in Table E.3.

Table E.3. Soedel's Steel Cylinder  
(Natural Frequencies in Hz)

Source	Mode				
	1	2	3	4	5
Soedel Theory	1343	1465	1726	1892	2493
NISA					
NKTP 40 (4 nodes)					
10 x 5 Mesh	1360	1489	1741	1946	2618
20 x 5 Mesh	1340	1454	1730	1874	2469
NKTP 20 (4 nodes)					
10 x 5 Mesh	1542	1857	1891	2870	2899
20 x 5 Mesh	1382	1534	1763	2045	2800
NKTP 20 (8 nodes)					
10 x 5 Mesh	1341	1469	1726	1923	2592

The results for the 10 x 5 mesh, NKTP 40 model agreed with Soedel to within 1%-5% for the five modes analyzed.

This improved to 0.2%-1% for the finer 20 x 5 mesh. The results for the 10 x 5 mesh, four-noded NKTP 20 model did not agree well, ranging from 10%-52% difference. Agreement improved markedly with the finer 20 x 5 mesh, resulting in agreement to within 2%-12% for the five modes. Finally, the 10 x 5 mesh, eight-noded NKTP 20 model gave excellent results, agreeing with Soedel to within 0%-4%.

These simple test cases provided a preliminary look at the relative merits of the thin shell versus general shell elements in analyzing thin, isotropic plates and shells, and at the reliability of the composite shell element for analyzing thin composite plates. The results for Monahan's isotropic plate indicated that an eight-noded NKTP 20 element was required to match the excellent results obtained with the four-noded NKTP 40 element. Thus, more degrees of freedom overcame the impact of introducing transverse shear effects with the general shell element.

The analysis of Yen's composite plate indicated that the NKTP 32 element was adequate for modeling a thin plate. Further study, however, should be done to determine why the NISA element predicted more modes in the 100 Hz-600 Hz range than reported by Yen.

The results for Soedel's cylinder are especially pertinent because they address the difference between using a thin shell element that neglects transverse shear effects

and using a general shell element that includes these effects. Clearly, the thin shell agreed well for both the 10 x 5 and 20 x 5 meshes, differing, at most, by 5%. The four-noded NKTP 20 element did not agree as well, differing with Soedel by 10%-52% for the 10 x 5 mesh and by 2%-12% for the 20 x 5 mesh. The eight-noded NKTP 20 model, however, had excellent agreement to within 0%-4% for a 10 x 5 mesh.

Two conclusions were drawn from this brief study. First, the eight-noded general shell element, NKTP 20, provided excellent results for thin isotropic plates and shells. It handled transverse shear effects very well. Second, the eight-noded composite general shell element, NKTP 32, provided excellent results for selected frequencies of a thin quasi-isotropic plate, but predicted more modes than were obtained by theory, by another FEM code, and by experiment. Thus, it would seem that differences in the NISA predictions obtained for the cylindrical composite panels studied in this thesis would be a function of the composite material, rather than of the curvature or thinness of the panels.

VITA

William P. Goodwin was born [REDACTED]

[REDACTED] Following his graduation from [REDACTED] he attended the United States Military Academy at West Point, New York. He received a Bachelor of Science degree from West Point in 1973 and was commissioned a second lieutenant in the US Army Corps of Engineers. In 1977 he completed the Army's Rotary Wing Aviator Course, and eventually transferred to the Army's newly established Aviation Branch in 1983. He attended the Army's Command and General Staff College in 1986-87. His duty assignments have included engineer and aviation platoon leader, aviation operations officer and company commander, battalion executive officer, and division-level staff officer. He entered the Air Force Institute of Technology in June 1987.

REPORT DOCUMENTATION PAGE

Form Approved  
OMB No. 0704-0188

1. REPORT SECURITY CLASSIFICATION <b>UNCLASSIFIED</b>		1b. RESTRICTIVE MARKINGS	
2a. SECURITY CLASSIFICATION AUTHORITY		3. DISTRIBUTION / AVAILABILITY OF REPORT Approved for public release; distribution unlimited	
2b. DECLASSIFICATION / DOWNGRADING SCHEDULE			
4. PERFORMING ORGANIZATION REPORT NUMBER(S) AFIT/GAE/AA/88D-18		5. MONITORING ORGANIZATION REPORT NUMBER(S)	
6a. NAME OF PERFORMING ORGANIZATION School of Engineering	6b. OFFICE SYMBOL (if applicable) AFIT/ENY	7a. NAME OF MONITORING ORGANIZATION	
6c. ADDRESS (City, State, and ZIP Code) Air Force Institute of Technology (AU), Wright-Patterson AFB, Ohio 45433-6583		7b. ADDRESS (City, State, and ZIP Code)	
8a. NAME OF FUNDING / SPONSORING ORGANIZATION	8b. OFFICE SYMBOL (if applicable)	9. PROCUREMENT INSTRUMENT IDENTIFICATION NUMBER	
8c. ADDRESS (City, State, and ZIP Code)		10. SOURCE OF FUNDING NUMBERS	
		PROGRAM ELEMENT NO.	PROJECT NO.
		TASK NO.	WORK UNIT ACCESSION NO.
11. TITLE (Include Security Classification) EFFECTS OF BATTLE DAMAGE REPAIR ON THE NATURAL FREQUENCIES AND MODE SHAPES OF CURVED RECTANGULAR COMPOSITE PANELS			
PERSONAL AUTHOR(S) William P. Goodwin, B.S., Major, U.S. Army			
13a. TYPE OF REPORT MS Thesis	13b. TIME COVERED FROM _____ TO _____	14. DATE OF REPORT (Year, Month, Day) 1988 December	15. PAGE COUNT 201
16. SUPPLEMENTARY NOTATION			
17. COSATI CODES		18. SUBJECT TERMS (Continue on reverse if necessary and identify by block number)	
FIELD	GROUP	SUB-GROUP	
11	04	Composites, Vibrations, Holography, NISA, Finite Elements,	
20	11	Natural Frequencies, Mode Shapes, Aircraft Battle Damage Repair. JES	
19. ABSTRACT (Continue on reverse if necessary and identify by block number)			
Thesis Advisor: Howard D. Gans, PhD Assistant Professor of Aerospace Engineering Department of Aeronautics and Astronautics			
20. DISTRIBUTION / AVAILABILITY OF ABSTRACT <input checked="" type="checkbox"/> UNCLASSIFIED/UNLIMITED <input type="checkbox"/> SAME AS RPT. <input type="checkbox"/> DTIC USERS		21. ABSTRACT SECURITY CLASSIFICATION <b>UNCLASSIFIED</b>	
22a. NAME OF RESPONSIBLE INDIVIDUAL Howard D. Gans, PhD	22b. TELEPHONE (Include Area Code) (513) 255-3069	22c. OFFICE SYMBOL AFIT/ENY	

*SDP reviewed  
12 Jan 1989*

UNCLASSIFIED

Interferometric holography and a finite element computer code, NISA, were used to experimentally and numerically determine the effects of battle damage repairs on the free vibrational behavior of thin, cylindrical composite panels. The primary objective was to experimentally determine how mass and stiffness changes introduced by mechanically fastened aluminum patches altered the natural frequencies and mode shapes of the panels. The secondary objective was to investigate the accuracy of the PC version of NISA in predicting the free vibrational behavior of the same panels. *✓ l, with →*

The thin, graphite/epoxy panels had a quasi-isotropic lay-up, [0/-45/45/90]<sub>s</sub>, and a 12 inch height and 12 inch radius of curvature. Each fully-clamped panel had a 2 x 4 inch cutout oriented at either 0°, 90°, +45°, -45° with respect to the panel circumference. A thin, 3.5 x 5.5 inch aluminum patch was riveted to each panel to cover the cutout area.

In general, the patch increased the natural frequencies of the cutout panels, but did not consistently restore the frequencies of the original solid panel. The mode shapes were restored to those of the original solid panel, although at the higher modes they did not always appear in the original sequence. The influence of the patch on the mode shapes increased at the higher modes as panel behavior became increasingly localized.

NISA predictions for the natural frequencies were within 10% - 20% of the experimental results, except for the 90° repaired panel, where they were within 2% - 6%. The correct mode shapes were predicted; however, they frequently appeared in a different sequence than observed experimentally.

A parallel investigation showed that both the NISA thin shell and general shell elements gave excellent results for both an isotropic flat plate and cylinder. Accuracy decreased slightly when the composite general shell element was used for a thin composite plate. The least accuracy was observed when the composite general shell element was used for a composite cylindrical panel.

UNCLASSIFIED